

4-2016

Iron Complexes for Photocatalytic Hydrogen Generation

Carolyn L. Hartley
College of William and Mary

Follow this and additional works at: <https://scholarworks.wm.edu/honorsthesis>

 Part of the [Inorganic Chemistry Commons](#)

Recommended Citation

Hartley, Carolyn L., "Iron Complexes for Photocatalytic Hydrogen Generation" (2016). *Undergraduate Honors Theses*. Paper 909.

<https://scholarworks.wm.edu/honorsthesis/909>

This Honors Thesis is brought to you for free and open access by the Theses, Dissertations, & Master Projects at W&M ScholarWorks. It has been accepted for inclusion in Undergraduate Honors Theses by an authorized administrator of W&M ScholarWorks. For more information, please contact scholarworks@wm.edu.

Iron Complexes for Photocatalytic Hydrogen Generation

A thesis submitted in partial fulfillment of the requirement
for the degree of Bachelors of Science in Department of Chemistry from
The College of William and Mary

By

Carolyn L. Hartley

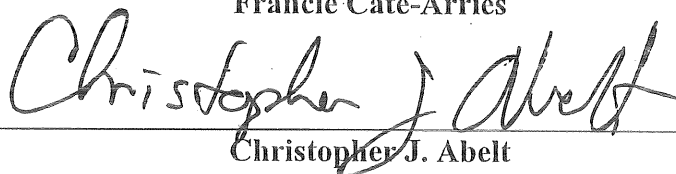
Accepted for Honors



William R. McNamara, Director



Francie Cate-Arries



Christopher J. Abelt



Kristin L. Wustholz

Williamsburg, VA
April 27, 2016

Table of Contents

Acknowledgments	4
List of Figures, Tables, Equations, and Schemes	5
List of Appendix Figures	9
Chapter 1: Introduction	11
The Global Energy Crisis	11
Solar Power and Artificial Photosynthesis	14
Developing Molecular Catalysts for Proton Reduction	17
Evaluating Proton Reduction Catalysts	19
References	22
Chapter 2: Electrocatalysis with Polypyridyl Complexes: Parent and Nitro	24
Introduction	24
Experimental	28
Results and Discussion	36
Conclusions	52
References	53
Appendix A	54
Chapter 3: Electrocatalysis with Sulfinato Complex	61
Introduction	61
Experimental	63
Results and Discussion	71
Conclusions	85
References	86

Appendix B	87
Chapter 4: Photochemical Systems for Hydrogen Generation	93
Introduction	93
Experimental	95
Results and Discussion	101
Conclusions	115
References	116
Appendix C	117

Acknowledgments

I would like to first thank Professor McNamara for serving as my research advisor for the past three years. My experiences in lab have been some of the most fulfilling, challenging, and definitive parts of my college experience, and I truly appreciate all of your patience and mentorship. I would not be the researcher I am today without your guidance. I also want to recognize the entire McNamara lab for its support and camaraderie, with a huge thank you to Ryan DiRisio and Megan Screen for their contributions to this project. Their collaboration and company made the late nights and early mornings involved in this project all the better.

I would also like to thank Professors Cate-Arries, Abelt, and Wustholz for serving on my honors thesis committee. Each of their classes have deepened my intellectual curiosity and helped me to envision meaningful ways to combine my interests in chemistry and Hispanic studies. Professor Cate-Arries has helped me to grow as a student at W&M and abroad, and has been instrumental to my interdisciplinary approach to scholarship. I am grateful to Professor Abelt for all of the knowledge imparted to me in two semesters of organic chemistry. Lastly, a special note of appreciation is due to Professor Wustholz for her guidance both in and out of the classroom. Professor Wustholz's instruction through two semesters of physical chemistry as well as conversations with her in office hours have provided me with invaluable support and inspiration in my development as a scientist.

Finally, I owe a great deal to my parents, my campus minister Max Blalock, and my friends for all of the support during the course of my research and throughout my time at William and Mary. Their love and support were the catalysts behind my work in the lab.

List of Figures, Tables, Equations, and Schemes

Figures

Figure 1.1: Projected global energy consumption	12
Figure 1.2: Primary energy sources for U.S.	13
Figure 1.3: Schematic of photosynthesis	16
Figure 1.4: [NiFe]-hydrogenase active site	17
Figure 1.5: [FeFe]-hydrogenase active site	17
Figure 1.6: [Fe]-hydrogenase active site	18
Figure 1.7: Structural mimic of [NiFe]-hydrogenase	19
Figure 1.8: Functional mimic of [NiFe]-hydrogenase	19
Figure 1.9: Example cyclic voltammogram	20
Figure 1.10: Photochemical system for artificial photosynthesis	21
Figure 2.1: Fe porphyrin complex	24
Figure 2.2: [Fe]-hydrogenase active site mimic	24
Figure 2.3: Fe carbonyl cluster catalyst	25
Figure 2.4: Complexes 2 and 4	26
Figure 2.5: ORTEP diagram of 4	36
Figure 2.6: CVs of 4 at varying scan rates	39
Figure 2.7: Comparison of redox couples of 2 and 4	40
Figure 2.8: Proton concentration study with 4 at 200 mV/s	41
Figure 2.9: Catalyst concentration study with 4 at 200 mV/s	42
Figure 2.10: Determination of i_c/i_p	43
Figure 2.11: Scan rate dependence study with 4	44

Figure 2.12: Proton concentration study with 4 at 10 V/s	45
Figure 2.13: Determination of overpotential	47
Figure 2.14: Comparison CVs of 2 and 4 with 8.8 mM TFA	48
Figure 2.15: Proposed mechanism of 4	49
Figure 2.16: CPC study with 4	50
Figure 2.17: CV of 4 upon additions of water	51
Figure 3.1: S-oxygenation of cysteine by CDO	61
Figure 3.2: Complexes 2 , 4 , and 6	62
Figure 3.3: ORTEP diagram of 6	71
Figure 3.4: Proton concentration study with 6 at 200 mV/s	75
Figure 3.5: Catalyst concentration study with 6 at 200 mV/s	76
Figure 3.6: Scan rate dependence study with 6	77
Figure 3.7: Proton concentration study with 6 at 10 V/s	77
Figure 3.8: Comparison CVs of 2 and 6 with 8.8 mM TFA	79
Figure 3.9: Proposed mechanism of 6	80
Figure 3.10: CPC study with 6	82
Figure 3.11: UV-Vis spectrum of 6 before and after addition of 11 mM TFA	83
Figure 3.12: CV of 6 upon addition of water	84
Figure 4.1: Three component system for H ₂ generation	94
Figure 4.2: GC calibration curve	97
Figure 4.3: Commonly used chromophores	101
Figure 4.4: Chromophore reduction potentials	102
Figure 4.5: TON vs. [2]	104

Figure 4.6: TON vs. [Fl] with 2	105
Figure 4.7: TON vs. pH with 2	106
Figure 4.8: Hydrogen evolution with 2 over 24 hours	107
Figure 4.9: Comparison of H ₂ generation by 2 , 4 , and 6	108
Figure 4.10: Hydrogen evolution using local pond water	109
Figure 4.11: Quenching pathway mechanisms	110
Figure 4.12: Fl quenching with TEA	111
Figure 4.13: Fl quenching with 2	111
Figure 4.14: Fl quenching with 4	112
Figure 4.15: Fl quenching with 6	112

Tables

Table 2.1: Bond lengths and angles for 4	37
Table 2.2: Selected X-ray data for 4	38
Table 3.1: Bond lengths and angles for 6	72
Table 3.2: Selected X-ray data for 6	73
Table 4.1: Catalyst concentration optimization with 2	103
Table 4.2: Fl concentration optimization with 2	104
Table 4.3: Quenching rates of 2 , 4 , and 6	113

Equations

Equation 1.1: Water oxidation	16
Equation 1.2: Proton reduction	16
Equation 2.1: Calculation of i_c/i_p	43

Equation 2.2: Correction for solvent dilution	45
Equation 2.3: Calculation of k_{obs}	45
Equation 2.4: Calculation of overpotential	47
Equation 4.1: Calculation of power	100
Equation 4.2: Calculation of average rate of hydrogen production	100
Equation 4.3: Calculation of photon flux	100
Equation 4.4: Calculation of quantum yield	100
 <i>Schemes</i>	
Scheme 2.1: Synthesis of 1	29
Scheme 2.2: Synthesis of 2	30
Scheme 2.3: Synthesis of 3	31
Scheme 2.4: Synthesis of 4	32
Scheme 3.1: Synthesis of 6	66

List of Appendix Figures

<i>Appendix A</i>	54
Figure A1: ^1H NMR Spectrum of 1	54
Figure A2: ^1H NMR Spectrum of 3	54
Figure A3: ^{13}C NMR of 3	55
Figure A4: High-Resolution Mass Spectrum of 4	55
Figure A5: Mössbauer Spectra of 2	56
Figure A6: Control CVs of 8.8 mM TFA with and without 4	57
Figure A7: CVs of 4 and ferrocene at varying proton concentrations	58
Figure A8: CVs of 4 with additions of tosic acid	58
Figure A9: GC calibration curve	59
Calculation of Faradaic yield	59
Determination of $[\text{H}^+]$ and [catalyst] dependence	60
 <i>Appendix B</i>	 87
Figure B1: ^1H NMR of 5	87
Figure B2: High Resolution Mass Spectrum of 5	88
Figure B3: High Resolution Mass Spectrum of 6	88
Figure B4: Control CVs of 22 mM TFA with and without 6	89
Figure B5: CVs of 6 and ferrocene at varying proton concentrations	89
Figure B6: CVs of 6 with additions of tosic acid	90
Figure B7: Dip Test Study	90
Figure B8: FeCl_3 Control Study	91
Figure B9: CVs of 6 before and after addition of H_2O	91

Calculation of k_{obs}	92
<i>Appendix C</i>	117
Table C1: Comparison of chromophore and sacrificial donors	117
Figure C1: TON vs. [Fl] with 4	117
Figure C2: TON vs. [4]	118
Figure C3: TON vs. pH with 4	118
Figure C4: TON vs. [Fl] with 6	119
Figure C5: TON vs. [6]	120
Figure C6: TON vs. pH with 6	120
Calculation of quantum yield	121

Chapter 1. Introduction

The Global Energy Crisis

Over the past century, dramatic increases in the size of the global population have led to a sharp growth in worldwide energy demands.¹ Additionally, the continued growth of less developed nations including India, China, and several South American countries have led to especially increased strains on energy.¹ In general, less developed nations are considered to be those countries that are not members of the Organization for Economic Cooperation and Development (OECD), an international organization that promotes economic growth and trade.¹ Owing to the dense populations and rapidly growing economies of non-OECD nations across the globe, the amount of energy used in these developing countries is expected to grow by approximately 2% per year.¹ This steady increase would escalate their demand of total worldwide energy usage from 54% in 2010 to 65% by 2040.¹ The significance of this vast growth in energy demands by developing countries must be considered seriously, as growth of non-developed nations causes greater strain to worldwide energy intake than the growth of OECD nations such as the United States (Figure 1.1).¹ The difference in strain posed by the growth of non-OECD nations versus that posed by OECD nations may be attributed to the already established technologies and relatively stable means of distributing and using energy in already developed countries, compared to nations that must undergo major renovations and advancement to fully power themselves.¹ Considering the energetic overhaul that non-OECD countries need in order to advance, the development of such nations may be viewed as the driving force behind increased global energy intake.¹

As the number of people on earth continues to increase alongside continued growth of less developed nations, overall global energy demands are projected to grow by approximately 2.3% per year, from 13.5 TW in 2001 to 40.8 TW in 2050.² These striking energy demands have

prompted a review of the primary sources of energy used across the globe, and of how to meet the higher energy needs effectively.

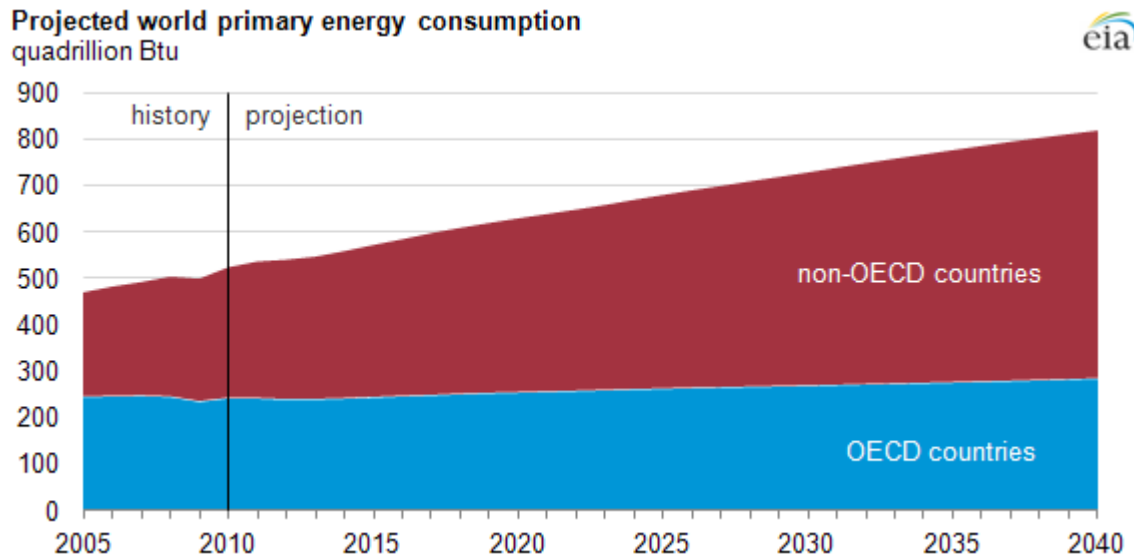


Figure 1.1. Projected global energy consumption comparing strains posed by growth of OCED vs. non-OECD nations.¹

The projections for increased strains on energy over the coming decades are particularly concerning considering the world’s primary sources of energy. Fossil fuels such as coal and natural gas have dominated the global energy supply since the industrial revolution, and continue to provide over 80% of the worldwide energy supply today.³ The United States echoes these trends, with the great majority of its energy still supplied from petroleum , natural gas, and coal (Figure 1.2).⁴ While fossil fuels are a major source of energy due to their high energy density and established use in modern society, their continued dominance is not sustainable.^{1,3} Based on energy consumption data from 1998, the global supplies of extractable oil may last another 50-150 years.¹ Similarly, there are approximately 200-600 years of gas left in global reserves, and 1000-2000 years of available coal remaining.¹ While this data suggests that there are sufficient fossil fuel reserves remaining to power the planet for several centuries, these are likely

overestimates as the projections assume a global energy consumption rate of between 25 and 30 TW.¹ As consumption rates grow and exceed this limit, the remaining fossil fuels available will dwindle in a shorter time span.

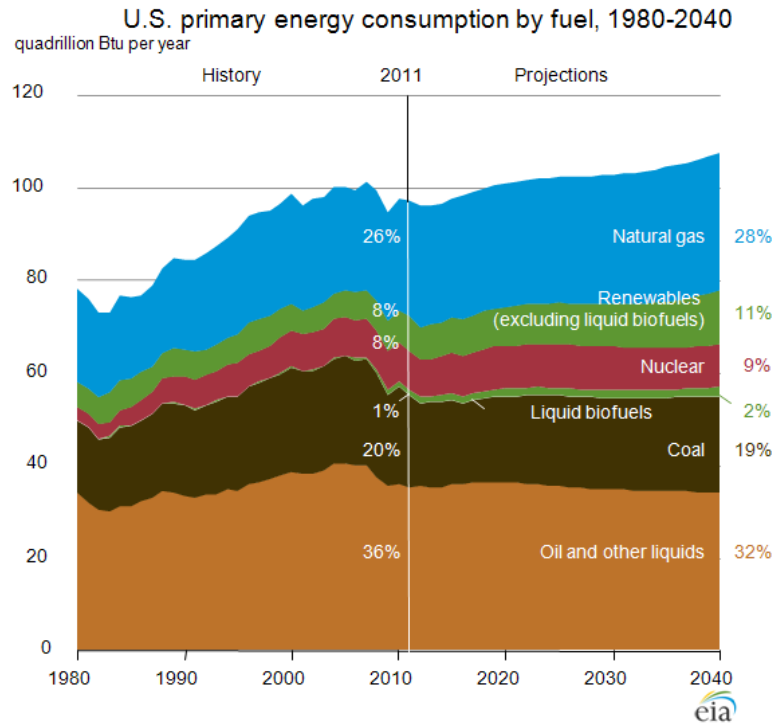


Figure 1.2. Primary energy sources for the United States from 1980 with projections until 2040.⁴

In addition to the fact that they are exhaustible, maintaining fossil fuels as the primary source of energy presents a host of problems. Primarily, the combustion of fossil fuels emits pollutants such as sulfur oxides and volatile organic compounds that are harmful to human health. Additionally, the emission of greenhouse gases such as carbon dioxide and nitrous oxides contribute to climate change.⁴ For example, increases in the concentration of greenhouse gases in the atmosphere and depletion of the ozone layer have led to increased average global

temperatures and various other harmful impacts to the environment including rising sea-levels, melting of the polar ice caps, and increased frequency of extreme weather.⁴

As fossil fuel reserves decline, it will increasingly require the use of fracking and other invasive methods to harvest these fuels. It is becoming less sustainable to continue to rely on fossil fuels, and cost of collection of these resources will soon become unjustifiable.³ It is abundantly clear that the supply of secure, clean and sustainable energy is one of the greatest challenges facing humanity today.² It is therefore necessary to develop clean, cost-effective and efficient methods of powering the planet.

Solar Power and Artificial Photosynthesis

In order to increase the global energy supply without continuing to harm the environment, it will be necessary to rely on renewable energy. There are numerous forms of alternative energy resources, and among the most established include wind, geothermal, nuclear and solar power. Each option is characterized by distinct advantages and disadvantages and some are better suited for certain environments than others. For example, wind turbines are excellent sources of harnessing energy; however their practicality is limited to locations that experience strong, sustained winds for much of the year. Geothermal energy sources are similarly limited in feasibility on a global scale. Nuclear power plants present another option, but are a less attractive alternative as they necessitate a timeline of 35 years to generate sufficient energy to offset fossil fuel dependence.¹ Of the options presented, solar energy is by far the most universally available and energetically viable.^{2,3} In addition to the solar resource being essentially limitless, the sun irradiates sufficient harvestable energy to the earth's surface to meet global energy demands for an entire year in fewer than 90 minutes.^{2,3}

The abundance of potential energy provided by the sun has prompted the scientific community to develop methods of harnessing this power. One of the most common technologies for harnessing solar energy includes dye-sensitized solar cells. This form of solar cell operates by converting absorbed photon energy directly into usable electricity through electron transfer and capture processes. Although these devices have developed substantially in recent decades, their competitiveness is limited. Current solar cells directly convert solar energy into electricity that must be immediately used or is dissipated over time. Similarly, the devices cannot function as sources of power for businesses or homes at night or during periods of especially low irradiance.² These limitations underscore the importance of developing technologies that can not only capture and convert photon energy, but also allow for energy storage in the form of a solar fuel.

One of the most promising methods of solving the problem of efficient energy capture and storage is by mimicking plants in nature. Plants have evolved over time to harness solar energy to convert carbon dioxide into chemical fuel via photosynthesis. In photosynthesis, there are two related photosystems: photosystem I (PSI) and photosystem II (PSII). Upon irradiation, PSI triggers an electron transfer process to reduce the enzyme cofactor NADP^+ to NADPH via the hydrogenase enzyme, oxidizing PSI.⁵ PSI is then regenerated from electrons supplied by the complementary PSII that mediates oxidation of water to oxygen upon excitation with light energy (Figure 1.3).⁵

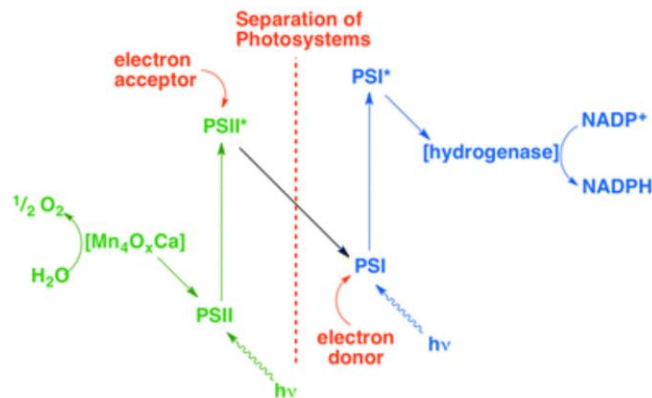
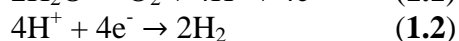


Figure 1.3. Schematic of photosynthesis, simplified and separated into PSI and PSII.⁵

It is possible to mimic the redox reactions of photosynthesis to develop commercially viable fuels by catalytic water splitting, a process termed artificial photosynthesis (AP).^{2,5} AP is one of the most promising and cost-effective means of generating fuel, and is carried out in two redox half reactions that oxidize water to oxygen and reduce protons to hydrogen (Equations 1.1 and 1.2):⁵



Over the past decade, much progress has been made in developing catalysts for water oxidation and proton reduction. The oxidation of water to O₂ has proven to be significantly more challenging than proton reduction because it requires a substantial four electrons whereas proton reduction is a two electron process.

While the two half reactions would ultimately recombine in a fuel cell device, it is advantageous to study each process separately in order to achieve optimal activity. Systems for proton reduction are of high interest because hydrogen is considered an important alternative source of energy. Hydrogen, with its high combustion energy, low density, and environmentally-benign combustion products, is a convenient fuel that may be stored or combined with oxygen in

a fuel cell to generate electricity.^{5, 6} In order to develop devices for hydrogen evolution, it is necessary to develop catalysts that readily reduce protons. A unique set of enzymes found in nature known as hydrogenase enzymes have provided inspiration for the design of such catalysts.

Developing Molecular Catalysts for Proton Reduction

Much like with the development of AP, the scientific community has drawn inspiration for designing proton reduction catalysts from nature. Hydrogenase enzymes occur in a variety of

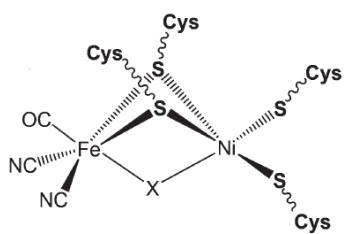


Figure 1.4. [NiFe]-hydrogenase active site.⁷

plants and bacteria and catalyze the formation or oxidation of H₂. There are three types of hydrogenases, each named according to the metals of their active sites: [NiFe]-hydrogenase, [FeFe]-

hydrogenase, and [Fe]-hydrogenase. In addition to the difference in metal centers composing the active sites of each of the enzymes, the surrounding proteins and ligands greatly affect the role and activity.

The most abundant hydrogenase is the [NiFe]-hydrogenase, found in a number of archaea and cyanobacteria.⁷ The active site consists of two subunits that together form an electron transfer pathway between the surrounding proteins and the Ni and Fe centers (Figure 1.4).⁸ The [FeFe]-

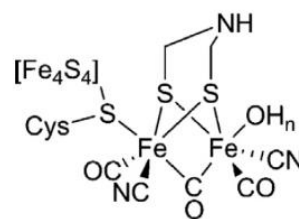


Figure 1.5. [FeFe]-hydrogenase active site.¹⁰

hydrogenase, by comparison, is composed of two iron centers that share a cysteine ligand with a Fe-S cluster (Figure 1.5).^{9,10} The Fe-S clusters allow for electron transport across the active site and are characteristic of the [FeFe]-hydrogenase active site.⁸ Additionally, the coordinated OH⁻ ion is thought to play an important protective role in the enzyme's oxidation state.⁸ The third hydrogenase is the mononuclear [Fe]-

hydrogenase, which occurs only in the hydrogenotrophic methanogenic archaea. It is called hydrogen-forming methylene-tetrahydromethanopterin H₄MPT dehydrogenase (Hmd) as it catalyzes the dehydrogenation of methylene-H₄MPT.⁷ The active site is composed of a single Fe center bonded to CO, H₂O and S ligands (Figure 1.6).^{7, 10}

While hydrogenase enzymes are highly active for hydrogen generation, their large size and low activity outside of the natural protein environments limit their use in systems for AP. To circumvent these limitations, it is possible to develop complexes that mimic the hydrogenase active sites to mimic the function of these enzymes for use in solar energy devices to produce H₂ fuel. One of the most structurally-accurate hydrogenase active site mimics was reported in 2005 by Tatsumi and coworkers.^{11, 12} The complex was a

dithiolate-bridged Ni-Fe complex with the Ni center bonded in an S₄³⁻ environment and CO and CN ligands bonded to the iron center (Figure 1.7).^{11, 12}

While this structural derivative was a major step towards developing active site mimics, the complex was not found to be catalytically active for proton reduction.^{11, 12}

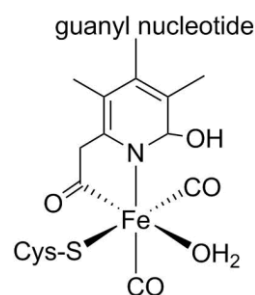


Figure 1.6. [Fe]-hydrogenase active site.

Another approach in designing hydrogenase active site mimics has been to replace one or more metals in the active site with noble metals such as Pt, Rh, or Ru. The replacement of one of the metal centers with electron rich noble metals such as Ru is favorable because they can easily bind to hydride ligands and release them as hydrogen radicals that may then bind and form H₂.¹² Additionally, Ru complexes were previously known to catalytically activate hydrogen, and were thus of interest for incorporation into hydrogenase mimics.¹² Oudart *et al.* reported a Ni-Ru complex in 2006, for example, that was the first reported functional [NiFe]-hydrogenase active

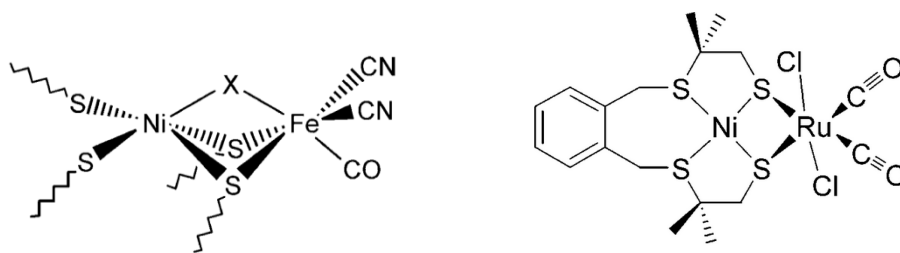


Figure 1.7. (left) Structural model for [NiFe]-hydrogenase active site reported by Tatsumi and coworkers where X is an oxygenated ligand removed upon reduction of the complex.¹¹
Figure 1.8. (right) First functional [NiFe]-hydrogenase mimic for proton reduction with Ni-Ru bimetallic center reported by Oudart *et al.*¹²

site mimic for proton reduction (Figure 1.8).¹² Although the development of catalysts that mimic the active site of hydrogenase enzymes and are active for proton reduction is important, complexes composed of rare and expensive noble metals are ultimately unrealistic for larger-scale use. For potential widespread applications, catalysts must be made from inexpensive, earth abundant metals such as nickel, cobalt and iron.⁶

Evaluating Proton Reduction Catalysts

Electrochemistry

A commonly employed experimental method of assessing the activity and efficiency of catalysts for proton reduction is cyclic voltammetry (CV). This technique may help elucidate catalytic mechanism and shows the electrochemical response of a catalyst upon addition of a proton source such as a weak acid, indicating whether the catalyst is capable of proton reduction, by the appearance of an irreversible catalytic wave. For example, Figure 1.9 illustrates that upon increasing additions of a proton source there is an observable catalytic response at approximately -1.05 V vs. saturated calomel reference electrode (SCE).^{13, 14}

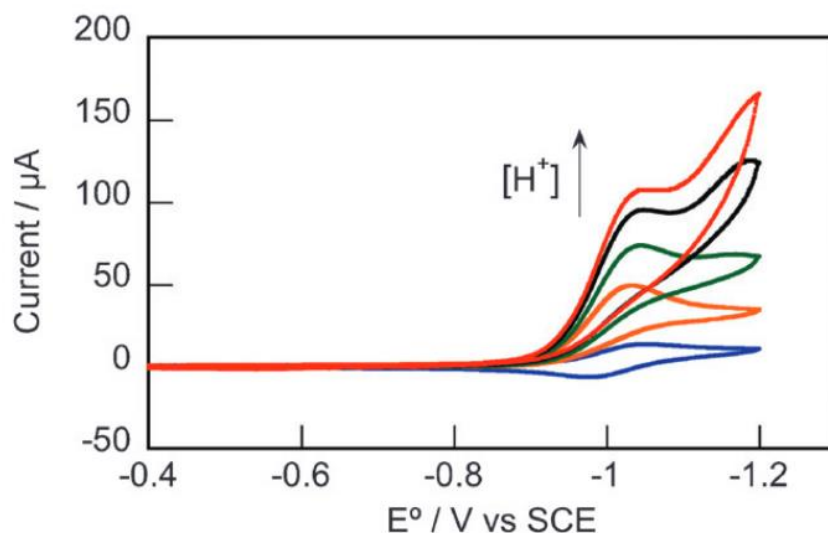


Figure 1.9. Example CV showing the formation of an irreversible catalytic wave upon addition of acid, corresponding to the reduction of protons.¹⁴

In addition to revealing activity of a catalyst for proton reduction, cyclic voltammetry allows for determination of the overpotential, a term that relates to the activation energy of catalysis.¹³ A greater overpotential indicates that a significant potential must be applied to the system (in addition to the thermodynamic requirement for proton reduction) to achieve catalysis.¹³ Ideally, a system for proton reduction will consist of a non-noble metal catalyst that operates with high activity and a low overpotential. A variety of electrocatalysts composed of earth-abundant transition metals such as Ni, Co, and Fe have been reported in recent years; however, their application is limited to use in organic solvents.¹⁵ Because systems for AP must ultimately operate in water, it is necessary to develop catalysts that can reduce protons in purely aqueous solution. Nevertheless, there have been very few examples of active catalysts composed of non-noble transition metals such as Fe that operate in aqueous media.¹⁵

Photochemistry

The development of active catalysts characterized by CV is of great interest for incorporation into photocatalytic systems. As a device for AP would ideally rely on solar energy as the driving force, it is necessary to probe the ability of active electrocatalysts to perform redox reactions triggered by photochemical processes.⁵

A theoretical device for photocatalytic proton reduction includes a chromophore and catalyst covalently attached to a semiconductor, such as TiO₂ (Figure 1.10). In practice, light first strikes the chromophore, exciting an electron from the chromophore into the conduction band of the semiconductor. The electron is then transferred to a molecular catalyst that reduces protons in solution to H₂.⁵

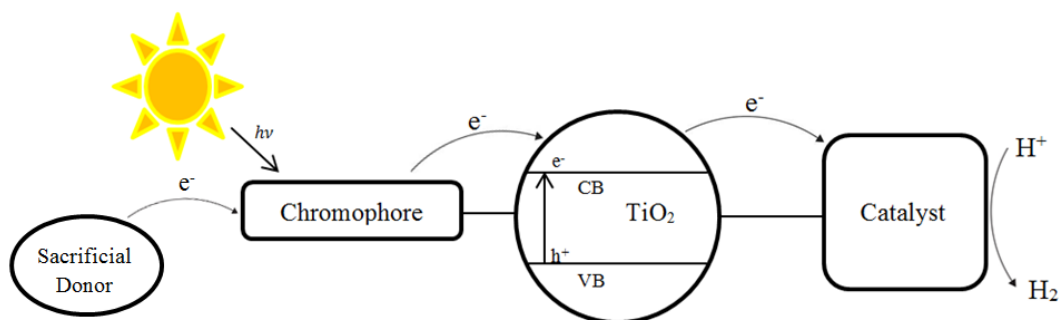


Figure 1.10. Photochemical system for artificial photosynthesis

In order to effectively carry out this process, catalysts that actively reduce protons from water must be discovered. An ideal photocatalyst will operate with high activity and efficiency in water, and will be long-lived and stable upon irradiation. The discovery of such catalysts is crucial to the advancement of devices for AP and hydrogen evolution.

References

- 1) (a) U.S. Energy Information Administration - EIA - Independent Statistics and Analysis. Retrieved March 09, 2016, from <http://www.eia.gov/> (b) U.S. Energy Information Administration - EIA - Independent Statistics and Analysis. Retrieved March 09, 2016, from <https://www.eia.gov/todayinenergy/detail.cfm?id=14011> (c) OECD.org. (n.d.). Retrieved April 09, 2016, from <http://www.oecd.org/>
- 2) (a) Lewis, N.S.; Nocera, D.G. *Proc. Nat. Acad. Sci.* **2006**, *103*, 15729-15735. (b) Eisenberg, R. *Science* **2009**, *324*, 44.
- 3) Solar Energy Perspectives. 2011. International Energy Agency. http://www.iea.org/publications/freepublications/publication/Solar_Energy_Perspectives2011.pdf (accessed December 30, 2014).
- 4) (a) The Energy Information Administration's New Report, In Four Charts. (n.d.). Retrieved April 17, 2016, from <https://stateimpact.npr.org/pennsylvania/2012/12/05/the-energy-information-administrations-new-report-in-four-charts/> (b) An Assessment of Energy Technologies and Research Opportunities. *Quadrennial Technology Review*. US Department of Energy, 2015. <http://energy.gov/sites/prod/files/2015/09/f26/QTR2015-01-Challenges.pdf>
- 5) Eckenhoff, W.T.; Eisenberg, R. *Dalton Trans.* **2012**, *41*, 13004.
- 6) (a) Tran, P.D.; Artero, V.; Fontecave, M. *Energy Environ. Sci.* **2010**, *3*, 727-747. (b) Andreiadis, E.S.; Chavarot-Kerlidou, M.; Fontecave, M.; Artero, V. *Photochem. Photobio.* **2011**, *87*, 946-964. (c) Alstrum-Acevedo, J.H.; Brennaman, M.K.; Meyer, T.J. *Inorg. Chem.* **2005**, *44*, 6802-6827. (d) Stubbert, B.; Peters, J.C.; Gray, H.B. *J. Am. Chem. Soc.* **2011**, *133*, 9212.
- 7) (a) Weber, K.; Kramer, T.; Shafaat, H.S.; Weyhermuler, T.; Bill, E.; van Gestel, M.; Neese, F.; Lubitz, W. *J. Am. Chem. Soc.* **2012**, *134*, 20745-20755. (b) Manor, B. C.; Rauchfuss, T.B. *J. Am. Chem. Soc.* **2013**, *135*(32), 11895-11900. (c) McGlynn, S.E.; Mulder, D.W.; Shepard, E.M.; Broderick, J.B.; Peters, J.W. *Dalton Trans.* **2009**, *22*, 4274-4285.
- 8) (a) Simmons, T.R.; Berggren, G.; Bacchi, M.; Fontecave, M.; Artero, V. *Coord. Chem. Rev.* **2014**, *270*, 127-150. (b) Finkelmann, A.R.; Senn, H.M.; Reiher, M. *Chem. Sci.* **2014**, *5*, 4474-4482.
- 9) Ghosh, S.; Hogarth, G.; Hollingsworth, N.; Holt, K.B.; Kabir, S.E.; Sanchez, B.E. *Chem. Comm.* **2014**, *50*, 945.
- 10) (a) Stiebritz, M.T.; Reiher, M. *Inorg. Chem.* **2010**, *49*, 5818-5823. (b) Mulder, D.W.; Ratzloff, M.W.; Bruschi, M.; Greco, C.; Koonce, E.; Peters, J.W.; King, P.W. *J. Am. Chem. Soc.* **2014**, *136*, 15394-15402. (c) Dey, S.; Das, P.K.; Dey, A. *Coord. Chem. Rev.* **2013**, *257*, 42-63.
- 11) Li, Z.; Ohki, Y.; Tatsumi, K. *J. Am. Chem. Soc.* **2005**, *127*, 8950-8951.
- 12) Oudart, Y.; Artero, V.; Pécaut, J.; Fontecave, M. *Inorg. Chem.* **2006**, *45* (11), 4334-4336.
- 13) Fourmond, V.; Jacques, P.; Fontecave, M.; Artero, V. *Inorg. Chem.* **2010**, *49*, 10338-10347.

- 14) Bigi, J.P.; Hanna, T.E.; Harman, W.H.; Chang, A.; Chang, C.J. *Chem. Commun.* **2010**, 46, 958-960.
- 15) (a) Rose, M.J.; Gray, H.B.; Winkler, J.R. *J. Am. Chem. Soc.* **2012**, 134, 8310-8313. (b) Kaur-Ghumaan, S.; Schwartz, L.; Lomoth, R.; Stein, M.; Ott, S. *Angew. Chem. Int. Ed.* **2010**, 49, 8033-8036. (c) Connor, G.P.; Mayer, K.J.; Tribble, C.S.; McNamara, W.R. *Inorg. Chem.* **2014**, 53(11), 5408-5410.

Chapter 2. Electrocatalysis with Polypyridyl Complexes: Parent and Nitro

Introduction

In recent decades much progress has been made in discovering catalysts for electro- and photochemical proton reduction. While highly active proton reduction catalysts composed of noble metals such as Pt and Ru have been reported, their high cost limits usefulness on a large scale. The need for cost-effective alternatives to Pt has motivated the development of catalysts using earth-abundant transition metals such as Co, Ni, and Fe.¹⁻⁴

While there have been numerous examples of cobalt and nickel catalysts for proton reduction, there have been far fewer reports of catalysts composed of iron. The greater abundance of iron on earth, however, makes the discovery of active catalysts with iron centers more desirable for sustainable, low-cost alternatives.

Though less common, there have been several iron electrocatalysts reported in recent years, with one of the first examples of a homogeneous iron electrocatalyst capable of proton reduction reported by Savéant and coworkers.¹ Their iron porphyrin complex reduced protons at a moderately negative potential of -1.6 V vs. SCE with good activity ($i_c/i_p \sim 10$ in the presence of

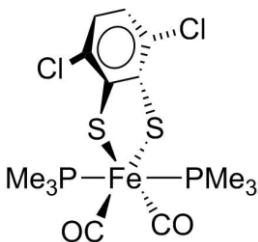


Figure 2.2. [Fe]-hydrogenase active site mimic reported by Kaur-Ghumaan et al.²

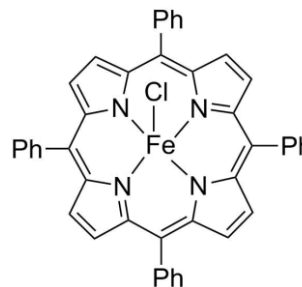


Figure 2.1. Fe Porphyrin complex reported by Saveánt and coworkers.¹

trifluoroacetic acid) (Figure 2.1).^{1,2} This study inspired further works, including that of Kaur-Ghumaan *et al.*, to develop complexes that successfully reduced protons to H₂ at less negative potentials. Kaur-Ghumaan *et al.* recently reported the first example of a mononuclear

iron complex that reduces protons at a more modest potential of -1.4 V vs. SCE and maintains the strong activity reported by Savéant (i_c/i_p also ~ 10) (Figure 2.2).^{2,3a} Similarly, Rose *et al.* reported several fluorinated diglyoxime-iron complexes that successfully reduced protons at an even lower potential of -0.8 V vs. SCE with an i_c/i_p of 8.²

In addition to the improvement in activity and efficiency, Berben and coworkers have made progress in developing iron catalysts that can reduce protons from purely aqueous media.^{3b}

The series of catalysts composed of iron carbonyl clusters reported by Berben in 2013 were among the first examples of iron catalysts that

function in aqueous solution, rather than organic or organic-water mixtures, and near neutral pH

(Figure 2.3).^{3b} This field has continued to flourish

with continued efforts towards developing

catalysts that operate at moderate overpotentials

with good activity. Although the examples discussed illustrate the progress made towards

developing cost-effective catalysts for proton reduction, the low activity of these systems

underscore the continued need to discover highly active and efficient iron catalysts.

Inspired by previously reported [Fe]-hydrogenase active site mimics, Connor *et al.* recently reported an iron polypyridyl catalyst (**2**) with a tetradentate monophenolate ligand that is active for electrocatalytic proton reduction (Figure 2.4, left).^{2,4,5} CV studies show that catalysis occurs at -1.57 V vs. Fc^+/Fc in CH_3CN with an overpotential of 800 mV and Faradic efficiencies of 98%. The complex is highly active with a turnover frequency (TOF) of 1000 s^{-1} and i_c/i_p reaching up to 7.8 in CH_3CN . Furthermore, catalytic activity is greatly enhanced in the presence of water showing TOF up to 3000 s^{-1} in 1:1 $CH_3CN:H_2O$ solutions. The complex is also stable

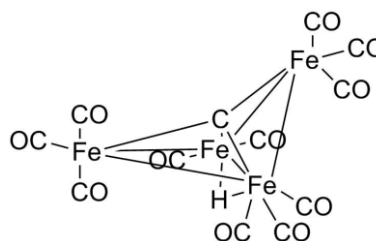


Figure 2.3. Fe catalyst proposed by Berben and coworkers.^{3b}

and active for hydrogen generation in aqueous buffer solutions of pH 3-5, illustrating its wide range of conditions at which it is capable of generating hydrogen. This catalyst is one of the most active iron electrocatalysts for proton reduction reported. However, though the catalyst is quite active, its moderately high overpotential limits its practicality for incorporation into systems for artificial photosynthesis (AP).

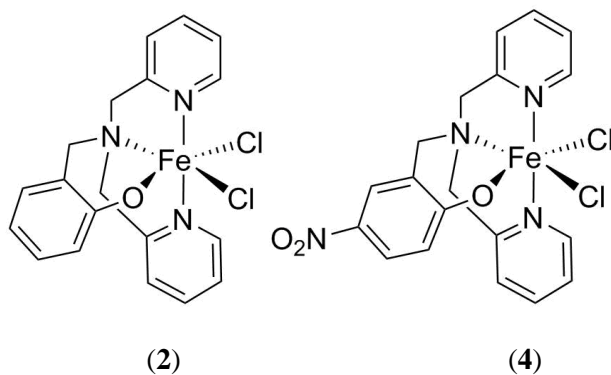


Figure 2.4. *Left:* Iron polypyridyl monophenolate complex (**2**) *Right:* Nitro-functionalized iron polypyridyl monophenolate complex (**4**).

A key benefit of developing molecular catalysts is their tunability via modification of the ligand, allowing control of electronic properties while maintaining key structural features. Due to the high overpotential of **2**, it was of interest to modify the complex to attain a lower overpotential while still maintaining catalytic activity. Many examples have been reported in the literature of cobalt glyoxime and nickel complexes whose electronic structure has been tuned to lower overpotential by ligand modification.^{6,7} Substitution of ligand functional groups with electron-withdrawing groups results in a more easily reduced complex, corresponding to a positive shift in reduction potential and subsequent lowering of overpotential.⁶ We reasoned that functionalizing the tetradentate monophenolate ligand with an electron-withdrawing NO₂ group would result in a complex that is easier to reduce and would therefore operate at a less cathodic potential.⁸

The work presented in this chapter reports the synthesis, characterization, and electrochemical analysis of a new iron catalyst (**4**) with a nitro-functionalized polypyridyl ligand (Figure 2.4, right). The complex was structurally characterized using NMR, MS, Mössbauer spectroscopy and X-ray diffractometry techniques. The catalytic activity of the complex was probed using cyclic voltammetry and controlled potential coulometry experiments. The effects of varying proton and catalyst concentrations were studied and a mechanism for catalysis is proposed. The motivation of this project is to develop an active analogue of the parent complex (**2**) that catalyzes proton reduction with greater efficiency at lower overpotential.

Experimental

Materials and methods

All synthesis experiments were performed using standard air-free Schlenk techniques under an Ar atmosphere, unless noted otherwise. 2-Hydroxy-5-nitrobenzaldehyde was purchased from Alfa Aesar and tetra-n-butylammoniumhexafluorophosphate (98%) was purchased from Acros Organics. All other chemicals used were purchased from Fischer Scientific without further purification before unless otherwise indicated.

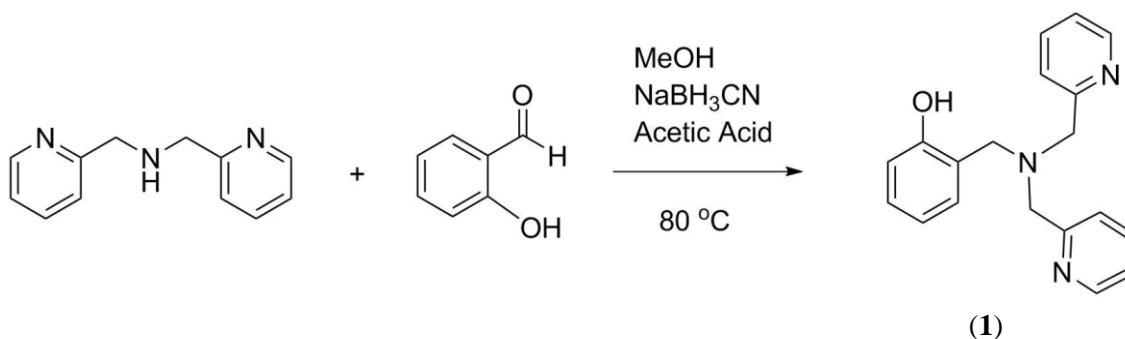
Instrumentation

^1H and ^{13}C spectra were recorded on an Agilent 400MR DD2 spectrometer operating in the pulse Fourier transform mode and chemical shifts are referenced to residual solvent. Elemental analysis was performed by the CENTC Elemental Analysis Facility at the University of Rochester. Mass spectrometry was carried out using positive electrospray ionization on a Bruker 12 Tesla APEX-Qe FTICR-MS with an Apollo II ion source. Mössbauer spectroscopy was performed at Carnegie Mellon University.

X-Ray Diffractometry

Single crystals were mounted on glass fibers and data for **2** and **4** were collected with graphite-monochromated Cu K α radiation ($\lambda = 1.54187$ nm) on a Bruker-AXS three-circle diffractometer using a SMART Apex II CCD detector. Crystal structures were solved via direct methods and refined using SIR2014 and SHELXL-2014/7.

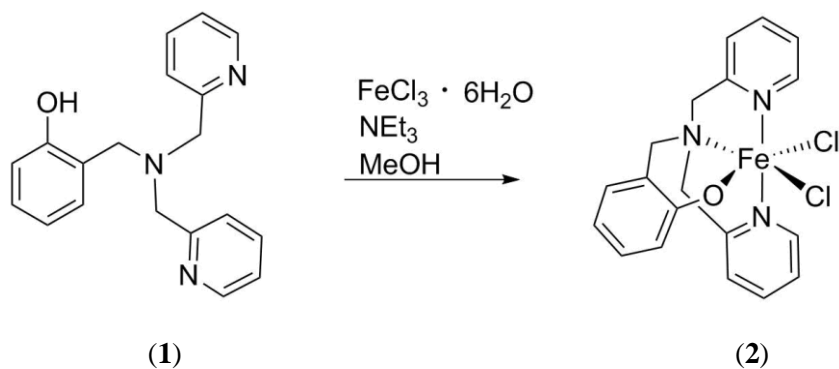
Syntheses



Scheme 2.1. Synthesis of **1**.

N-(2-hydroxybenzyl)-N,N-bis(2-pyridylmethyl)amine (L₁, **1)**

The ligand (**1**) was synthesized using a modified literature procedure (Scheme 2.1).⁹ Bis(pyridin-2-ylmethyl)amine (10 mmol) in 10 mL of MeOH was added to a degassed solution of salicylaldehyde (10 mmol) in 50 mL of MeOH under Ar. Three drops of glacial acetic acid were added to the solution, followed by dropwise addition of sodium cyanoborohydride (5 mmol) in 5 mL of MeOH, all under an Ar atmosphere. The resulting clear, yellow solution was refluxed for 1 hour and then stirred at room temperature overnight. 1 M HCl was added to the resulting solution until it reached pH 4 and changed from yellow to amber in color. The solution was evaporated to near dryness and dissolved in 25 mL of saturated Na₂CO₃ solution. This solution was then extracted with chloroform (3 x 75 mL). The organic layer was dried with Na₂SO₄ and filtered through celite. The liquid was evaporated to dryness to yield an amber oil. **1** was purified through a silica gel column run sequentially in 99:1, then 19:1, then 9:1 DCM:MeOH. The purified **1** was collected at a yield of 59% (1.80 g, 5.88 mmol) as an amber oil. ¹H NMR (CDCl₃): δ 8.49 (d, 2H), 7.57 (t, 2H), 7.29 (d, 2H), 7.10 (m, 3H), 7.00 (d, 1H), 6.84 (d, 1H), 6.70 (t, 1H), 3.81 (s, 4H), 3.73 (s, 2H) (see Appendix A).

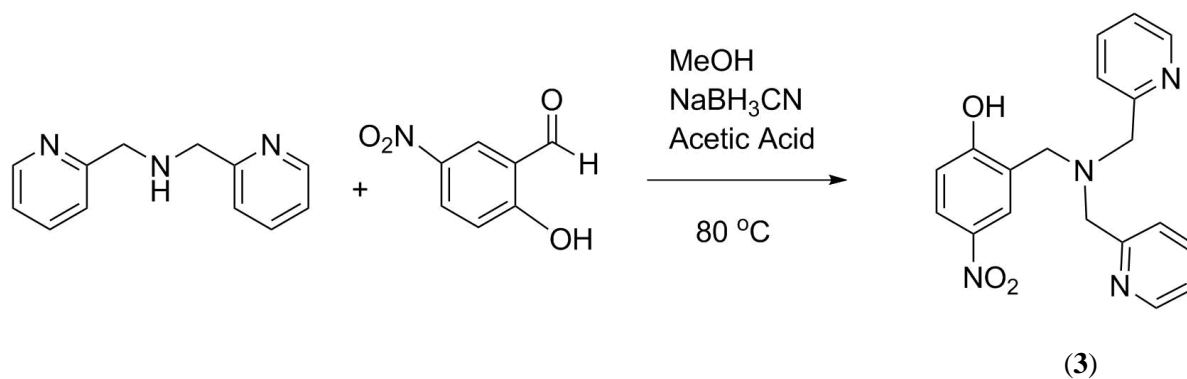


Scheme 2.2. Synthesis of **2**.

FeNNNO Complex ([FeCl₂(L₁)], **2**)

The FeNNNO complex (**2**) was synthesized using a modified literature procedure (Scheme 2.2).⁹

The ligand **1** (1.798 g, 5.88 mmol) and triethylamine (0.475 g, 4.7 mmol) were dissolved in 10 mL of MeOH and degassed under Ar. FeCl₃·6H₂O (1.271 g, 4.7 mmol) was also dissolved in 10 mL of MeOH and degassed. The solutions were combined under Ar to yield a dark solution with a visible dark blue precipitate. The reaction was stirred at room temperature for 1 hour and then filtered. The solid was washed with cold MeOH (3 x 10 mL). A dark solid of **2** was collected with 74% yield (1.502 g, 3.48 mmol). The product was crystallized by slow diffusion of hexanes into a concentrated solution of **2** in dichloromethane to yield blue feather crystals that were collected via filtration. Anal. Calcd. for **2** monohydrate FeC₁₉H₁₈N₃Cl₂·H₂O: C, 50.8; H, 4.49; N, 9.36%. Found: C, 50.66; H, 4.18; N, 9.13%.

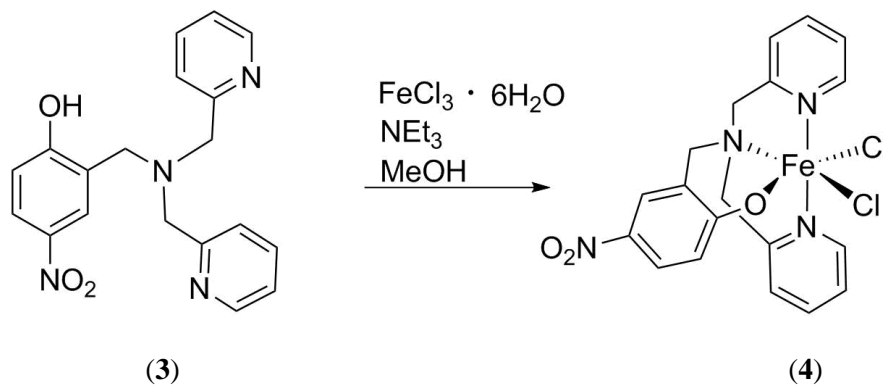


Scheme 2.3. Scheme for synthesis of **3**.

2-((bis(pyridin-2-ylmethyl)amino)methyl)-4-nitrophenol (**L₂**, **3**)

This procedure was modified from a literature method (Scheme 2.3).¹⁰ 2-hydroxy-5-nitrobenzaldehyde (3 mmol) was dissolved in 50 mL of MeOH and degassed under Ar. A degassed solution of bis(pyridin-2-ylmethyl)amine (3 mmol) in 5 mL of methanol was transferred to the aldehyde solution under Ar. Three drops of glacial acetic acid was added followed by dropwise addition of a degassed solution of sodium cyanoborohydride (3 mmol) in 5 mL methanol. The resulting clear, red solution was refluxed for 1 hour and then stirred at room temperature for 24 hours. 1 M HCl was added to the solution until it reached pH 4. The solution was then evaporated to dryness and dissolved in 25 mL of saturated Na₂CO₃ solution and finally extracted with chloroform. The organic layers were combined, dried with Na₂SO₄, and filtered through celite. The solvents were removed under vacuum to yield a red oil. The ligand **3** was then purified using silica gel chromatography with 9:1 DCM:MeOH. The desired compound eluted first and the solvent was removed under vacuum to give 540 mg of the pure product in 62% yield (1.85 mmol). ¹H NMR (CDCl₃): δ 8.58 (d, 2H), δ 8.12 (d, 1H), δ 8.05 (2, 1H), δ 7.66 (t, 2H), δ 7.30 (d, 2H), δ 7.21 (t, 2H), δ 6.95 (d, 1H), δ 3.93 (s, 4H), δ 3.85 (s, 2H). ¹³C NMR (CDCl₃): δ 164.27, δ 157.71, δ 148.69, δ 139.68, δ 137.06, δ 126.54, δ 125.61, δ 123.52, δ

123.08, δ 122.41, δ 117.17, δ 58.67, δ 56.10. m/z for $C_{19}H_{18}N_4O_3H^+$ expected = 351.15, found = 351.1 (see Appendix A).



Scheme 2.4. Scheme for synthesis of **4**.

[FeCl₂(L₂)] (**4**)

The complex was synthesized using a modified literature procedure (Scheme 2.4).¹⁰ Ligand **3** (0.6 mmol) and triethylamine (0.6 mmol) were dissolved in 10 mL of MeOH and degassed under Ar. FeCl₃·6H₂O (0.6 mmol) was dissolved in 10 mL of MeOH and also degassed under Ar. The ligand solution was transferred to the flask containing the FeCl₃ solution using air-free techniques. The solution immediately became a deep purple color with a visible precipitate. The reaction was stirred at room temperature for 1 hour and then filtered. The filtrate was evaporated to dryness and washed with cold MeOH to give the product as a purple solid in 41% yield (118 mg). Crystals suitable for X-ray diffraction were grown by diffusion of diethyl ether into a solution of **4** in dichloromethane. m/z for $C_{19}H_{17}Cl_2FeN_4O_3Na^+$ expected = 497.991934, found = 497.992060. Anal'd calc'd for 2: C, 47.83; H, 3.80; N, 11.74. Found: C, 47.77, H, 3.83, N, 11.90 (Appendix A)

Electrochemistry Experiments

Cyclic Voltammetry (CV)

All electrochemistry experiments were performed under an Ar atmosphere using a CH Instruments 620D potentiostat. Cyclic voltammograms were acquired using a standard three-electrode cell. A saturated calomel reference electrode (SCE) was used for all experiments unless noted otherwise. Prior to each acquisition, the glassy carbon working electrode and the platinum auxiliary electrode were polished using 0.05 μm alumina powder paste on a cloth-covered polishing pad, followed by rinsing with water and acetonitrile. Ferrocene was used as an internal standard to correct for drifting of the reference electrode and changes in concentration, and all potentials are reported relative to the ferrocenium/ferrocene (Fc^+/Fc) redox couple.

Acid Addition Study

In an electrochemical cell, 0.2-0.5 mg of crystals of **2** or **4** were dissolved in 5.0 mL of acetonitrile (CH_3CN). 0.1 M TBAPF_6 was added as the supporting electrolyte. The cell was degassed with Ar for 15 minutes. Cyclic voltammograms (CVs) were taken without acid and after additions of 10 μL , 20 μL , 30 μL , 40 μL , and 50 μL of 1.1 M trifluoroacetic acid (TFA) unless otherwise noted. The CV were performed at varying ranges of potentials adjusted for each catalyst, generally at a scan rate of 200 mV/s unless noted otherwise. Prior to each scan, the working and auxiliary electrodes were polished as described above.

Catalyst Concentration Study

A stock solution of 0.1 M of **4** in CH_3CN was prepared. A 5 mL solution of 0.1 M TBAPF_6 in CH_3CN was prepared in an electrochemical cell and 200 μL of 1.1 M TFA (44 mM) was added. The solution in the cell was then degassed under Ar. CVs were taken at $\nu = 200$ mV/s without

any catalyst added, then after addition of 0.2, 0.4, 0.6, 0.8, and 1.0 mM catalyst from the stock solution of **4**.

Scan Rate Dependence Study

In an electrochemical cell, 1.0 mg of **4** was dissolved in 5.0 mL of 0.1 M TBAPF₆ in CH₃CN with 8.8 mM TFA. Cyclic voltammograms were taken at scan rates ranging from $\nu = 8$ V/s to 12 V/s to determine the scan rate at which catalysis is no longer diffusion limited.

Controlled Potential Coulometry

Controlled potential coulometry (CPC) was conducted to assess the robustness of the catalyst as well as to confirm the generation of hydrogen gas in the systems. The study was performed in a closed four-neck 500 mL round-bottom flask using vitreous carbon working and counter electrodes and a Ag wire reference electrode separated by porous VYCOR frits. A continuous potential at the voltage of catalysis was applied to the system for 1800 seconds, after which the headspace gases of the cell were analyzed. A CH Instruments 620D potentiostat combined with a CH Instruments 680 amp booster was used for the CPC. Gas analysis for H₂ was performed using a Bruker Scion 436 gas chromatograph equipped with a TCD using Ar carrier gas and calibrated with H₂/CH₄ gas mixtures of known composition.

Activity in Aqueous Mixtures

In an electrochemical cell, 1.0 mg of **4** was dissolved in 5.0 mL of 0.1 M TBAPF₆ in CH₃CN and degassed under Ar. CVs were taken at $\nu = 200$ mV/s without acid, after addition of 11 mM TFA in dry conditions, and in the presence of 100, 200, 300, and 400 μ L of DI water.

Background Reduction of TFA

In an electrochemical cell, 8.8 mM TFA in 5.0 mL of 0.1 M TBAPF₆ in CH₃CN was degassed with Ar. CVs were taken at $\nu = 200$ mV/s prior to addition of catalyst, and after addition of 0.05 mM **4** (see in Appendix A)

Results and Discussion

Characterizing the Nitro-Functionalized Complex (4)

Crystals suitable for X-ray diffraction were obtained via slow diffusion of diethyl ether into a solution of **4** in DCM. The structure of **4** is a distorted octahedral complex, with the Fe(III) metal center bound to the two chlorine ligands and the ligand **1** (Figure 2.5). The iron(III) complex has a high-spin d^5 electronic configuration, confirmed by Mössbauer spectroscopy (Appendix A). Distortion of the octahedral structure is evident in the O-Fe-N and N-Fe-N bonds, with bond angles of 163.7° and 73.9° , respectively. Typical octahedral complexes display axial position bond angles of 180° and equatorial angles of 90° .

The deviation from typical octahedral geometry likely occurs due to the formation of the 6-membered chelate ring from bonding of the phenolate to the metal center. The length of the Fe-O bond is 1.945 \AA , consistent with bond lengths typically reported for Fe(III)-phenolate bonds.^{4, 10, 11} Bond lengths and angles are shown in Table 2.1 and X-ray

crystallography data is shown in Table 2.2 for reference.

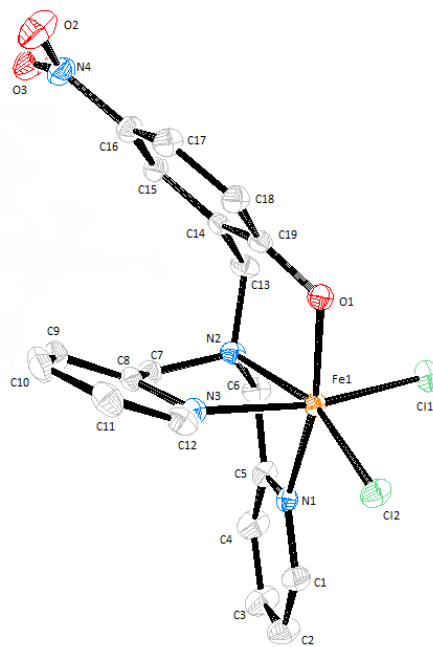


Figure 2.5. ORTEP diagram of **4** with Fe (orange), O (red), N (blue), Cl (green), and C (black). Hydrogen atoms are omitted for clarity and ellipsoids are at the 50% probability level.

Table 2.1. Bond lengths [\AA] and angles [$^\circ$] for **4**.

Bond Length (\AA)	
Fe(1)-O(1)	1.945(5)
Fe(1)-N(2)	2.184(6)
Fe(1)-N(1)	2.186(6)
Fe(1)-N(3)	2.227(7)
Fe(1)-Cl(4)	2.282(2)
Fe(1)-Cl(3)	2.316(2)

Bond Angle ($^\circ$)	
O(1)-Fe(1)-N(2)	82.8(2)
O(1)-Fe(1)-N(1)	163.7(2)
N(2)-Fe(1)-N(1)	93.2(2)
O(1)-Fe(1)-N(3)	89.8(2)
N(2)-Fe(1)-N(3)	76.3(2)
N(1)-Fe(1)-N(3)	73.9(2)

Table 2.2. Crystal data and structure refinement for **4**

Empirical formula	C ₂₀ H ₂₁ Cl ₄ Fe N ₄ O ₄	
Formula weight	579.06	
Temperature	100(2) K	
Wavelength	1.54178 Å	
Crystal system	Orthorhombic	
Space group	P c a 21	
Unit cell dimensions	a = 14.7198(4) Å	a = 90°.
	b = 12.8174(3) Å	b = 90°.
	c = 12.5061(3) Å	g = 90°.
Volume	2359.52(10) Å ³	
Z	4	
Density (calculated)	1.630 Mg/m ³	
Absorption coefficient	9.609 mm ⁻¹	
F(000)	1180	
Crystal size	0.38 x 0.11 x 0.10 mm ³	
Theta range for data collection	3.448 to 69.839°.	
Index ranges	-17<=h<=17, -15<=k<=15, -10<=l<=15	
Reflections collected	15533	
Independent reflections	3348 [R(int) = 0.0406]	
Completeness to theta = 67.679°	99.8 %	
Refinement method	Full-matrix least-squares on F ²	
Data / restraints / parameters	3348 / 295 / 305	
Goodness-of-fit on F ²	1.051	
Final R indices [I>2sigma(I)]	R1 = 0.0560, wR2 = 0.1596	
R indices (all data)	R1 = 0.0582, wR2 = 0.1613	
Absolute structure parameter	0.040(7)	
Extinction coefficient	0.0024(4)	
Largest diff. peak and hole	1.066 and -1.286 e.Å ⁻³	

It was of interest to probe **4** for its usefulness as an electrocatalyst and to compare its activity to **2**. Cyclic voltammograms (CVs) of **4** show a reversible $\text{Fe}^{\text{III}}/\text{Fe}^{\text{II}}$ redox couple at -0.45 V vs. Fc^+/Fc (Figure 2.6). A peak separation of 72 mV is observed, typical of what is reported for the Fc^+/Fc internal standard that was used in all experiments (Appendix A). This separation indicates that the peak corresponds to a one electron redox event. Interestingly, the redox couple for **4** occurs at a potential 100 mV more positive than the corresponding $\text{Fe}^{\text{III}}/\text{Fe}^{\text{II}}$ redox couple of **2** (Figure 2.7). Because of this large, positive shift of the nitro-functionalized complex relative to the parent complex (**2**), we reasoned that **4** would reduce protons with an overpotential approximately 100 mV lower than **2**.

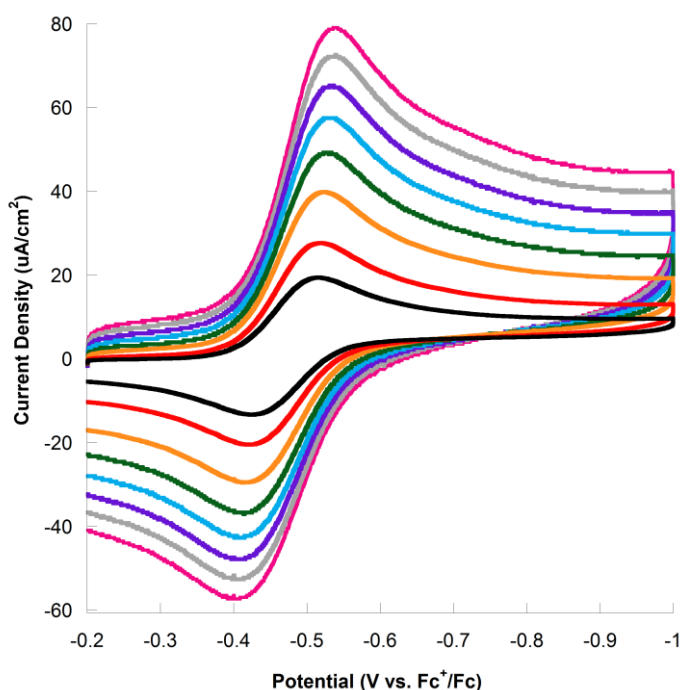


Figure 2.6. CVs of 1.0 mg of **4** in 5 mL acetonitrile with 0.1 M TBAPF_6 at scan rates of 50 mV/s (black), 100 mV/s (red), 200 mV/s (orange), 300 mV/s (green), 400 mV/s (blue), 500 mV/s (purple), 600 mV/s (gray) and 700 mV/s (pink).

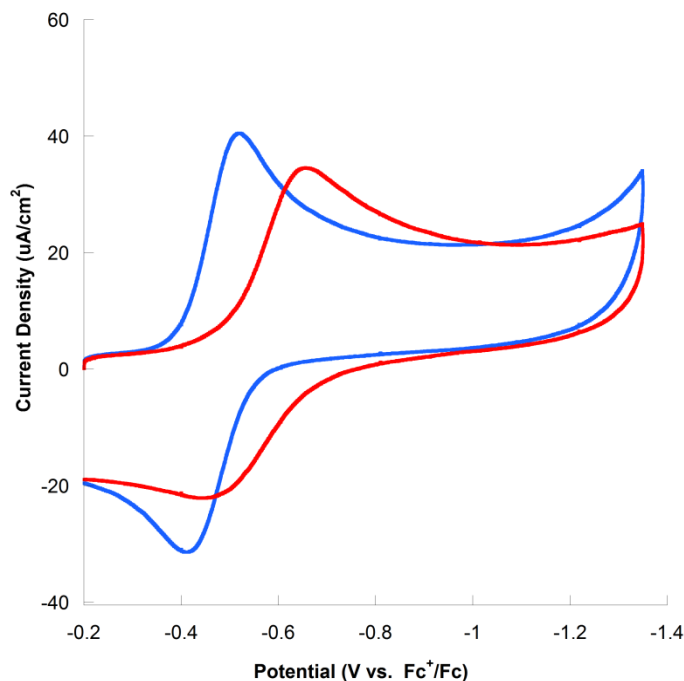


Figure 2.7. CVs of 1.0 mg of **2** (red) and **4** (blue) in 5 mL acetonitrile with 0.1 M TBAPF₆ at scan rates of 200 mV/s.

Assessing Kinetics and Catalytic Activity

CV studies conducted by adding increasing amounts of weak acid (proton source) reveal whether a complex is catalytically active for hydrogen generation. Upon addition of known aliquots of 1.1 M trifluoroacetic acid (TFA) to a solution of **4** in acetonitrile with TBAPF₆ as electrolyte, an irreversible catalytic wave for **4** occurs at -1.18 V vs. Fc⁺/Fc, a potential that is 400 mV more positive than that of **2**. The peak current (i_c) increases linearly with increasing additions of acid, suggesting that catalysis is second order with respect to [H⁺] (Figure 2.8). This second order dependence is determined from the relationship between [H⁺] and peak current, and this correlation is discussed further in Appendix A.^{5b}

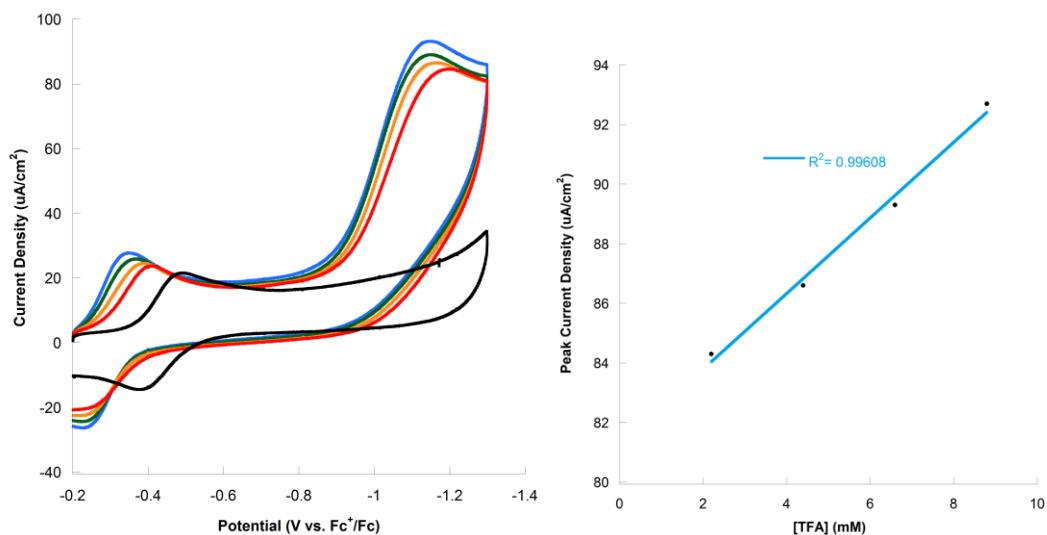


Figure 2.8. *Left:* CVs of 0.3 mg of **4** in 5 mL of 0.1 M TBAPF₆ in CH₃CN at $v = 200$ mV/s without acid added (black) and upon the addition of 2.2 mM (red), 4.4 mM (orange), 6.6 mM (green), and 8.8 mM (blue) TFA. A catalytic reduction is visible at -1.18 V vs. Fc⁺/Fc with an i_c/i_p of 5.32.

Right: Peak Current Density vs. [TFA]. The linear correlation between PCD and proton concentration ($R^2 = 0.996$) indicates a second order reaction with regards to [H⁺].

Additionally, as increasing amounts of catalyst are added to a fixed amount of TFA in acetonitrile solution, the catalytic reduction event is still observed at -1.18 V vs. Fc⁺/Fc (Figure 2.9). Current enhancement increases linearly with increasing concentration of catalyst, indicating that catalysis is first order with respect to [**4**]. Determination of the dependence on [H⁺] and [catalyst] give rise to an overall rate expression of $\text{rate} = k[\mathbf{4}][\text{H}^+]^2$. This expression is in accordance with that of previously reported **2**.^{4, 5, 10}

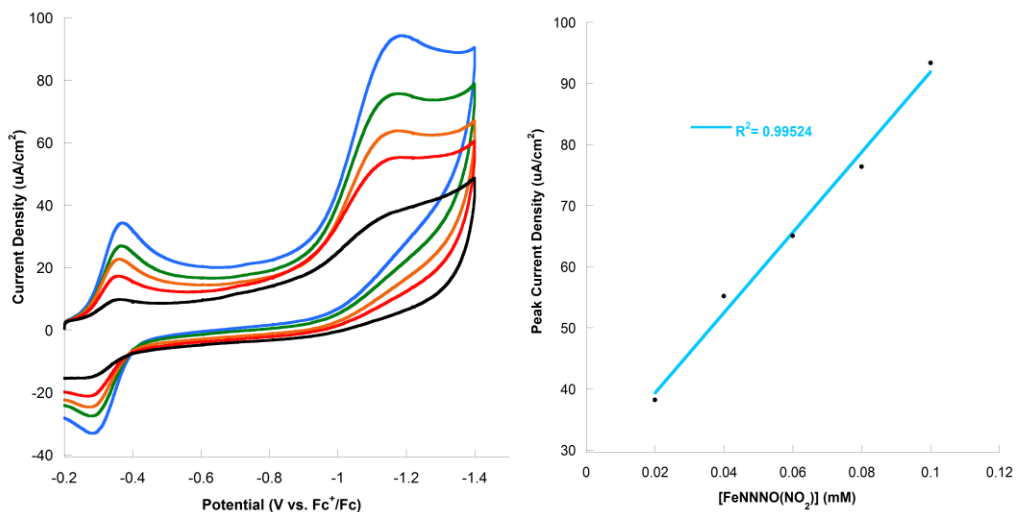


Figure 2.9. *Left:* CVs in CH₃CN with 0.1 M TBAPF₆ containing 44 mM TFA with 0.2 mM **4** (black), 0.4 mM **4** (red), 0.6 mM **4** (orange), 0.8 mM **4** (green), 1.0 mM **4** (blue) at $v = 200$ mV/s. *Right:* Peak Current Density vs. [TFA]. The linear correlation between PCD and catalyst concentration ($R^2 = 0.995$) indicates a first order reaction with regards to [**4**].

Cyclic voltammetry is a useful tool for evaluating the catalytic activity and kinetic mechanism of catalysts for reduction or oxidation events. The i_c/i_p is a commonly employed approach to assess the activity of a catalyst using CV. The method for determining i_c/i_p from CV data is shown in Figure 2.10, with a sample calculation shown below. Figure 2.10 is an example CV from an acid addition experiment with **4**. The black trace shows a scan of complex **4**, revealing its characteristic reversible Fe^{III}/Fe^{II} redox couple at -0.45 V vs. Fc⁺/Fc. Upon addition of acid, the blue trace displays the appearance of an irreversible reduction event at -1.18 V vs. Fc⁺/Fc, corresponding to a proton reduction event. The catalytic activity is taken to be a ratio of the peak height of the irreversible catalytic wave (i_c) and the peak height of the catalytic reduction wave (i_p); the larger the i_c/i_p , the more active a catalyst is for proton reduction.⁴

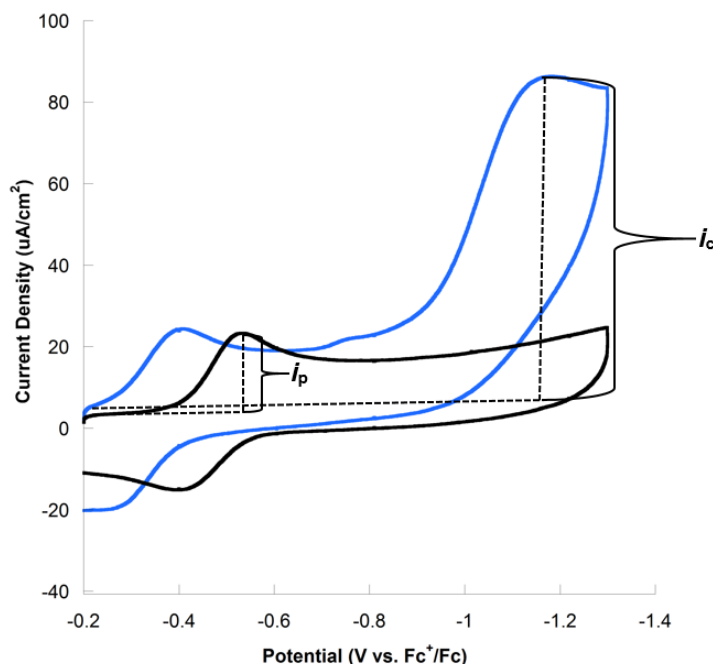


Figure 2.10. CVs of 0.3 mg of **4** in 5 mL of 0.1 M TBAPF₆ in CH₃CN before (black) and after (blue) the addition of 8.8 mM TFA at $\nu = 200$ mV/s.

The activity of the catalyst (i_c/i_p) may be further used to determine the turnover frequency (TOF) of the reaction using the following expression (Equation 2.1):¹⁶

$$\frac{i_c}{i_p} = \frac{n}{0.4463} \sqrt{\frac{RTk_{obs}}{F\nu}} \quad (2.1)$$

In equation 2.1, n is the number of electrons catalyzed during a reaction, R is the gas constant, T is temperature (K), F is the Faraday constant (96485 A/mol), and ν is scan rate (V/s). By solving the expression for k_{obs} , it is possible to determine the TOF. Although this method of solving for TOF is generally used for simple pseudo-first order systems with EC' mechanisms, it may be used as a means of comparing TOF of electrocatalysts that may operate under more complex mechanisms and therefore may be used as a point of comparison to other literature examples.^{4,17}

In order to report the most accurate TOF, the experiment must be conducted at a scan rate at which the reaction is not diffusion limited. Studies conducted varying the scan rate from $\nu = 8$

V/s to 12 V/s show a plateau at rates above 10 V/s, indicating that at 10 V/s catalysis by **4** becomes independent of scan rate (Figure 2.11). An acid addition experiment was therefore conducted at a scan rate of 10 V/s to determine a more accurate i_c/i_p value (Figure 2.12). The i_c/i_p at $\nu = 10$ V/s was determined to be 5.32, taking into account the effects of dilution of the substrate upon additions of TFA to the system (Equation 2.2).

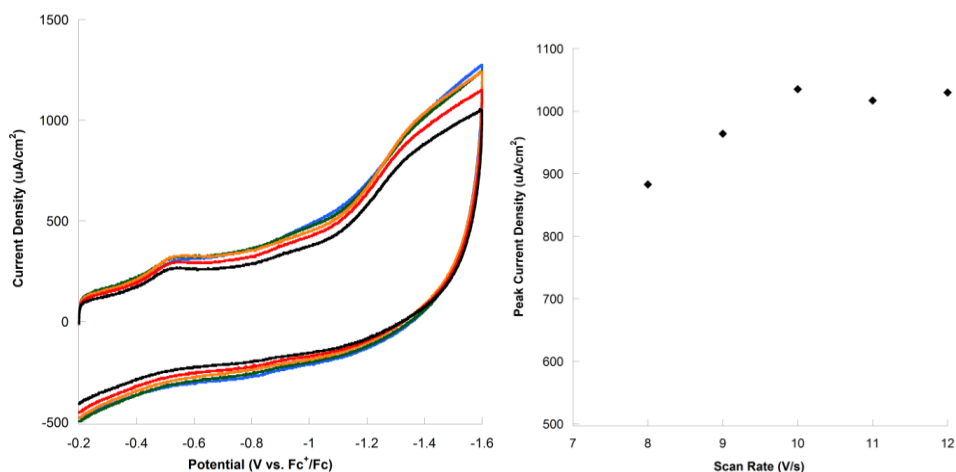


Figure 2.11. *Left:* CVs of 1.0 mg **4** in 5 mL of CH₃CN with 0.1 M TBAPF₆ with 8.8 mM TFA at scan rates of 8 V/s (black), 9 V/s (red), 10 V/s (orange), 11 V/s (green), and 12 V/s (blue).

Right: Plot of peak current density vs. scan rate shows that i_c becomes independent of scan rate at $\nu \geq 10$ V/s.

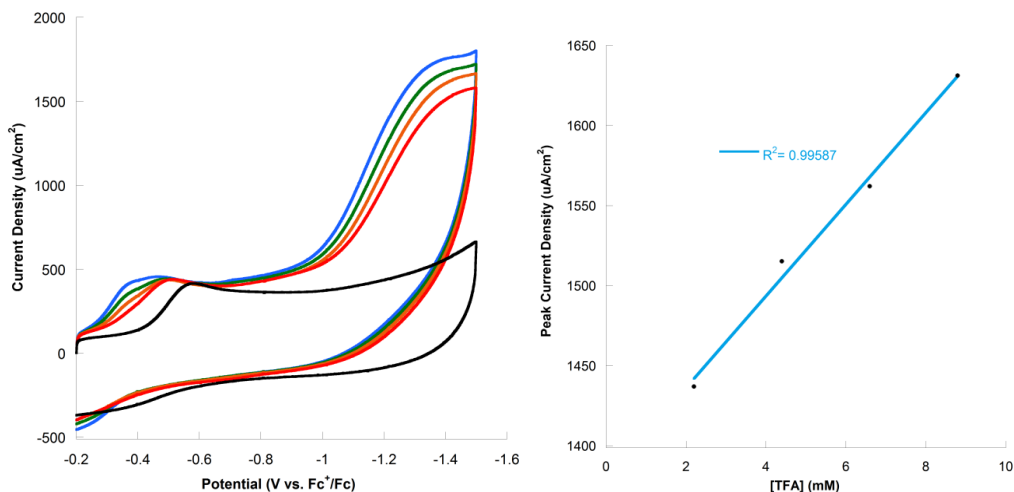


Figure 2.12. *Left:* CVs of 0.2 mg of **4** in 5 mL of 0.1 M TBAPF₆ in CH₃CN at $v = 10$ mV/s without acid added (black) and upon the addition of 2.2 mM (red), 4.4 mM (orange), 6.6 mM (green), and 8.8 mM (blue) TFA. *Right:* Peak current density vs. [TFA]. The linear correlation between PCD and proton concentration ($R^2 = 0.996$) indicates a second order reaction with regards to $[H^+]$.⁴

$$i_p = 2.18 \times 10^{-5} A$$

$$i_c = 1.15 \times 10^{-4} A$$

Correction for solvent dilution:¹²

$$\text{Dilution factor: } i_p \times \frac{vol_i}{vol_f} \quad (2.2)$$

$$(2.18 \times 10^{-5} A) \times \left(\frac{5.00 \text{ mL}}{5.04 \text{ mL}} \right) = 2.16 \times 10^{-5} A$$

$$\frac{i_c}{i_p} = \frac{(1.15 \times 10^{-4} A)}{(2.16 \times 10^{-5})} = 5.32$$

With this more accurate i_c/i_p value, the TOF (k_{obs}) was thus calculated to be 558 s^{-1} (Equation 2.3):⁸

$$k_{obs} = \left(\frac{i_c}{i_p} \times \frac{0.4463}{n} \right)^2 \times \left(\frac{Fv}{RT} \right) \quad (2.3)$$

$$k_{obs} = \left(5.32 \times \frac{0.4463}{2} \right)^2 \times \left(\frac{96485 \text{ C/mol} \times 10 \text{ V/s}}{8.314 \text{ J/Kmol} \times 293 \text{ K}} \right) = 558 \text{ s}^{-1}$$

Assessing Catalytic Efficiency

In addition to assessing a catalyst's activity, it is important to evaluate the efficiency of the system for proton reduction. The efficiency of a complex may be measured and compared to other catalysts reported by determination of overpotential. Overpotential is a thermodynamic parameter that refers to the additional potential, beyond the thermodynamic requirement for proton reduction, needed to drive a reaction at a specific rate.¹⁴ The overpotential may be determined by taking the difference between the half-wave potential ($E_{1/2}$) of the catalytic reduction event and a reference potential of the selected proton source (E_{ref}) (Figure 2.13).^{14, 15} E_{ref} is the reduction potential of a given proton source that takes into account the effects of homoconjugation commonly exhibited by acids such as TFA in acetonitrile.^{11, 14} Homoconjugation occurs when the conjugate base of an acid, in this case trifluoroacetate, is stabilized by hydrogen bonding to the acid.^{14, 15} This effect magnifies the acidity of the proton source at higher concentrations and may lead to overestimation of catalytic activity and imprecise overpotential measurements if left unconsidered.^{14, 15}

Although homoconjugation is a known problem when using TFA, this weak acid was selected as the proton source in these studies because of its low background reduction at potentials where catalytic activity is shown (Appendix A).¹⁴ To confirm the catalytic activity observed, CVs were also run tosic acid as the proton source (Appendix A). These experiments showed similar catalytic activity for **4** to those conducted with TFA.

To calculate the overpotential of complex **4**, the reference potential of 10 mM TFA in CH_3CN was subtracted from the half-wave potential of the irreversible reduction event. The half-wave potential of **4** was found to be -0.97 V vs. Fc^+/Fc using the method illustrated in Figure

2.13. The reference potential for 10 mM TFA in CH₃CN, obtained from literature values, was -0.68 V vs. Fc⁺/Fc. This allowed for calculation of overpotential for **4** (Equation 2.4):^{8, 15}

$$\begin{aligned} \text{Overpotential} &= \left| E_{\frac{1}{2}} - E_{\text{ref}} \right| \quad (2.4) \\ &= |(-0.97 \text{ V vs. Fc}^+/\text{Fc}) - (-0.68 \text{ V vs. Fc}^+/\text{Fc})| \\ &= 0.290 \text{ V} = 290 \text{ mV} \end{aligned}$$

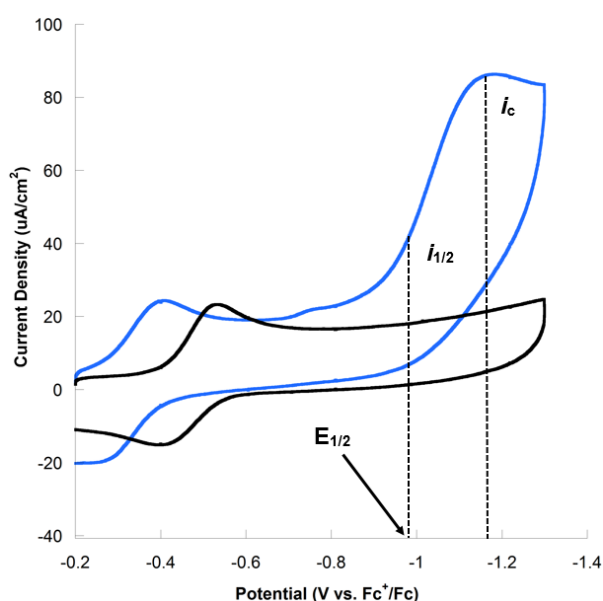


Figure 2.13. CVs of 0.3 mg of **4** in 5 mL of 0.1 M TBAPF₆ in CH₃CN before (black) and after (blue) the addition of 8.8 mM TFA at $v = 200$ mV/s.

An overpotential of approximately 300 mV for **4** compares very favorably to previously reported electrocatalysts in organic solvents.^{2, 4, 11} Compared with complex **2**, which shows an overpotential of 800 mV, this much lower overpotential highlights the success achieved by modification of ligand to tune catalytic abilities. However, while the overpotential is lowered, the catalytic activity is as well as **4** operates at a much lower i_c/i_p of 5.32 compared with catalyst **2** which has an i_c/i_p of 7.8 under identical conditions. The concurrent lowering of activity observed in these experiments is typical of complexes modified to achieve lower overpotentials.^{4, 13} The

nitro-functionalized derivative **4** also compares well to mononuclear iron electrocatalysts reported by Winkler and Ott in its very low overpotential and moderate catalytic activity.^{2,3}

Proposed Mechanism

CV also helped to elucidate the mechanism of the nitro-functionalized catalyst, which behaves similarly to complex **2**. A redox couple for $\text{Fe}^{\text{III}}/\text{Fe}^{\text{II}}$ appears at $-0.45\text{ V vs. Fc}^+/\text{Fc}$ prior to acid addition, and the redox couple shifts to $-0.28\text{ V vs. Fc}^+/\text{Fc}$ upon addition of TFA.⁸ Similar to the mechanism of **2**, this shift implies a chemical change to the catalyst as the first step of the catalytic mechanism, likely by protonation of the phenol (Figure 2.14). Following the first chemical step of the mechanism (protonation, C), the catalyst **4** undergoes subsequent electrochemical reduction (E) and protonation (C) steps resulting in a CECE or CEEC mechanism (Figure 2.15).

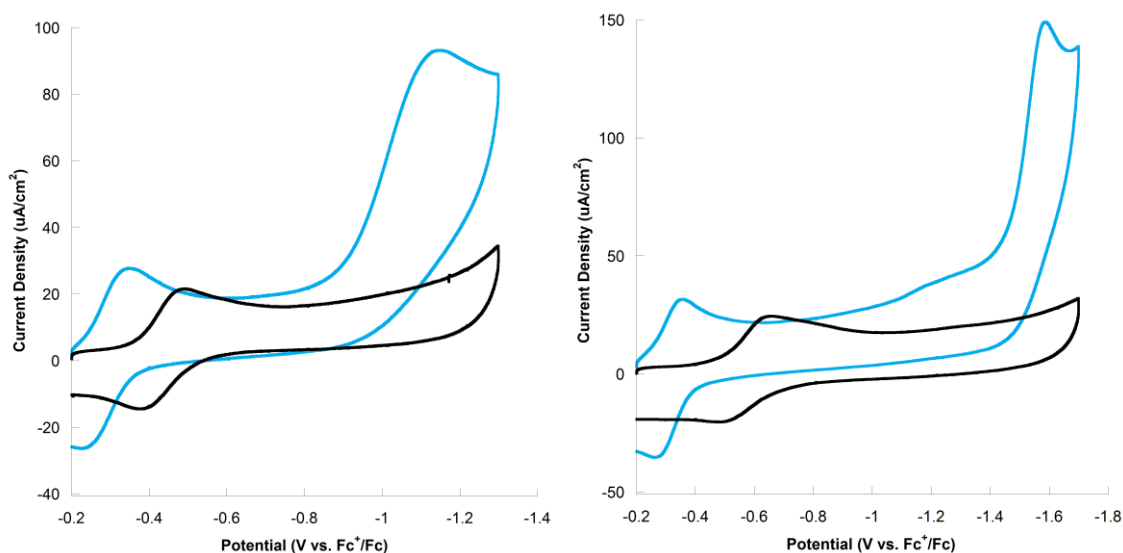


Figure 2.14. *Left:* CVs of **4** without added TFA (black) and with 8.8 mM TFA (blue). *Right:* CVs of **2** without added TFA (black) and with 8.8 mM TFA (blue).

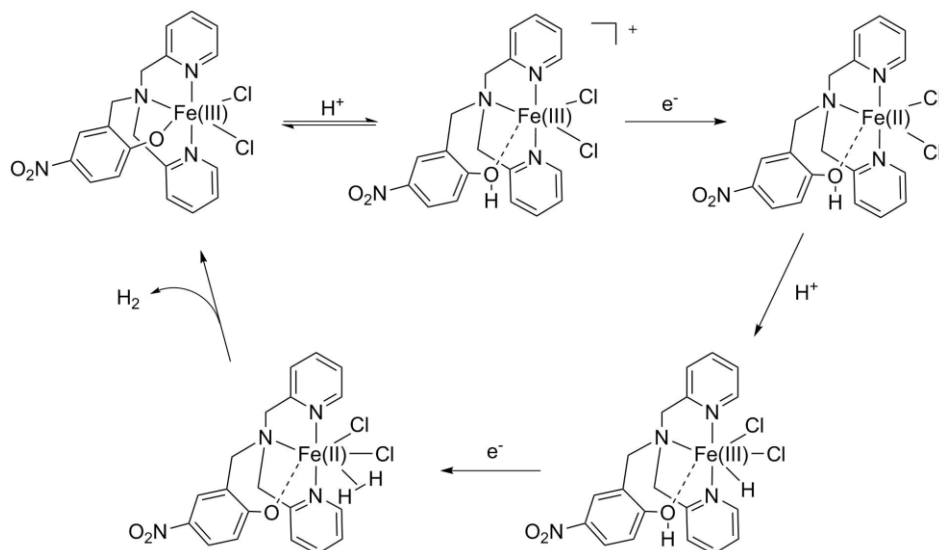


Figure 2.15. Proposed CECE mechanism for proton reduction by **4**.

Because the protonated versions of both **4** and **2** are reduced at -0.28 V vs. Fc^+/Fc , this indicates that the phenol group likely becomes hemilabile after protonation and leaves the same Fe-NNN core intact. The large shift of 400 mV in the catalytic reduction event of **4** compared to **2**, however, indicates that the electron-withdrawing nitro group greatly affects catalysis. Overall this suggests that the phenol group of **4** likely re-coordinates during later stages of the catalytic cycle as the presence of the nitro group makes the catalytic reduction potential less cathodic.

Assessing Stability

To assess the stability of **4** during electrocatalysis and confirm the generation of H_2 , a controlled potential coulometry (CPC) experiment was conducted. During CPC experiments, the working electrode is maintained at a constant potential while the resulting current is observed over a period of time. The potential was held at -1.2 V vs. Fc^+/Fc for 1800 seconds to confirm that the irreversible reduction wave corresponded to electrocatalytic proton reduction to generate hydrogen (Figure 2.16). The CPC resulted in a total charge of 33.34 C and gas chromatography

analysis of the headspace gases showed the evolution of 0.17 mmoles of hydrogen gas. This amount of hydrogen generation corresponded to an impressive Faradaic yield of 99% (see Appendix A).

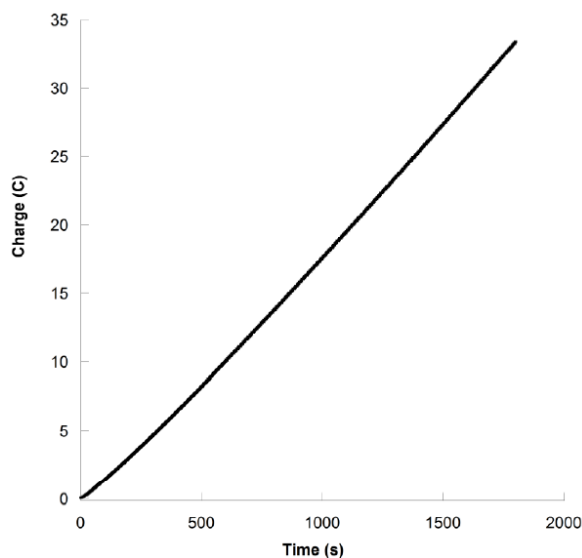


Figure 2.16. Controlled potential coulometry study of **4** in 0.1 M TBAPF₆ in acetonitrile with 65 mM TFA. The potential was held constant at -1.2 V vs. Fc⁺/Fc for 1800 seconds, yielding a charge of 33.34 C.

This Faradaic yield of nearly 100% illustrates the function of the catalyst to efficiently reduce protons using electrons in the system. This efficiency value illustrates the great efficiency of **4** and its overall potential for incorporation into devices for proton reduction.

Activity in Aqueous Mixtures

Because the ultimate goal is to develop systems that use water as its primary proton source, it is of interest to probe the activity of the catalysts in aqueous solution. Due to difficulties in solubility, experiments using **4** in purely aqueous solutions were limited. However, studies examining the effect of the presence of water on the system show that catalytic activity is enhanced (Figure 2.17). Upon addition of 100 μ L of water, the catalytic activity increases by

12% compared to that exhibited in dry acetonitrile. The activity is increasingly enhanced with subsequent additions of water until the catalyst begins to precipitate out of solution after addition of 400 μL , limiting the addition of more water.

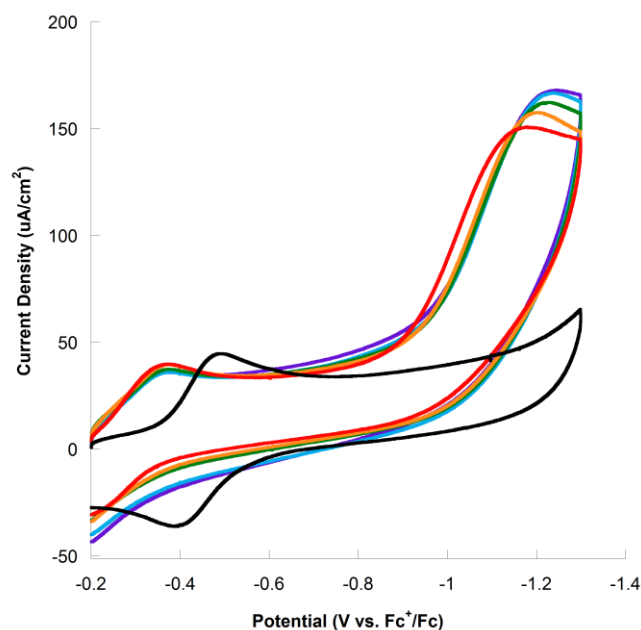


Figure 2.17. CVs of **4** in CH_3CN solution with 0.1M TBAPF_6 and 11 mM TFA in dry conditions (red) and in the presence of 100 μL of water (orange), 200 μL of water (green), 300 μL of water (blue) and 400 μL of water (purple). The black trace is a CV of **4** in dry acetonitrile in the absence of TFA.

The observed enhancement in catalytic activity may be attributed to the additional proton source available in solution upon addition of water. The cathodic shift of the reduction event observed upon adding water may be the result of a change in chemical environment from differences in proton solvation energies between acetonitrile and water.¹⁴ Overall, such studies illustrate the great potential for incorporation of **4** into devices for AP as the catalyst remains stable and active in the presence of water.

Conclusions

We have developed a family of highly active iron polypyridyl monophenolate complexes for proton reduction. Modification of the phenol group of the ligand resulted in a new catalyst that greatly reduces the overpotential of parent complex **2**. The nitro-functionalized catalyst **4** operates at an overpotential of 300 mV, compared to the previously reported catalysts overpotential of 800 mV. Additionally, complex **4** is active for proton reduction with a TOF of 550 s^{-1} . The catalyst is proposed to operate through either a CECE or CEEC mechanism as elucidated through cyclic voltammetry experiments and comparison to other proton reduction catalysts.^{4, 11} Catalysis is first order with respect to catalyst concentration, and second order with respect to proton concentration. Complex **4** shows an increase of in catalytic activity of 12% in the presence of water, suggesting that this family of catalysts may be viable for incorporation into aqueous systems for AP.

References

- 1) Bhugan, I.; Lexa, D.; Savéant, J. *J. Am. Chem. Soc.* **1996**, *118*, 3982-3983.
- 2) Rose, M.J.; Gray, H.B.; Winkler, J.R. *J. Am. Chem. Soc.* **2012**, *134*, 8310-8313.
- 3) (a) Kaur-Ghumaan, S.; Schwartz, L.; Lomoth, R.; Stein, M.; Ott, S. *Angew. Chem. Int. Ed.* **2010**, *49*, 8033-8036. (b) Nguyen, A.D.; Rail, M.D.; Shanmugam, M.; Fettinger, J.C.; Berben, L.A. *Inorg. Chem.* **2013**, *52*, 12847-12854.
- 4) Connor, G.P.; Mayer, K.J.; Tribble, C.S.; McNamara, W.R. *Inorg. Chem.* **2014**, *53*(11), 5408-5410.
- 5) (a) Bigi, J.P.; Hanna, T.E.; Harman, W.H.; Chang, A.; Chang, C.J. *Chem. Commun.* **2010**, *46*, 958-960. (b) Kugler, M.; Scholz, J.; Kronz, A.; Siewert, I. *Dalton Trans.* **2016**, *45*, 6974-6982.
- 6) Dempsey, J.L.; Brunschwig, B.S.; Winkler, J.R.; Gray, H.B. *Acc. Chem. Res.* **2009**, *42*, 1995.
- 7) Martin, D.J.; McCarthy, B.D.; Donley, C.L.; Dempsey, J.L. *Chem. Commun.* **2015**, *51*, 5290-5293.
- 8) Hartley, C.L.; DiRisio, R.J.; Chang, T.Y.; Zhang, W.; McNamara, W.R. *Polyhedron* **2015**, In press.
- 9) Mayilmurugan, R.; Visvaganesan, K.; Suresh, E.; Palaniandavar, M. *Inorg. Chem.* **2009**, *48*, 8771-8783.
- 10) Viswanathan, R.; Palaniandava, M.; Blasubramanian, T.; Muthiah, P.T. *Inorg. Chem.* **1998**, *37*, 2943.
- 11) Cavell, A.C.; Hartley, C.L.; Liu, D.; Tribble, C. S.; McNamara, W. R. *Inorg. Chem.* **2015**, *54* (7), 3325-3330.
- 12) Hoffert, W.A.; Roberts, J.A.S.; Bullock, R.M.; Helm, M.L. *Chem. Commun.* **2013**, *49*, 7767-7769.
- 13) Roy, S.; Bacchi, M.; Berggren, G.; Artero, V. *ChemSusChem* **2015**, *8*(21), 3632-3638.
- 14) Rountree, E.S.; McCarthy, B.D.; Eisenhart, T.T.; Dempsey, J.L. *Inorg. Chem.* **2014**, *53*, 9983-10002.
- 15) Fourmond, V.; Jacques, P.; Fontecave, M.; Artero, V. *Inorg. Chem.* **2010**, *49*, 10338-10347.
- 16) Bard, A.J.; Faulkner, L.R. *Electrochemical Methods: Fundamentals and Applications*, 2nd ed.; John Wiley & Sons: New York, 2001.
- 17) McCrory C.L.; Uyeda, C.; Peters, J.C. *J. Am. Chem. Soc.* **2012** *134*(6), 3164-3170.

Appendix A

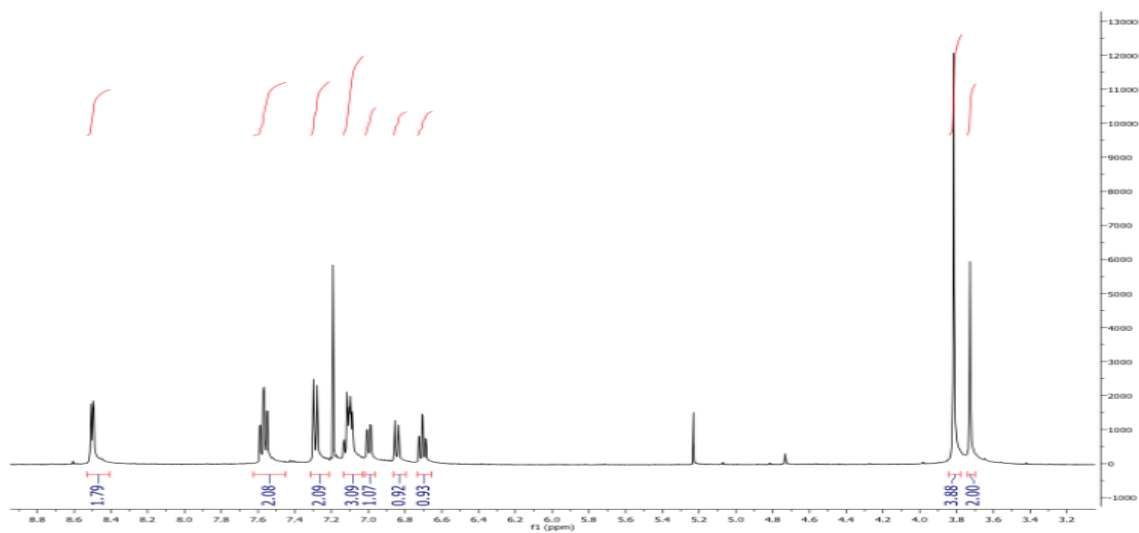


Figure A1. ¹H NMR Spectrum of **1** with integrations in blue.

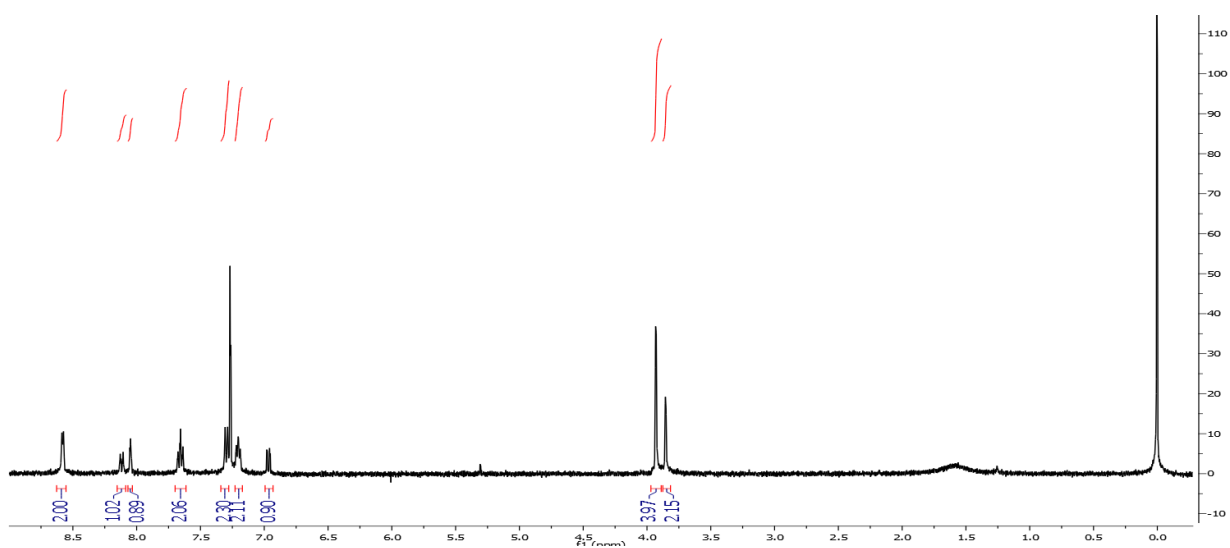


Figure A2. ¹H NMR Spectrum of **3** with integrations in blue.

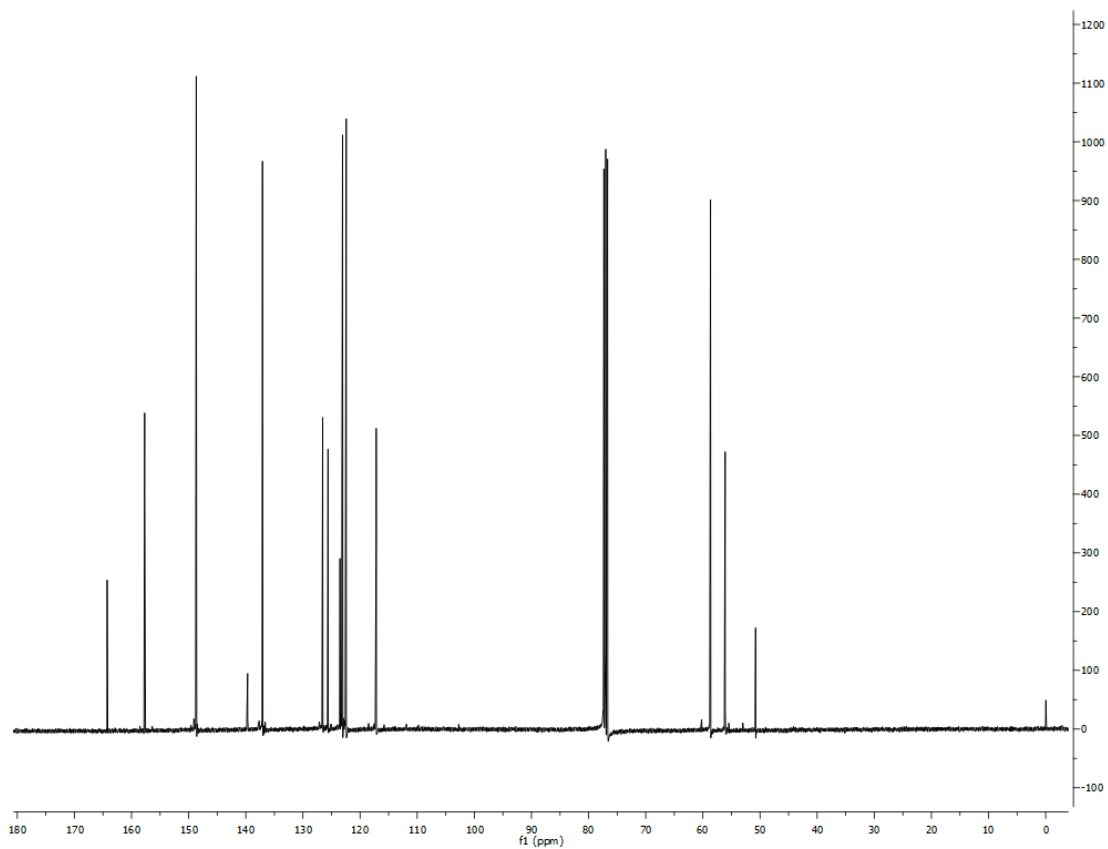


Figure A3. ^{13}C NMR of **3**.

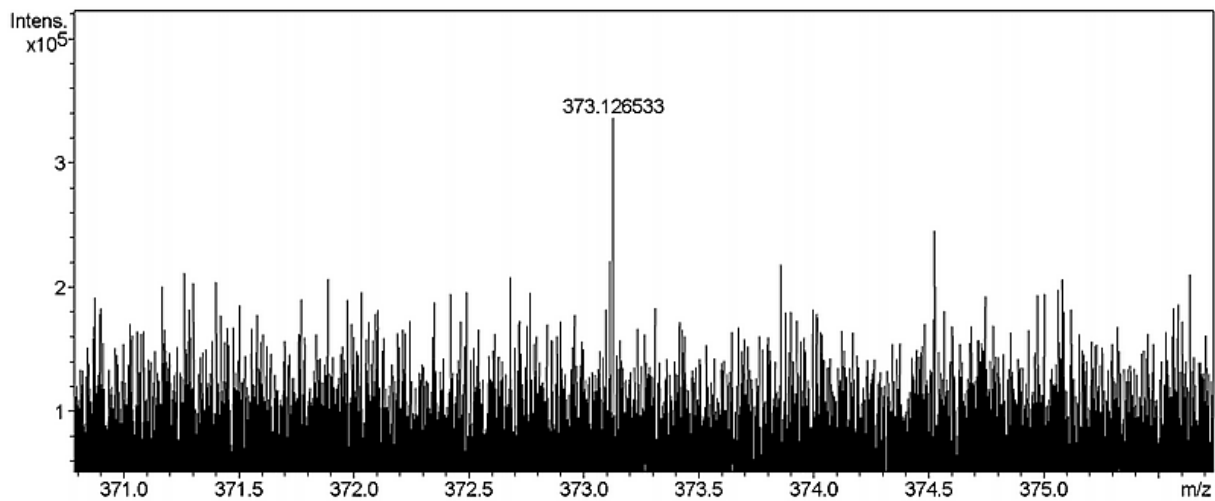


Figure A4. High-resolution of mass spectrum of complex **4** in 1:1 Methanol:THF with NaCl added.

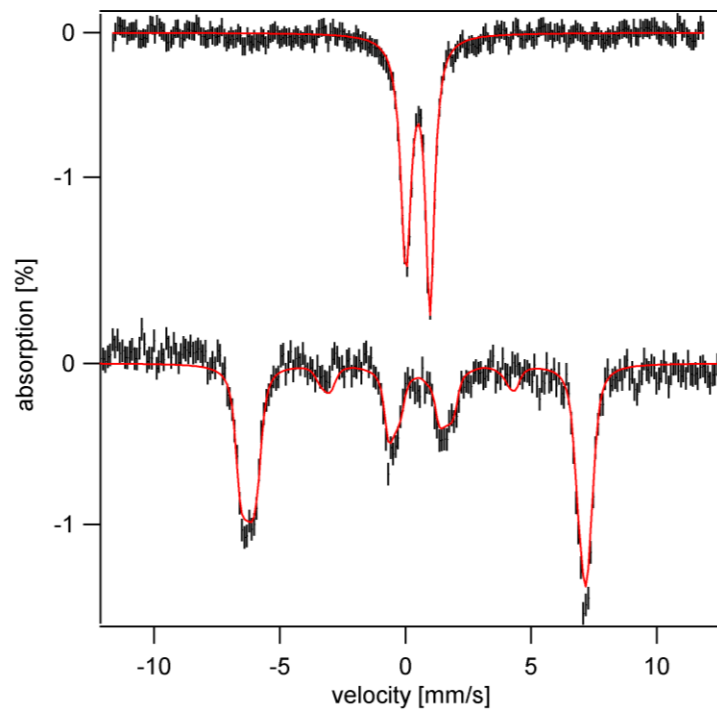


Figure A5. 4.2 K Mössbauer spectra of the complex **2** with zero applied field (top) and an applied field of 7.5 T (bottom), with the spectral simulation curves shown in red. The spectra confirm that the complex is d^5 high-spin.

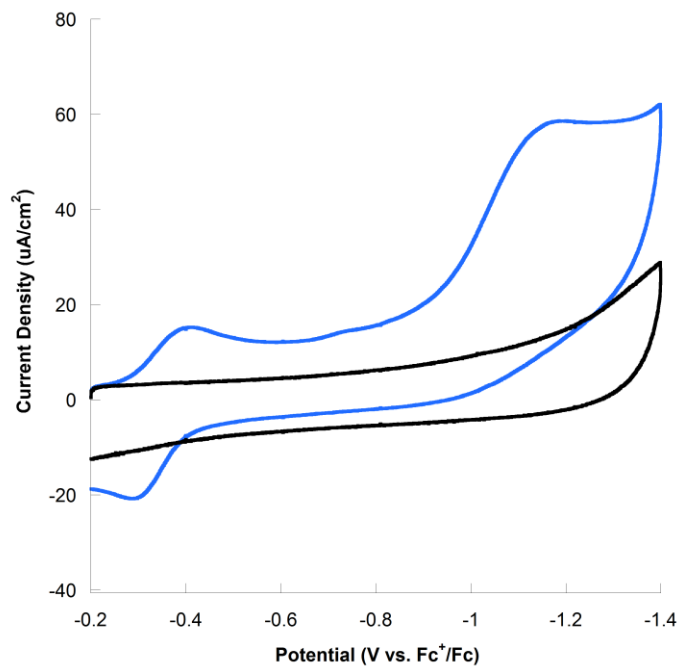


Figure A6. CV of 8.8 mM TFA in CH₃CN with 0.1 M TBAPF₆ prior to (black) and after (blue) the addition of 0.05 mM **4** at a scan rate of 200 mV/s. A reduction peak corresponding to the catalytic reduction of hydrogen is visible at -1.18 V vs. Fc⁺/Fc only upon addition of **4**.

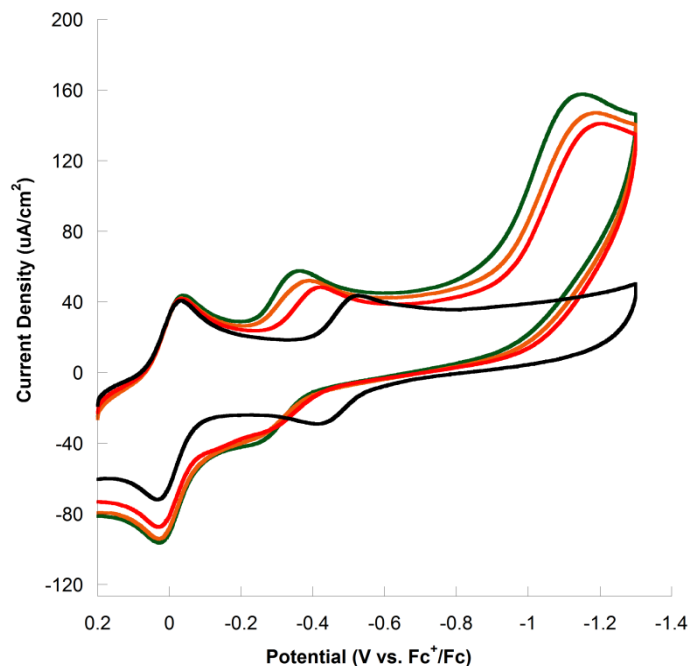


Figure A7. CVs of 0.5 mg of **4** and 0.2 mg ferrocene as an internal standard in 5 mL of 0.1 M TBAPF₆ in acetonitrile at a scan rate of $\nu = 200$ mV/s with no acid added (black), and with 2.2 mM (red), 4.4 mM (orange), and 6.6 mM (green) TFA. The redox couple of ferrocene appears at 0 V vs. Fc⁺/Fc.

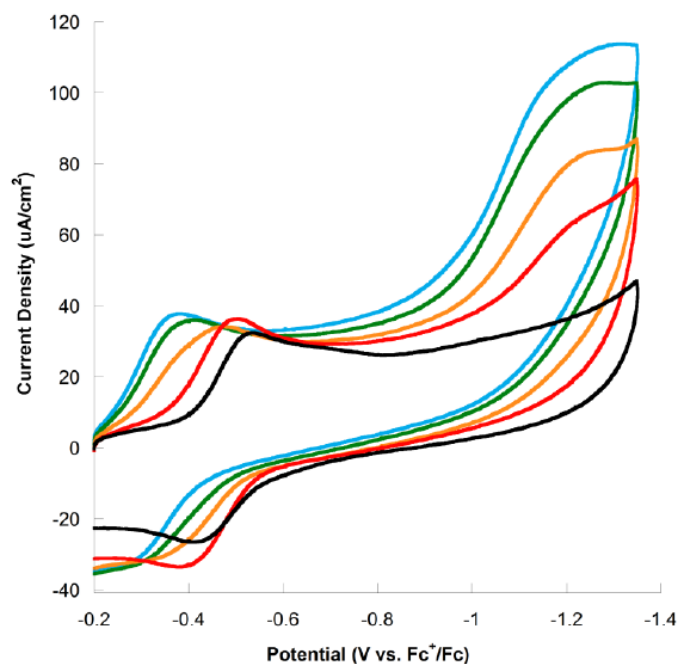


Figure A8. CVs of 0.3 mg of **4** in 5 mL of 0.1 M TBAPF₆ in acetonitrile at a scan rate of $\nu = 200$ mV/s with no acid added (black), and with 2.2 mM (red), 4.4 mM (orange), 6.6 mM (green), and 8.8 mM (blue) of Tosic acid.

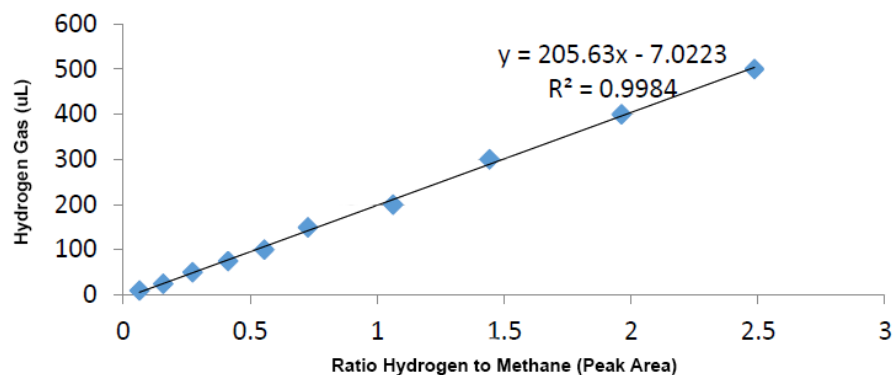


Figure A9. Calibration curve of H₂ to CH₄ peak areas used for determination of hydrogen generation. The ratio of peak areas was plotted against the volume of H₂ injected into the GC.

Calculation of Faradaic yield from CPC experiment:

A Faradaic yield of 99% was calculated for **4** by integrating the H₂ and CH₄ peaks from analysis of a sample of the headspace gases of the CPC experiment and using a GC calibration curve (Figure A9):

H₂ peak area: 200005

CH₄ peak area: 10709

$$y = 205.63 \left(\frac{200005}{10709} \right) - 7.0223 = 3833 \mu\text{L H}_2$$

$$\frac{3.83 \text{ mL H}_2}{22.4 \text{ L/mol}} = 0.171 \text{ mmol H}_2 \text{ generated}$$

Assuming 100% Faradaic yield, the generation of 33.34 C would correspond to 0.173 mmol H₂:

$$33.34 \text{ C} \left(\frac{1 e^-}{1.602 \times 10^{-19} \text{ C}} \right) \left(\frac{1 \text{ mol } e^-}{6.02 \times 10^{23} e^-} \right) \left(\frac{1 \text{ mol H}_2}{2 \text{ mol } e^-} \right) = 0.173 \text{ mmol H}_2$$

To determine the Faradaic yield, the ratio of the experimentally observed value to the theoretical value of H₂ produced was taken:

$$\left(\frac{0.171 \text{ mmol H}_2}{0.173 \text{ mmol H}_2} \right) \times 100 = 99\%$$

Determination of $[H^+]$ and [catalyst] dependence

Peak current (i_c) is defined as:^{5b}

$$i_c = F c_p \sqrt{D_p k c_A}$$

Where F is the Faraday constant, c_p is the catalyst concentration, c_A is the substrate concentration, D_p is the diffusion coefficient and k is the rate constant.

Chapter 3. Electrocatalysis with Sulfinato Complex

Introduction

After improving the overpotential of **2** by incorporating an electron-withdrawing nitro group, it was of interest to use a different approach to modify the polypyridyl ligand framework around the iron center to enhance catalytic activity. Studies with these complexes indicated that the catalytic mechanism for hydrogen generation likely operated by CECE or CEEC steps, with the dissociation of the protonated phenolate moiety as part of the rate-limiting step. We therefore reasoned that replacement of the phenolate with a functional group that would form a less favorable chelate ring would result in a ligand that dissociates faster, shortening the rate-limiting step, and would therefore increase the overall activity of the catalyst.

Inspiration for design of a more active complex was again derived from studying the active site of several naturally occurring enzymes. Much progress has been made over the past 20 years in development of enzyme active site mimics in addition to the [Fe]-hydrogenase, such as cysteine dioxygenase (CDO).¹⁻⁴ CDO is an enzyme that catalyzes the biosynthesis of pyruvate and taurine through S-oxygenation of cysteine (Figure 3.1).^{1,2} Relatively few CDO active site mimics have been

reported, and even fewer have been completely

characterized for

redox capabilities.^{1,2} The inclusion of a heteroatom such as S that might be bound to the metal center through a sulfinate moiety was also an intriguing means of tuning the ligand framework of **2** to obtain a highly active catalyst.

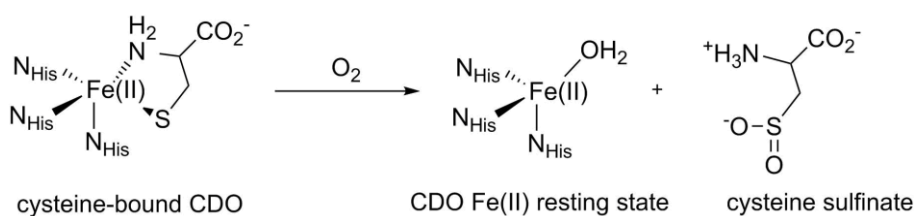


Figure 3.1. S-oxygenation of cysteine by CDO.²

This chapter presents the synthesis, characterization and electrochemical analysis of the first reported example of a sulfinato iron(III) catalyst (**6**) for proton reduction (Figure 3.2). The complex was

characterized by NMR, MS, UV-Vis and X-ray diffractometry techniques and

studied for its catalytic activity

using cyclic voltammetry. The effects of varying proton and catalyst concentrations as well as scan rate are investigated. The complex **6** is compared with the parent complex (**2**) and a catalytic mechanism for hydrogen evolution is proposed. The goal of this project is to ideally develop an analogue of **2** whose activity is enhanced without lowering efficiency, and to identify modes of improving molecular catalysts for proton reduction.

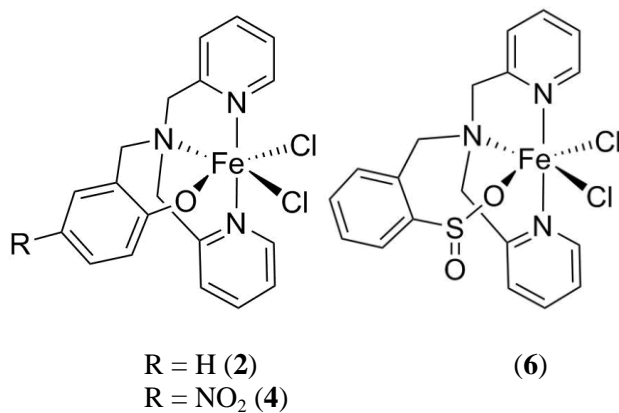


Figure 3.2. *Left:* Iron polypyridyl monophenolate complexes (**2**) and (**4**). *Right:* Iron polypyridyl sulfinate complex (**6**).

Experimental

Materials and methods

All syntheses were performed using standard air-free Schlenk techniques under an atmosphere of Ar unless otherwise indicated. All chemicals were purchased from Fischer Scientific and were used without further purification.

Instrumentation

^1H and ^{13}C NMR spectra were recorded on an Agilent 400MR DD2 spectrometer operating in the pulse Fourier transform mode and chemical shifts are referenced to residual solvent.

Elemental analysis was performed by the CENTC Elemental Analysis Facility at the University of Rochester, funded by NSF CHE-0650456. UV–Vis spectra were recorded using an Agilent Cary 60 UV–Vis Spectrophotometer using sealed quartz cuvettes degassed under Ar prior to scans.

X-Ray Diffraction

Single crystals of **6** were mounted on glass fibers and data was collected with graphite-monochromated Mo $K\alpha$ radiation on a Bruker SMART Apex II CCD platform diffractometer. The structure was solved using SIR20114 and refined using SHELXL 2014/7. The space group $P4_3$ was determined based on CSD statistics and having solved the structure in space groups $P1$ and $P2_1$ and noting the higher symmetry visually and via the Addsym function of program Platon. A direct-methods solution was calculated, which provided most non-hydrogen atoms from the E-map. Full-matrix least-squares/ difference Fourier cycles were performed, which located the remaining non-hydrogen atoms. Non-hydrogen atoms were refined using anisotropic

displacement parameters, and hydrogen atoms were placed in ideal positions and refined as riding atoms with relative isotropic displacement parameters.

Syntheses

Sulfinato Ligand Precursor (L₃, 5)

The ligand (5) was synthesized from thiosalicylic acid using a modified literature procedure.⁴

O-mercaptobenzyl alcohol

Thiosalicylic acid (0.02 mol) in 75 mL of dry diethyl ether was degassed under Ar. This was combined with LiAlH₄ (0.03 mol) under an Ar atmosphere and the solution was stirred for 1 hour at room temperature. The solution was then cooled in an ice bath and 4.0 mL DI H₂O was added dropwise, followed by 20 mL of 10% H₂SO₄. The solution was then stirred under argon for 48 hours. The reaction mixture was washed with diethyl ether (3x 30 mL), and the organic layer was dried using MgSO₄ and evaporated to yield o-mercaptobenzyl alcohol, a yellow oil. (82% yield) The ¹H and ¹³C NMR spectra matched reported values (Appendix B).⁴

3-(2-hydroxymethylphenylsulfanyl)propionitrile

A solution of o-mercaptobenzyl alcohol (7.12 mmol) in 15 mL ethanol was prepared and degassed with Ar. To this solution, NaOH (0.01 mol) in 5 mL H₂O and 10 mL ethanol was added. Bromopropionitrile (0.6 mL, 7.1 mmol) was added dropwise under Ar using air-free techniques, and the mixture was stirred for 5 hours at room temperature. The resulting solution was filtered and evaporated to yield an oily yellow solution. This was dissolved in 25 mL diethyl ether and washed with 10 mL 5% NaOH and 10 mL H₂O. The solution was then dried with MgSO₄ and evaporated to yield a white solid, 3-(2-

hydroxymethylphenylsulfanyl)propionitrile. The ^1H and ^{13}C NMR spectra matched reported values (Appendix B).⁴

3-(2-bromomethylphenylsulfanyl)propionitrile

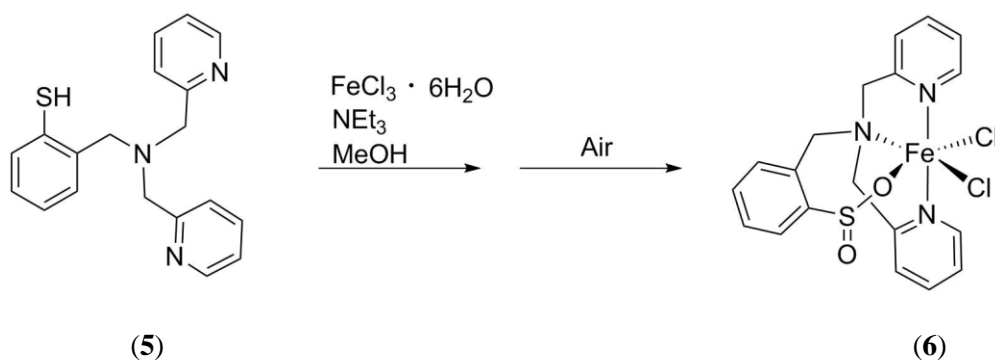
Solid 3-(2-hydroxymethylphenylsulfanyl)propionitrile (0.2739 g, 1.473 mmol) was dissolved in 22 mL of CH_2Cl_2 and degassed under Ar. This solution was added to a Schlenk flask using air-free techniques and the reaction cooled in an ice bath. 1.0 M PBr_3 (0.6 mmol) was added dropwise to the Schlenk flask under Ar and the solution stirred for 4 hours. The clear yellow-orange solution was washed with 10 mL 10% NaOH and 10 mL H_2O . The solution was then dried with MgSO_4 , filtered, and evaporated to yield 3-(2-bromomethylphenylsulfanyl)propionitrile as a clear yellow oil in 80% yield. The ^1H and ^{13}C NMR spectra matched reported values (Appendix B).⁴

N-(2-propionitrilemercaptobenzyl)-N,N-bis(2-pyridylmethyl)amine

3-(2-bromomethylphenylsulfanyl)propionitrile (0.347 g, 1.355 mmol) was dissolved in 20 mL ethyl acetate and degassed under Ar. This solution was added to a Schlenk flask, followed by the addition of a degassed solution of dipicolylamine (1.671 mmol) in 15 mL ethyl acetate. A degassed solution of trimethylamine (7.17 mmol) in 15 mL ethyl acetate was then also added to the solution. This stirred under Ar for 72 hours. The solution was then filtered and evaporated to yield N-(2-propionitrilemercaptobenzyl)-N,N-bis-(2-pyridylmethyl)amine. The product was purified through a silica gel column run in 7:3 EtOH:ethyl acetate and collected at a 59% yield. The ^1H and ^{13}C NMR spectra matched reported values (Appendix B).⁴

N-(2-mercaptobenzyl)-N,N-bis(2-pyridylmethyl)amine (5)

N-(2-propionitrilemercaptobenzyl)-N,N-bis-(2-pyridylmethyl)amine (40.7 mg, 0.112 mmol) was dissolved in 10 mL MeOH and degassed under Ar. The solution was then combined with NaOMe (9.7 mg, 0.180 mmol) in a Schlenk flask under an air-free environment. The solution was refluxed under Ar for 72 hours, and afterwards the resulting clear amber colored solution was filtered and then evaporated. The solid was dissolved in 13 mL DCM and extracted with 13 mL DI H₂O to quench any remaining NaOMe. The lower orange-brown organic layer was collected and evaporated to yield a brown oil. The ligand **5** was purified through use of a silica gel column in 9:1 DCM:MeOH. The purified N-(2-mercaptobenzyl)-N,N-bis(2-pyridylmethyl)amine (**5**) was collected at 45% yield as a brown oil. The ¹H and ¹³C NMR spectra matched reported values (Appendix B).⁴ ¹H NMR (CDCl₃): δ 8.51 (s, 2H), 7.50-7.67 (m, 4H), 7.10-7.37 (m, 7H), 3.87 (s, 2H), 3.80 (s, 4H). HR MS: m/z for (C₁₉H₁₉N₃S)⁺ expected = 322.137245 m/z found = 322.137527.



Scheme 3.1. Synthesis of **6**.

FeNNOSO Complex ([FeCl₂(L₃)], **6**)

The sulfinato complex (**6**) was synthesized according to the following procedure (Scheme 3.1):

The ligand (**5**) (0.100 g, 0.312 mmol) and triethylamine (0.312 mmol) were dissolved in 10 mL

of MeOH and degassed under Ar. $\text{FeCl}_3 \cdot 6\text{H}_2\text{O}$ (0.843 g, 0.312 mmol) was dissolved in 10 mL of MeOH and also degassed under Ar. The two solutions were then combined using air-free techniques to yield a brown solution with a visible precipitate. The reaction was stirred at room temperature for 12 hours and then filtered. The filtrate was evaporated and the resulting solid dissolved in DCM to remove impurities through recrystallization. Additional recrystallizations were performed in EtOH. A dark solid of complex **6** was collected with a 71% yield. Crystals suitable for X-ray diffraction were grown by slow diffusion of diethyl ether into a concentrated solution of **6** in CH_3CN . HR MS: m/z for $(\text{C}_{19}\text{H}_{18}\text{Cl}_2\text{FeN}_3\text{O}_2\text{S})\text{Na}^+$ expected = 500.973841 m/z found = 500.974354 (Appendix B). Anal. Calcd. for **6** $\text{FeC}_{19}\text{H}_{18}\text{Cl}_2\text{N}_3\text{O}_2\text{S}$: C, 47.63; H, 3.79; N, 8.77%. Found: C, 47.77; H, 4.12; N, 8.44%.

Electrochemistry Experiments

Cyclic Voltammetry

All electrochemistry experiments were performed under an Ar atmosphere using a CH Instruments 620D potentiostat. Cyclic voltammograms were acquired using a standard three-electrode cell. A saturated calomel reference electrode (SCE) was used for all experiments unless noted otherwise. Prior to each acquisition, the glassy carbon working electrode and the platinum auxiliary electrode were polished using 0.05 μm alumina powder paste on a cloth-covered polishing pad, followed by rinsing with water and acetonitrile. Ferrocene was used as an internal reference to correct for drifting of the SCE electrode and changes in concentration, and all potentials are reported relative to the ferrocenium/ferrocene (Fc^+/Fc) redox couple.

Acid Addition Study

In an electrochemical cell, 0.3-1.0 mg of crystals of **6** were dissolved in 5.0 mL of acetonitrile (CH_3CN) and 0.1 M TBAPF_6 was added as the supporting electrolyte. The cell was degassed under Ar for 15 minutes. Cyclic voltammograms (CVs) were taken without acid and after additions of 10, 20, 30, and 40 μL of 1.1 M trifluoroacetic acid (TFA) unless otherwise noted. The CVs were performed at a varied range of potentials adjusted for each experiment, generally at a scan rate of 200 mV/s. Prior to each scan, the working and auxiliary electrodes were polished as described above. Because homoconjugation is a known problem when using TFA, experiments were conducted using a similar procedure with 0.11 M tosic acid.

Catalyst Concentration Study

A 5.2 mM stock solution of **6** was prepared by dissolving 0.0125 g of crystalline **6** in CH_3CN in a 5 mL volumetric flask. A 5.0 mL solution of 0.1 M TBAPF_6 in CH_3CN was prepared in an electrochemical cell and 200 μL of 1.1 M TFA (44 mM) was added. The cell was degassed prior to performing scans. CVs were taken at 200 mV/s without any catalyst, then in the presence of 0.2, 0.3, 0.4, and 0.5 mM catalyst from the stock solution of **6**.

Scan Rate Study

In an electrochemical cell, 1.0 mg of **6** (2.09 μmol) was dissolved in 5 mL of CH_3CN with 0.1 M TBAPF_6 and 11 mM TFA and degassed with Ar. CVs were taken at various scan rates ranging from $\nu = 5 \text{ V/s}$ to 14 V/s in order to determine the scan rate at which catalysis is no longer diffusion limited and is therefore independent of scan rate. The reaction may not be diffusion limited in order to accurately calculate turnover frequency.

Dip Test for Homogeneity

In an electrochemical cell, 0.3 mg **6** in was dissolved in 5.0 mL of CH₃CN with 0.1 M TBAPF₆ and 6.6 mM TFA. A CV was taken at a scan rate of $\nu = 200$ V/s, and afterward the glassy carbon working electrode and Pt auxiliary electrode were rinsed with CH₃CN (without polishing) and a CV was obtained in CH₃CN solution without catalyst present. The working and auxiliary electrodes were then used again to obtain CVs of **6** with 6.6 mM TFA. The electrodes were then rinsed again with acetonitrile (without polishing) and a CV was obtained in CH₃CN with 6.6 mM TFA without catalyst. In all cases no peaks were observed that would correspond to colloid formation, confirming the homogeneity of the catalyst. This study is shown in Appendix B.

Controlled Potential Coulometry

Controlled-potential coulometry experiments (CPC) were conducted in a closed 500 mL four-neck round-bottom flask. 0.3 mg of **6** (0.00063 mmol) was added to 50 mL of 0.1 M TBAPF₆ in CH₃CN. The flask was capped with two vitreous carbon electrodes and a silver wire reference electrode, all of which were submerged in solution and separated by VYCOR frits. The flask was degassed under Ar for 15 min while the solution was stirred. Using a Hamilton gas syringe, 10 mL of Ar was removed from the flask and replaced with 10 mL of CH₄ to function as an internal standard. A CV of the solution was then taken from -0.1 to -1.8 V vs. Fc⁺/Fc to identify the potential of proton reduction. A CPC was run at -1.6 V for 1800 s, while the solution continued to stir. Upon completion of the experiment, a 0.10 mL sample of gas from the flask was removed using a Hamilton gas syringe and injected into a GC. The ratio of H₂ to CH₄ in the sample was compared to a calibration curve to determine the total volume of H₂ produced during the experiment. A Faradaic yield of 98% was observed for **6**. No hydrogen was observed when the CPC experiment was run in the absence of catalyst.

Catalysis in Presence of Water

In an electrochemical cell, 0.5 mg of **6** was dissolved in 5.0 mL of 0.1 M TBAPF₆ in CH₃CN and degassed under Ar. CVs were taken at $\nu = 200$ mV/s without acid, after addition of 11 mM TFA in dry conditions, and upon addition of 100 μ L of DI water.

Background Reduction of TFA

In an electrochemical cell, 22 mM TFA in 5.0 mL of 0.1 M TBAPF₆ in CH₃CN was degassed under Ar. CVs were taken at $\nu = 200$ mV/s prior to addition of catalyst, and after addition of 0.5 mM **6**. This study may be found in Appendix B.

FeCl₃ Control

In an electrochemical cell, 0.3 mg of FeCl₃ in 5 mL 0.1 M TBAPF₆ in CH₃CN was degassed under Ar. CVs were taken at $\nu = 200$ mV/s without acid, and in the presence of 6.6 mM TFA. This study may be found in Appendix B.

Determination of Stability Using UV-Vis

A blank of CH₃CN in a sealed and degassed quartz cuvette was scanned, and then 1.0 mg of crystals of **6** were dissolved CH₃CN in a sealed quartz cuvette and degassed with Ar. A UV-Vis spectrum was taken of **6** in CH₃CN alone and then upon addition of 11 mM TFA.

Results and Discussion

Characterizing the Sulfinato Iron(III) Complex (6)

X-ray quality crystals of **6** were obtained via slow diffusion of diethyl ether into a solution of **6** in acetonitrile, yielding the product as brown block crystals. X-ray crystallography data confirmed the structure of complex **6** (Figure 3.3). The sulfinato moiety of the ligand is bound to the Fe(III) metal

center through an oxygen,

resulting in the formation of a seven-membered chelate ring.³

The complex displays a

distorted octahedral geometry

with O-Fe-N and N-Fe-Cl bond

angles of 170.22° and 161.41°,

respectively, compared to 180°

for an axial ligand angle in a

typical octahedral structure

(Table 3.1). The Fe-O bond length for the sulfinato moiety is longer than the bond length

reported for complex **2**, at 1.934 Å.³ The S-O bond lengths shown by the X-ray data are 1.527 Å

and 1.451 Å, consistent with a single S-O bond to the oxygen that is coordinated to the metal

center and a double bond between the sulfur and unbound oxygen atom. Bond lengths and

angles are shown in Table 3.1 and X-ray crystallography data may be found in Table 3.2.

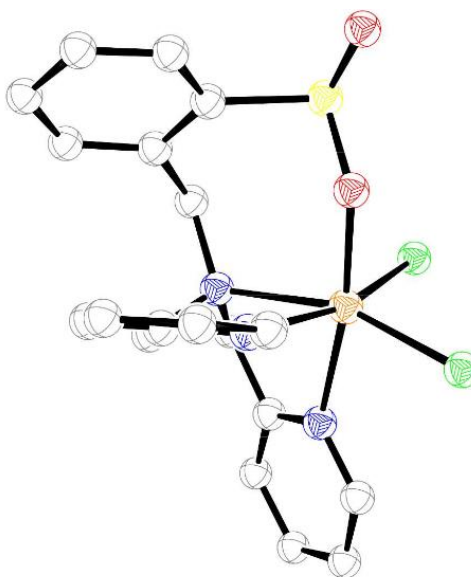


Figure 3.3. ORTEP diagram of **6**. Ellipsoids are at the 50% probability level and hydrogens have been omitted for clarity.

Table 3.1. Bond lengths [Å] and angles [°] for **6**

Fe(1)-Cl(1)	2.2720(16)
O(1)-Fe(1)-N(3)	170.22(18)
O(1)-Fe(1)-N(2)	82.63(18)
N(3)-Fe(1)-N(2)	95.55(18)
O(1)-Fe(1)-Cl(1)	96.86(12)
N(3)-Fe(1)-Cl(1)	92.83(14)
N(2)-Fe(1)-Cl(1)	93.30(13)
O(1)-Fe(1)-N(1)	96.63(18)
N(3)-Fe(1)-N(1)	73.63(19)
N(2)-Fe(1)-N(1)	75.83(18)
Cl(1)-Fe(1)-N(1)	161.41(13)
O(1)-Fe(1)-Cl(2)	91.27(13)
N(3)-Fe(1)-Cl(2)	88.13(13)
N(2)-Fe(1)-Cl(2)	165.00(14)
Cl(1)-Fe(1)-Cl(2)	101.05(7)
N(1)-Fe(1)-Cl(2)	91.37(14)
S(1)-O(1)-Fe(1)	136.5(3)
C(1)-N(1)-Fe(1)	107.7(3)
C(13)-N(1)-Fe(1)	116.8(4)
C(7)-N(1)-Fe(1)	104.2(4)
C(2)-N(2)-Fe(1)	117.3(4)
C(6)-N(2)-Fe(1)	122.0(4)
C(12)-N(3)-Fe(1)	125.4(4)
C(8)-N(3)-Fe(1)	116.6(4)

Table 3.2. X-ray Crystallography Selected Data for **6**

Empirical Formula	C ₁₉ H ₁₈ Cl ₂ FeN ₃ O ₂ S
fw (g/mol)	479.17
color/habit	dark purple needle
<i>T</i> (K)	296(2)
space group	<i>P4</i> ₃
<i>Z</i>	4
<i>a</i> (Å)	14.1819(15)
<i>b</i> (Å)	14.1819(15)
<i>c</i> (Å)	10.8160(11)
<i>α</i> (deg)	90
<i>β</i> (deg)	90
<i>γ</i> (deg)	90
<i>V</i> (Å ³)	2175.4(5)
Final R-indices (<i>I</i> > 2 <i>σ</i>)	0.0451, 0.1008
Final R-indices (all data)	0.0574, 0.1061
GOF	1.106
No. reflections measured	45127
No. of independent reflections	5212
<i>R</i> _{int}	0.0696

Assessing Kinetics and Catalytic Activity

In order to compare the electrochemical properties and activity of complex **6** to the others in this family, electrochemistry experiments similar to those reported in Chapter 2 were conducted. Catalytic activity was determined by taking the i_c/i_p ratio as described in Chapter 2. CVs of **6** in acetonitrile with TBAPF₆ as electrolyte display a reversible Fe(III)/Fe(II) redox couple at -0.28 V vs. Fc⁺/Fc. The reduction and oxidation peaks are separated by approximately 70 mV, consistent with peak separation for the Fc⁺/Fc redox couple under identical conditions.³ Ferrocene was used as an internal reference in acid addition experiments to account for drifting of the SCE electrode (Appendix B).

Acid addition studies similar to those run with **2** and **4** were conducted to test whether **6** was catalytic, and to determine the relationship between catalysis and proton concentration. Upon addition of known concentrations of 1.1 M TFA in acetonitrile, an irreversible catalytic peak appears at -1.57 V vs. Fc⁺/Fc, corresponding to a proton reduction event. With increasing additions of TFA, the catalytic peak current increases linearly, indicating a second order dependence on [H⁺] (Figure 3.4). This second order dependence is in accordance with previously reported iron polypyridyl complexes **2** and **4**.^{5,6} TFA was again selected as the proton source for comparison purposes to previously reported complexes, and because of the minimal background reduction effects in the range of potentials scanned in these experiments (Appendix B).

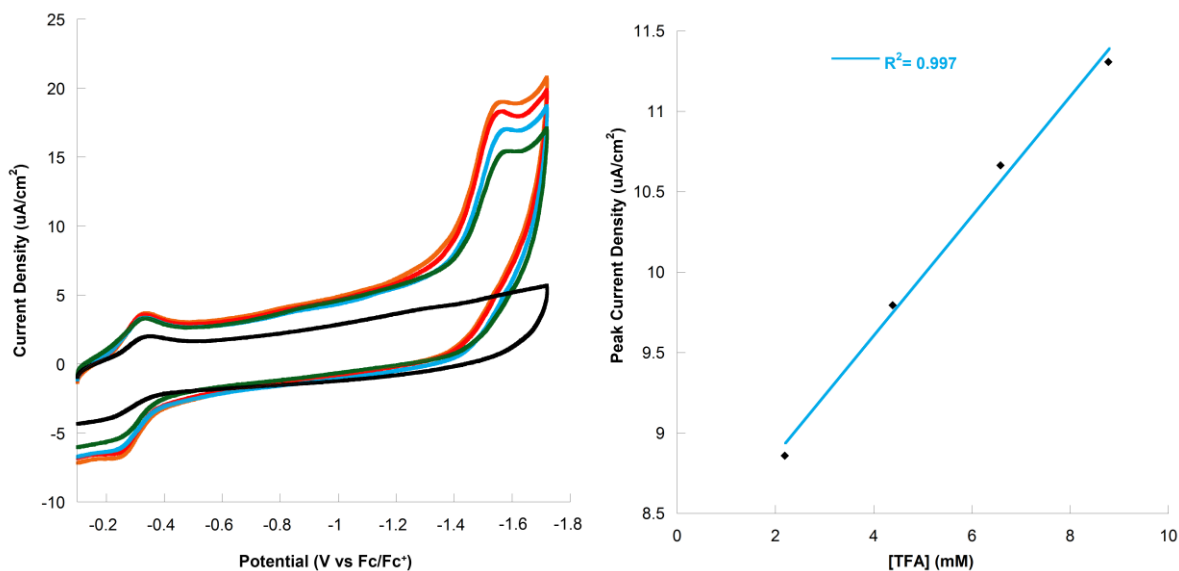


Figure 3.4. *Left:* CVs of **6** in CH₃CN with 0.1 M TBAPF₆ (black) upon addition of 2.2 mM (green), 4.4 mM (blue), 6.6 mM (red), and 8.8 mM (orange) TFA at $v = 200$ mV/s. *Right:* The peak current density vs. [TFA] was fit with a linear correlation exhibiting an R^2 value of 0.997. This suggests a second order dependence on [H⁺].

When studies were conducted holding [TFA] constant and adding known concentrations of catalyst, an irreversible catalytic wave also appears at -1.57 V vs. Fc⁺/Fc (Figure 3.5). Increasing additions of catalyst result in current enhancement and show a linear relationship between [catalyst] and peak current density. This linear relationship indicates a first-order dependence on [**6**]. The dependence on [H⁺] and [catalyst] may be combined to yield an overall rate expression for catalysis of rate = $k[\mathbf{6}][\text{H}^+]^2$.

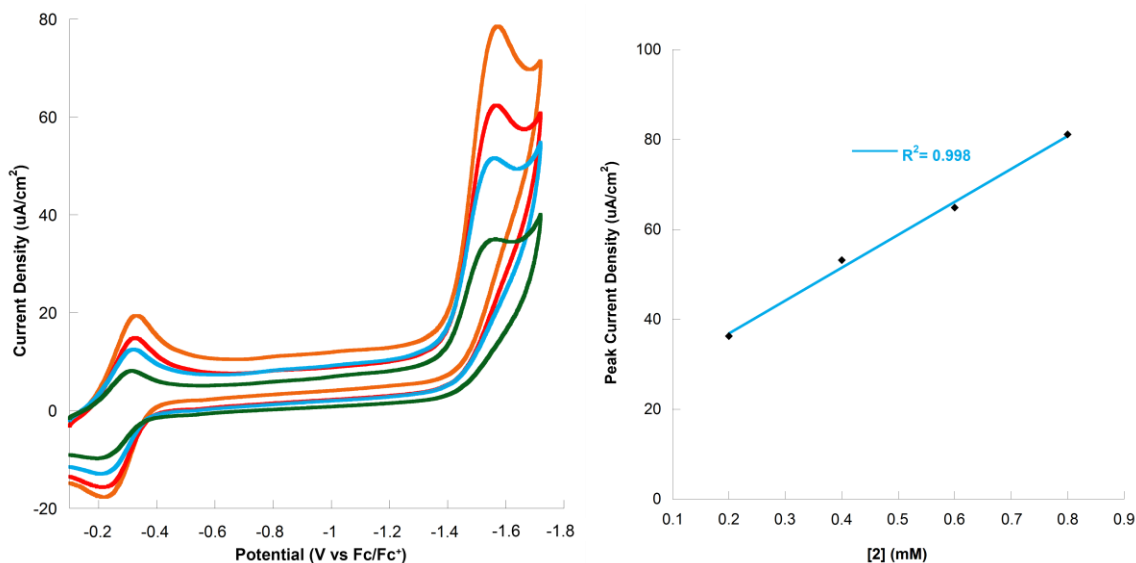


Figure 3.5. *Left:* CVs in CH₃CN with 0.1 M TBAPF₆ containing 44 mM TFA with 0.2 mM **6** (green), 0.4 mM **6** (blue), 0.6 mM **6** (red), and 0.8 mM **6** at $v = 200$ mV/s. *Right:* The peak current density vs. [**6**] was fit with a linear correlation exhibiting an R² value of 0.998. This suggests a first order dependence on [catalyst].

As discussed with complexes **2** and **4**, when the system is scan rate-independent it may be considered a pseudo-first order system and be used to determine TOF and k_{obs} . Catalysis by **6** becomes independent of scan rate at $v = 10$ V/s (Figure 3.6), yielding an i_c/i_p of 13 upon addition of aliquots of TFA (Figure 3.7). Using the method outlined in Chapter 2 to obtain TOF, this i_c/i_p value corresponds to a k_{obs} of 3300 s^{-1} (see Appendix B).⁸ This compares very favorably to complex **2**, which has an i_c/i_p of 7.8 and k_{obs} of 1000 s^{-1} under identical conditions.³ The sulfinato catalyst also compares well with previously reported iron electrocatalysts and is the only example of a sulfinato iron(III) catalyst that is active for electrochemical proton reduction.^{2, 3, 5-7}

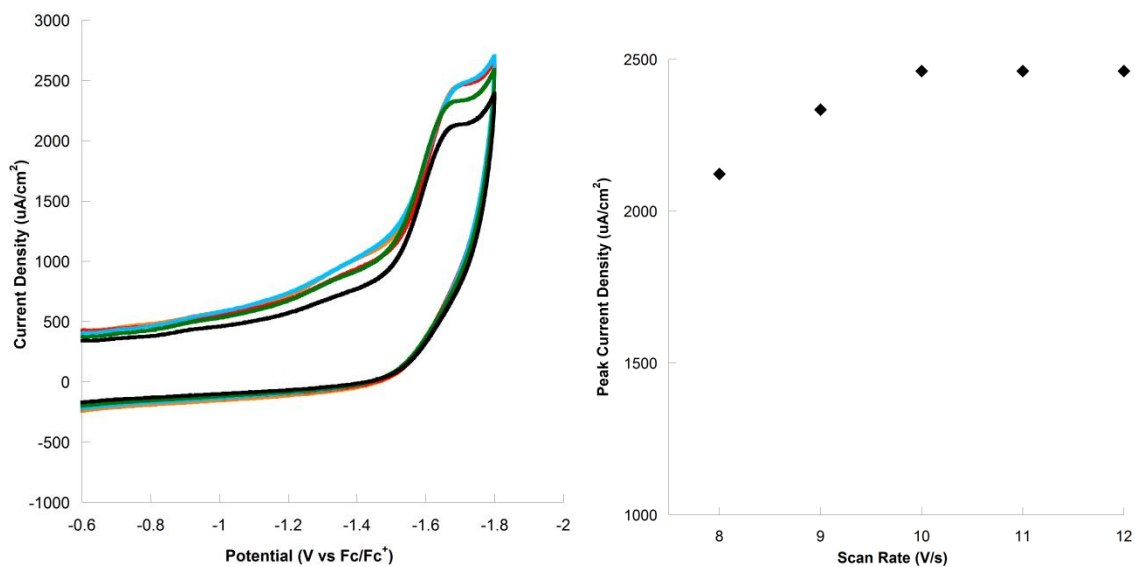


Figure 3.6. *Left:* CVs of 1.0 mg **6** in 5 mL CH₃CN with 0.1 M TBAPF₆ containing 11 mM TFA at scan rates of $\nu = 8$ V/s (black), 9 V/s (blue), 10 V/s (orange), 11 V/s (red) and 12 V/s (green).

Right: Plot of i_c vs. scan rate. The i_c of the catalytic wave at -1.6 V vs. Fc⁺/Fc becomes scan rate-independent at $\nu > 10$ V/s.

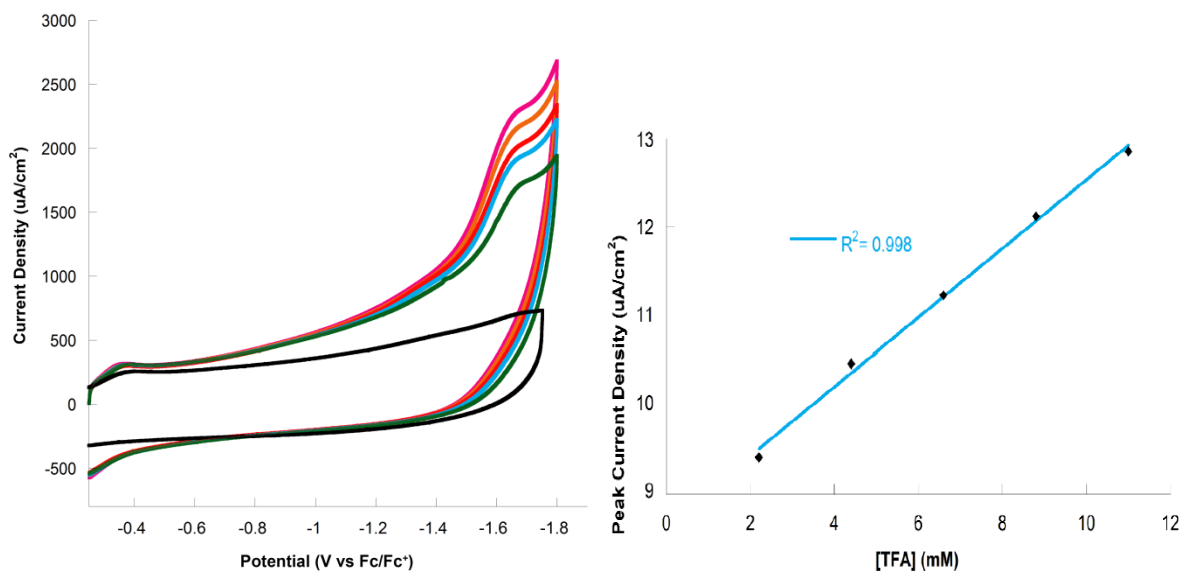


Figure 3.7. *Left:* CVs of **6** in CH₃CN with 0.1 M TBAPF₆ (black) upon addition of 2.2 mM (green), 4.4 mM (blue), 6.6 mM (red), and 8.8 mM (orange) TFA at $\nu = 10$ V/s.

Right: The peak current density vs. [TFA] was fit with a linear correlation exhibiting an R^2 value of 0.998.

The high i_c/i_p and corresponding k_{obs} illustrate the high activity of **6** for proton reduction. To the best of our knowledge, **6** is one of the most active electrocatalysts composed of a single iron center reported in the literature. The increased activity resulting from the less favorable chelate ring formed presents a model for designing more active catalysts for proton reduction.

Assessing Catalytic Efficiency

Although catalyst **6** displays unprecedented activity for a mononuclear iron complex, it is also important to evaluate the complex for its overpotential as it is common for increased catalytic activity to accompany increased thermodynamic energy input. Using the method outlined in Chapter 2 the half-wave potential of **6** was found to be -1.48 V vs. Fc^+/Fc , corresponding to an overpotential of 800 mV.^{6,9} A modest overpotential of 800 mV for **6** is comparable to previously reported electrocatalysts in organic solvents.^{3,5,7} It is of note that both complexes **2** and **6** display overpotential values of approximately 800 mV. This is significant in that the modification of the ligand to incorporate a sulfinato moiety shows a great increase in catalytic activity without simultaneously increasing the overpotential. The sulfinato complex also shows the same overpotential when using an alternative proton source, tosic acid (Appendix B).

Proposed Mechanism

In addition to its greater activity, the sulfinato complex (**6**) appears to operate under a different mechanism from the parent complex (**2**). The difference in mechanism from the phenolate complex (**2**) may be understood by comparison of acid addition experiments with **2** and **6**. Complex **2** exhibits a redox couple for Fe(III)/Fe(II) that shifts from -0.60 to -0.28 V vs. Fc^+/Fc upon addition of acid (Figure 3.8, right). This shift of the redox couple indicates a chemical change (C), or the formation of a new species; this event is likely the result of

protonation of the oxygen of the phenolate, as this is the most basic site of the complex.⁵ By comparison, the redox couple for Fe(III)/Fe(II) appears at -0.28 V vs. Fc⁺/Fc and remains stationary upon addition of TFA (Figure 3.8, left). This suggests that rather than forming a new species, the first step of the mechanism for **6** is likely an electrochemical reduction event (E). This electrochemical reduction is then followed by a chemical reaction (protonation, C) and subsequent reduction events, suggesting that catalysis proceeds through either an ECEC or ECCE mechanism (Figure 3.9).

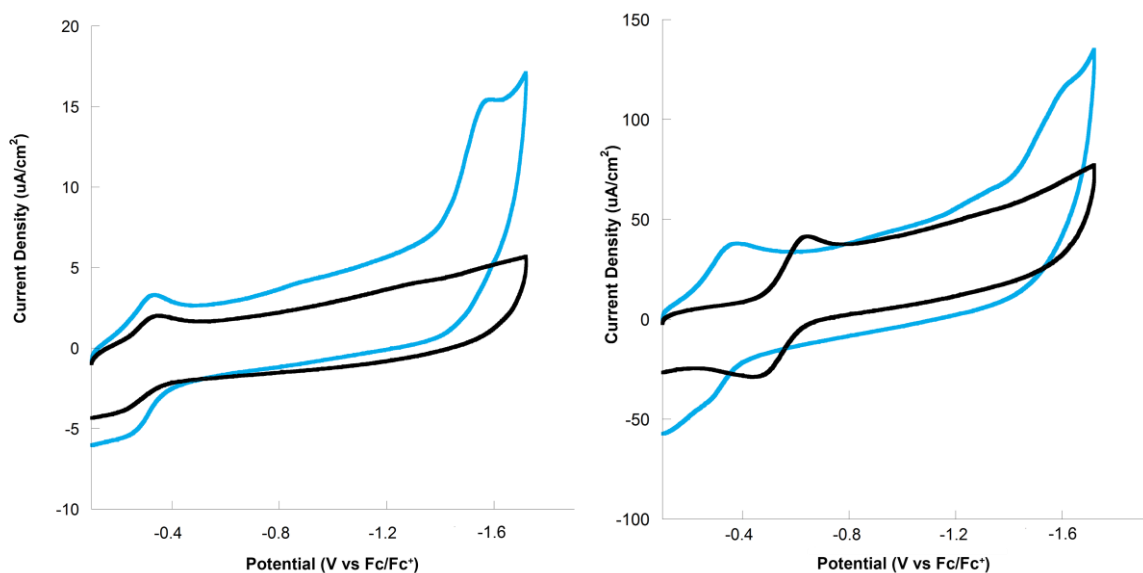


Figure 3.8. *Left:* CVs of **6** without added TFA (black) and with 8.8 mM TFA (blue). *Right:* CVs of **2** without added TFA (black) and with 8.8 mM TFA (blue).

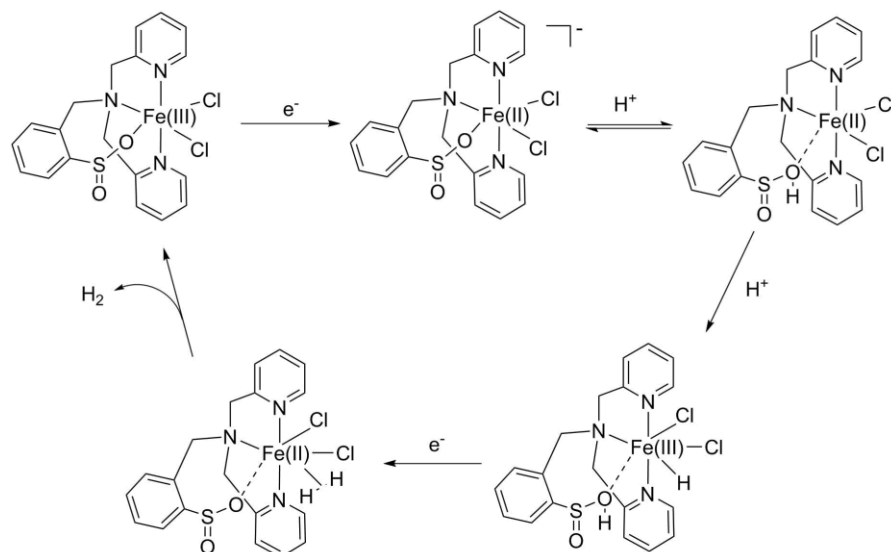


Figure 3.9. Proposed ECEC mechanism for hydrogen generation by **6**.

While the phenolate and sulfinate catalysts clearly proceed through different mechanisms, it is important to note that upon addition of acid both complexes display redox couples at the same potential (-0.28 V vs. Fc^+/Fc). This suggests that the complexes maintain the same Fe-NNN core during catalysis and that both the phenolate and sulfinate components of **2** and **6**, respectively, are hemilabile. As discussed in Chapter 2, the phenolate ligands in complexes **2** and **4** are protonated and become labile upon electrochemical reduction. Similarly, as the sulfinate moiety in complex **6** is protonated, it also becomes labile. Because complex **6** contains an unfavorable seven-membered chelate ring, the lability of the sulfinate site is increased. This increased lability results in the higher catalytic activity displayed by complex **6**. The difference in activity between **2** and **6** suggest that lability of the phenol in complex **2** is involved in the rate-determining step of the mechanism, resulting in a significant rate enhancement observed for the more labile sulfinate catalyst.³ Finally, it is also important to note that although CV is a very useful means of characterizing catalysts, it is also possible that

catalysis proceeds via a more complicated mechanism than what may be understood from electrochemistry experiments alone.

Assessing Stability

In addition to studying the kinetics, activity, and mechanism for catalysis of **6**, it is important to evaluate the catalyst for its stability and robustness. Controlled potential coulometry (CPC) was used to assess the stability of **6** during electrocatalysis and confirm the generation of H₂ gas. The potential was held at the catalytic potential of -1.6 V vs. Fc⁺/Fc for 1800 seconds to confirm that the irreversible reduction wave corresponded to a proton reduction event (Figure 3.10). Gas chromatography (GC) analysis of the headspace gases showed the evolution of 1.41 x 10⁻⁵ moles of hydrogen gas and TON of 22.4 per half-hour. This amount of hydrogen generation corresponded to an impressive Faradaic yield of 98%. It is important to note, however, that this calculated value does not accurately depict the activity of the catalyst as hydrogen is only generated by the concentration of **6** at the electrode surface.³ Additionally, differences in surface area of the vitreous carbon electrodes used in CPC experiments for each complex makes comparison difficult across laboratories and experiments.³ The inconsistency in surface areas of electrodes provides explanation for the lower amount of H₂ generated for this experiment than the CPC study of **4** (0.17 mmol) even though **6** is a significantly more active catalyst.³

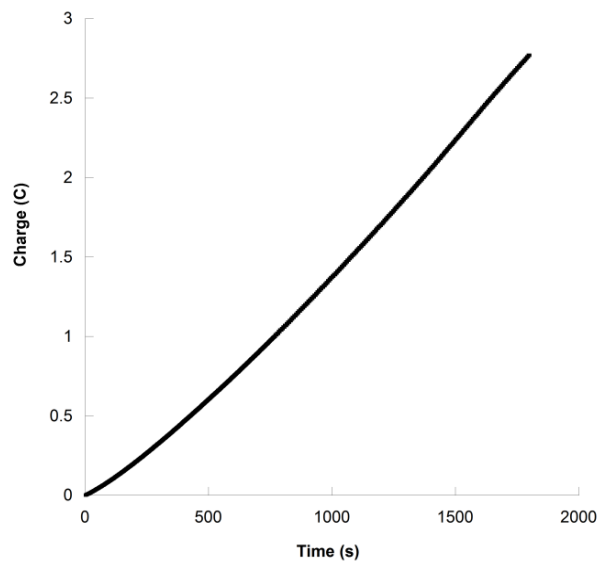


Figure 3.10. Controlled Potential Coulometry experiment with **6** in 50 mL 0.1 M TBAPF₆ in CH₃CN with 65 mM TFA. The potential was held constant at -1.6 V vs. Fc⁺/Fc for 1800 seconds.

To further confirm the stability of **6** with high concentrations of acid, a UV-Vis spectrum of **6** was taken before and after addition of 11 mM of TFA (Figure 3.11). The spectrum illustrated that the complex does not decompose or form new species even at high concentrations of acid, as the scan of **6** alone in CH₃CN was identical to the scan taken with acid added. This experiment also elucidated the charge transfer transitions of the complex. Absorption bands at 360 nm and 515 nm correspond to $p\pi \rightarrow d\sigma^*$ ligand-to-metal charge transfer (LMCT) and $p\pi \rightarrow d\pi^*$ LMCT, respectively.¹⁰ These transitions are in agreement with those reported for high-spin Fe(III) complexes bonded to polydentate ligands.

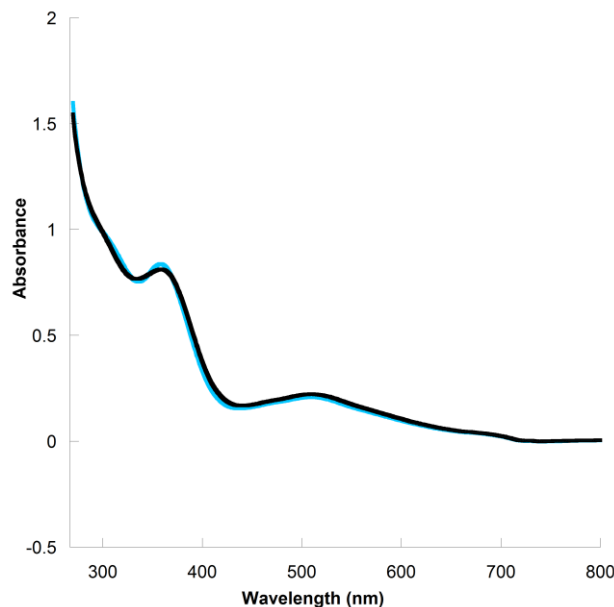


Figure 3.11. UV-Vis spectrum of **6** in CH₃CN alone (black) and upon addition of 11 mM TFA (blue).

Activity in Aqueous Mixtures

Because it is ultimately of interest to develop proton reduction catalysts that operate in aqueous systems, it was imperative to study the activity of **6** in the presence of water. CVs of **6** in acetonitrile with 11 mM TFA show that a catalytic current enhancement of 11% is achieved by addition of 100 μ L of water (Figure 3.12). This current enhancement indicates that the hemilabile sulfinate may be stabilized by polar protic solvents such as water.³

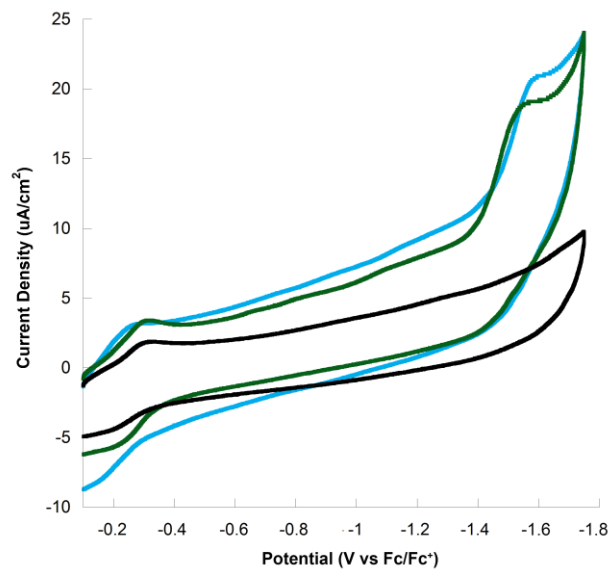


Figure 3.12. CVs of **6** in a CH_3CN solution with 0.1 M TBAPF_6 and 11 mM TFA in dry conditions (green) and upon addition of 100 μL (1.1 M) of water (blue) at $v = 200$ mV/s. The black trace represents the CV of **6** in CH_3CN with no acid added.

At higher concentrations of water, the complex is limited by solubility issues. As such, we were unable to run CVs in 1:1 $\text{CH}_3\text{CN}:\text{H}_2\text{O}$ or in purely aqueous buffer solution.³ Although the catalyst may not operate in completely aqueous solution, its enhancement in the presence of water indicates that catalysts that contain sulfinate ligands and are water-soluble may be active for proton reduction in an aqueous environment.

Conclusions

We report the first example of a sulfinato iron(III) complex that is one of the most active iron catalysts for proton reduction reported. The sulfinato ligand binds to the iron center through oxygen, resulting in a seven-member chelate ring that is likely hemilabile during catalysis.³ The sulfinato complex (**6**) reduces protons at a potential of -1.57 V vs. Fc⁺/Fc with an overpotential of 800 mV and an $i_c/i_p = 13$ ($k_{\text{obs}} = 3300 \text{ s}^{-1}$), making it significantly more active than previously reported iron polypyridyl complexes **2** and **4**. Catalysis by **6** gives an overall rate expression of $\text{rate} = k[\text{catalyst}][\text{H}^+]^2$ and is thought to proceed through either a ECEC or ECCE mechanism. The complex also exhibits enhanced catalytic activity in the presence of water, which suggests that this complex may serve as a viable example for developing catalysts for aqueous proton reduction.³ Finally, CVs of the catalyst helped elucidate a new mechanism for this family of iron polypyridyl catalysts, and helped to clarify the mechanism of previously reported complexes **2** and **4**.

References

- 1) Noveron, J.C.; Olmstead, M.M.; Mascharak, P.K. *J. Am. Chem. Soc.* **2001**, *123*, 3247-3259.
- 2) (a) McQuilken, A.C.; Jiang, Y.; Siegler, M.A.; Goldberg, D.P. *J. Am. Chem. Soc.* **2012**, *134*, 8758-8761. (b) Heinrich, L.; Li, Y.; Vaissermann, J.; Chottard, G.; Chottard, J.-C. *Angew. Chem., Int. Ed.* **1999**, *38*, 3526.
- 3) Cavell, A.C.; Hartley, C.L.; Liu, D.; Tribble, C. S.; McNamara, W. R. *Inorg. Chem.* **2015**, *54* (7), 3325-3330.
- 4) Thapper, A.; Behrens, A.; Fryxelius, J.; Johansson, M. H.; Prestopino, F.; Czaun, M.; Rehder, D.; Nordlander, E. *Dalton Trans.* **2005**, 3566-3571.
- 5) Connor, G.P.; Mayer, K.J.; Tribble, C.S.; McNamara, W.R. *Inorg. Chem.* **2014**, *53*(11), 5408-5410.
- 6) Hartley, C.L.; DiRisio, R.J.; Chang, T.Y.; Zhang, W.; McNamara, W.R. *Polyhedron* **2015**, *In press*.
- 7) Rose, M.J.; Gray, H.B.; Winkler, J.R. *J. Am. Chem. Soc.* **2012**, *134*, 8310-8313.
- 8) Hoffert, W.A.; Roberts, J.A.S.; Bullock, R.M.; Helm, M.L. *Chem. Commun.* **2013**, *49*, 7767-7769.
- 9) Fourmond, V.; Jacques, P.; Fontecave, M.; Artero, V. *Inorg. Chem.* **2010**, *49*, 10338-10347.
- 10) (a) Lanznaster, M.; Neves, A.; Bortoluzzi, A.J.; Assumpcao, A.M.C.; Vencato, I.; Machado, S.P.; Drechsel, S.M. *Inorg. Chem.* **2006**, *45*, 1005-1011. (b) Imbert, C.; Hratchian, H.P.; Lanznaster, M.; Heeg, M.J.; Hryhorczuk, L.M.; McGarvey, B.R.; Schlegel, H.B.; Verani, C.N. *Inorg. Chem.* **2005**, *44*, 7414-7422.

Appendix B

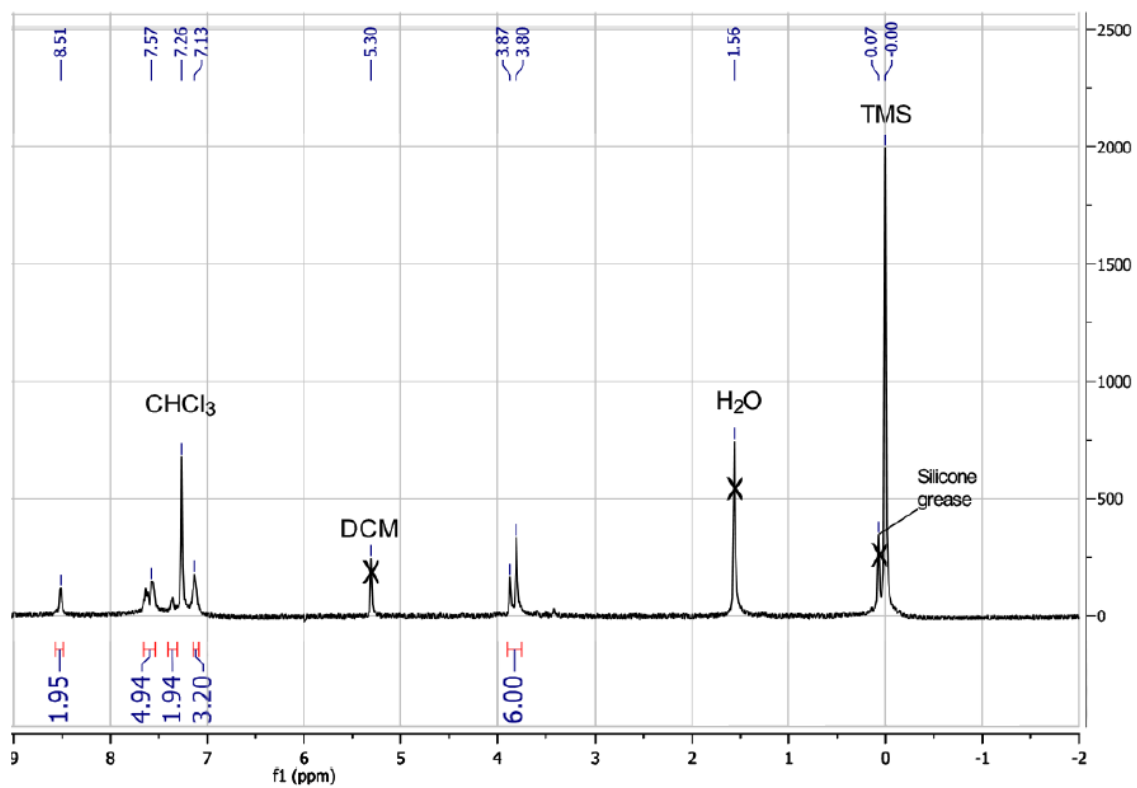


Figure B1. ^1H NMR of ligand 5.

Sample Name: WRM010
Exact Mass of (C₁₉H₁₉N₃S)H⁺ = 322.137245u
Observed Mass: 322.137527u
Difference: < -1.0 ppm

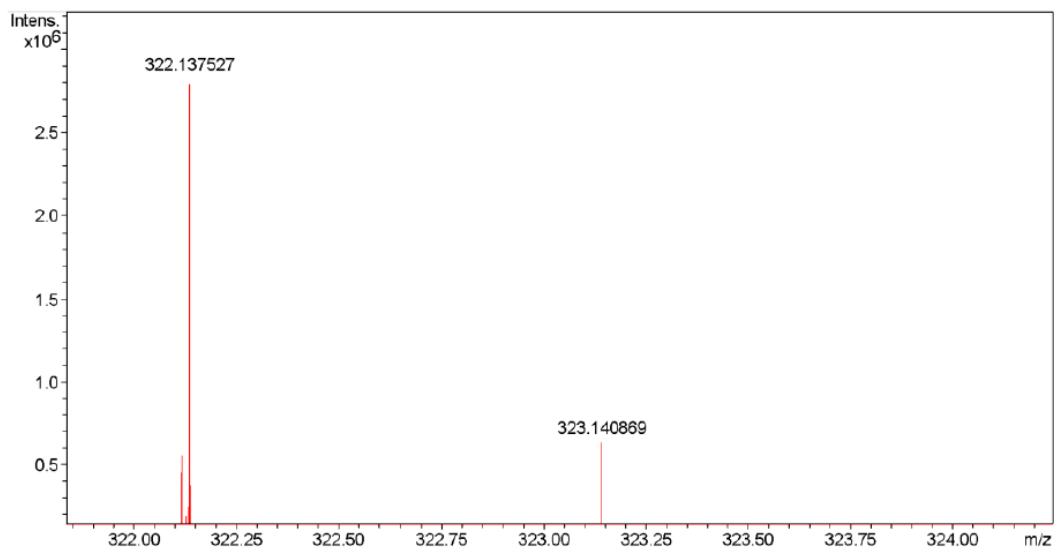


Figure B2. High-resolution mass spectrum of ligand **5** in CH₃CN.

Sample Name: WRM009
Exact Mass of (C₁₉H₁₈Cl₂FeN₃O₂S)Na⁺ = 500.973841u
Observed Mass: 500.974354u
Difference: +1.0 ppm

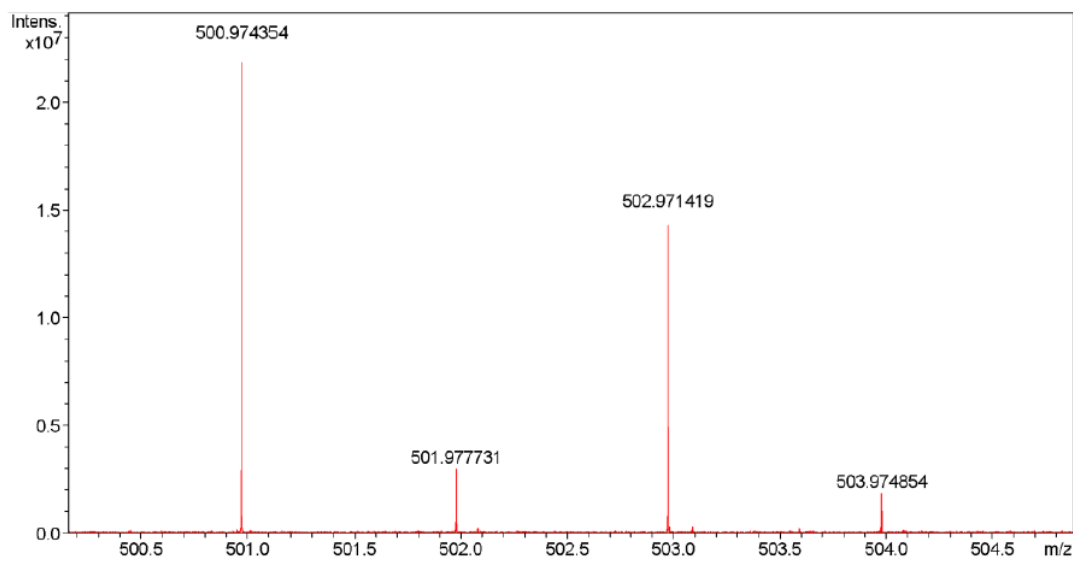


Figure B3. High-resolution mass spectrum of **6** in CH₃CN.

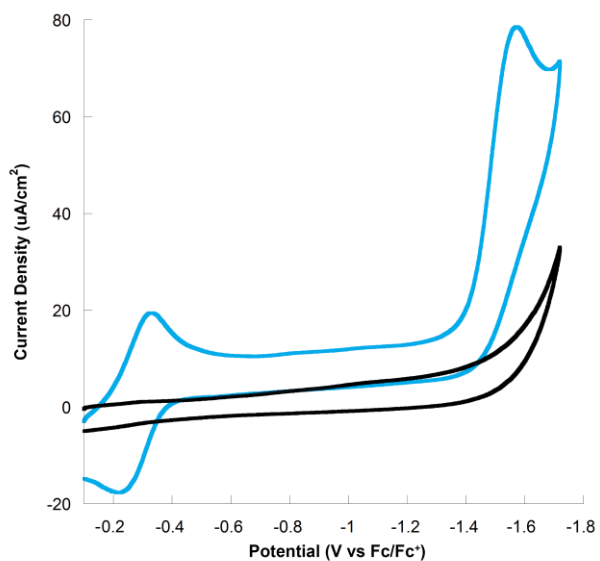


Figure B4. CVs of 22 mM TFA in 0.1 M TBAPF₆ without (black) and with 0.5 mM **6** at a scan rate of $\nu = 200$ mV/s. A catalytic reduction peak at -1.57 V vs. Fc⁺/Fc is only visible in the presence of **6**.

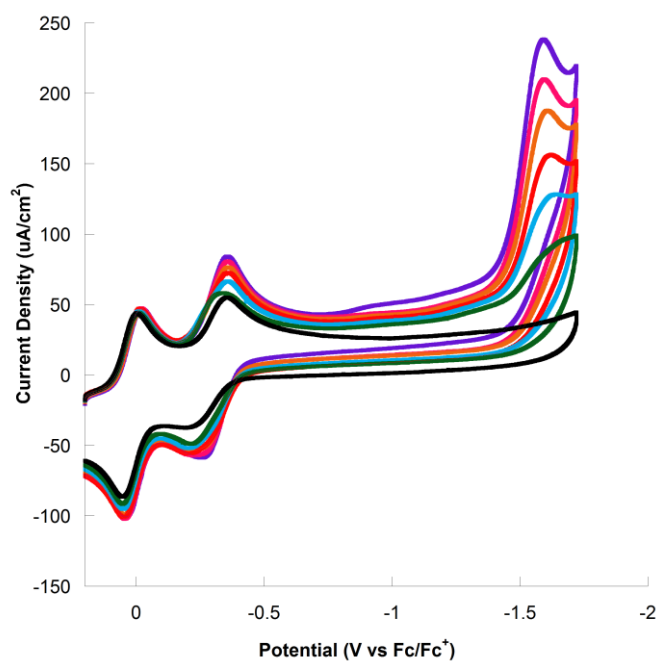


Figure B5. CVs of 0.3 mg of **6** and 0.1 mg ferrocene as an internal standard in 5 mL of 0.1 M TBAPF₆ in CH₃CN at $\nu = 200$ mV/s without acid added (black) and upon the addition of 2.2 mM (green), 4.4 mM (blue), 6.6 mM (red), 8.8 mM (orange), 11 mM (light red), and 13.2 mM (purple) TFA. The redox couple of ferrocene is observed at 0 V vs. Fc⁺/Fc.

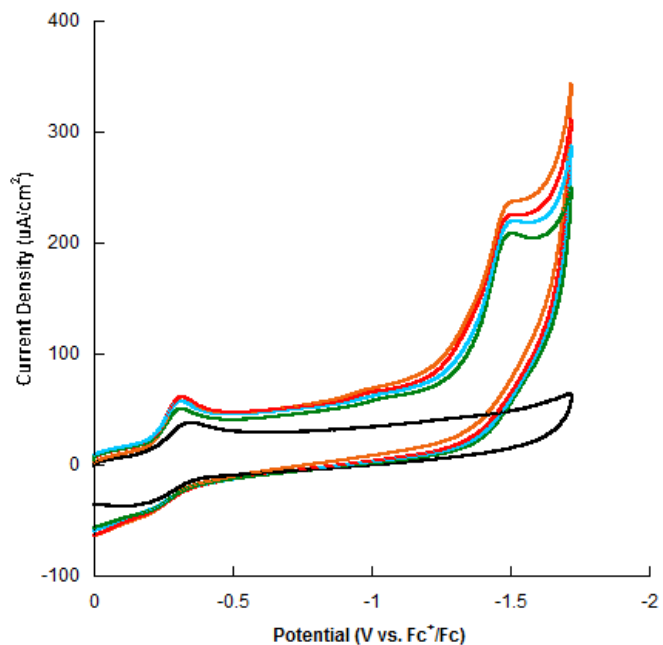


Figure B6. CVs of 0.3 mg of **6** in 5 mL of 0.1 M TBAPF₆ in CH₃CN at $v = 200$ mV/s without acid added (black) and upon the addition of 2.2 mM (green), 4.4 mM (blue), 6.6 mM (red), and 8.8 mM (orange) Tonic acid.

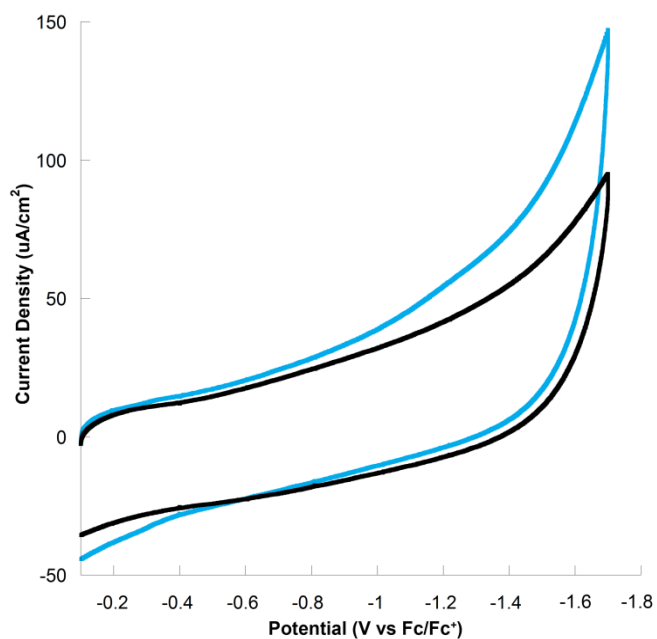


Figure B7. CVs from dip test study, showing that no peaks are observed that might correspond to colloid formation. See experimental section for description of experiment.

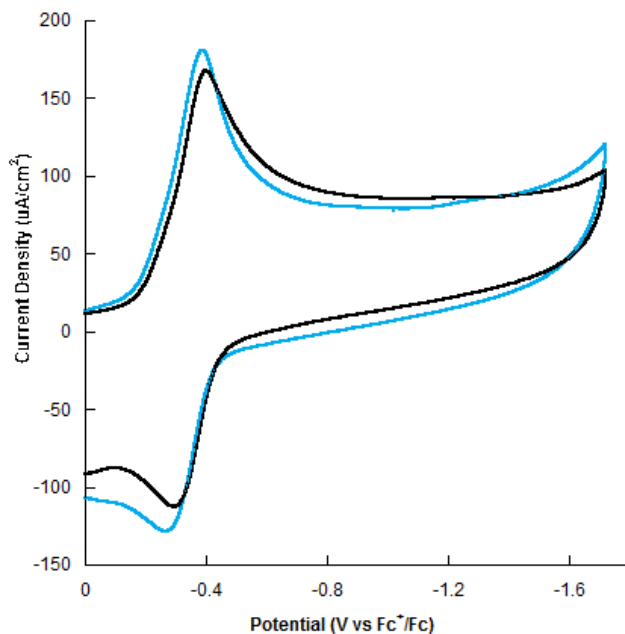


Figure B8. CVs of 0.3 mg FeCl_3 salt in 0.1 M TBAPF_6 and 5 mL acetonitrile without acid (black) and upon addition of 6.6 mM TFA (blue) at a scan rate of $\nu = 200$ mV/s. No catalytic current enhancement is observed in the presence of acid with the iron precursor salt solution.

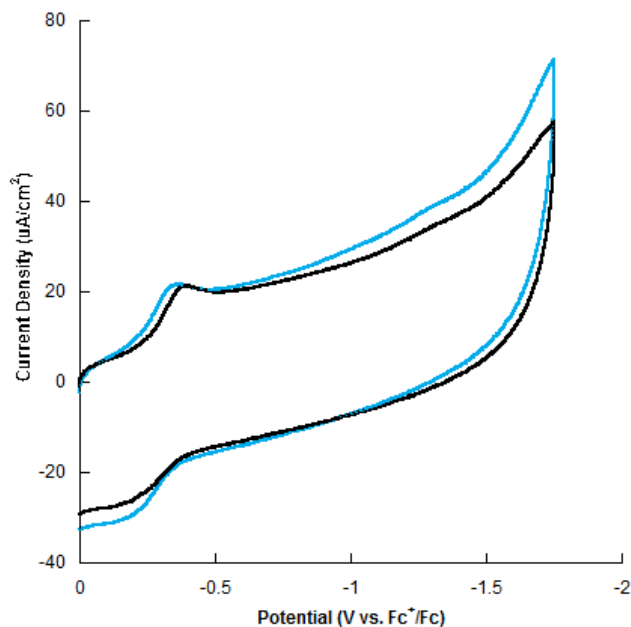


Figure B9. CVs of 0.4 mg of **6** in 0.1 M TBAPF_6 and 5 mL acetonitrile without water added (black) and upon addition of 100 μL of H_2O at a scan rate of $\nu = 200$ mV/s. The slight change in current density after addition of water was used to correct the calculation of catalytic enhancement in the presence of water.

Calculation of k_{obs} for 6 corresponding to Figure 3.7:

$$i_p = 1.223 \times 10^{-5} A$$

$$i_c = 1.557 \times 10^{-4} A$$

Correction for solvent dilution:⁸

$$i_p \times \frac{vol_i}{vol_f}$$

$$1.223 \times 10^{-5} \times \frac{5.00 \text{ mL}}{5.05 \text{ mL}} = 1.211 \times 10^{-5}$$

$$k_{obs} = \left(13 \times \frac{0.4463}{2}\right)^2 \times \left(\frac{96485 \text{ C/mol} \times 10 \text{ V/s}}{8.314 \text{ J/Kmol} \times 293 \text{ K}}\right)$$
$$= 3300 \text{ s}^{-1}$$

Chapter 4. Photochemical Systems for Hydrogen Generation

Introduction

While electrochemistry is a useful tool for studying catalytic activity and mechanism, the ultimate goal of AP is to develop systems driven by solar power.^{1,2} Systems for electrocatalysis use electrodes to provide a source of electrons; in photocatalytic systems, catalysts are instead reduced by a light-harvesting chromophore.² Though systems for photocatalysis differ from electrocatalysis in methods of reducing the catalysts, advances in light-driven AP have largely been inspired by electrocatalytic studies. Indeed, there have been numerous examples in the literature of molecular electrocatalysts that are also found to be active for proton reduction in photocatalytic systems.¹⁻⁷

An efficient means of testing catalysts for their photocatalytic activity to reduce protons to H₂ is using “three component systems” composed of a chromophore, a sacrificial electron donor, and a proton-reducing catalyst (Figure 4.1).^{1,2} In such systems, the chromophore accepts light energy upon irradiation, gets excited to PS*, and then donates an electron to the catalyst, enabling the catalyst to reduce protons in solution. The sacrificial donor then replenishes the PS and regenerates the cycle. The viability of these systems is determined by properly matching the redox potentials of the catalyst, the photosensitizer and the sacrificial donor, as well as the photocatalytic mechanism.² Key challenges limiting the large-scale development of these systems include developing cost-effective catalysts that are capable of accepting a charge and carrying out redox reactions, identifying chromophores that are capable of electron transfer at a favorable potential to drive the reaction forward, and long-term stability of the chromophore, catalyst and sacrificial donor.²

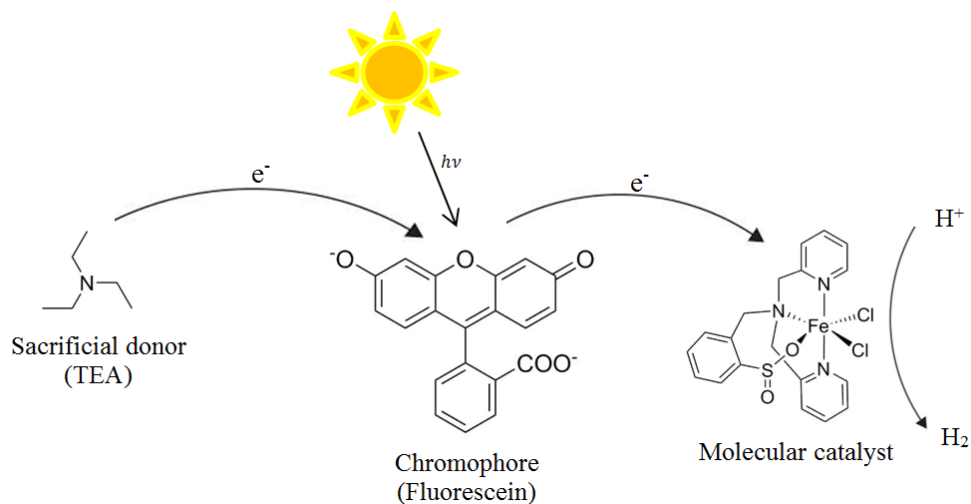


Figure 4.1. Three component system for photocatalytic hydrogen generation.

While several Ni and Co catalysts have been reported to reduce protons in photocatalytic systems, the much greater abundance of Fe on earth makes its use more desirable and cost-effective. Few to no iron catalysts have been reported that are able to photocatalytically reduce protons to hydrogen in aqueous solution. Because of the high electrocatalytic activity and stability of the iron polypyridyl complexes **2**, **4**, and **6**, it was of interest to study these complexes in photochemical systems for hydrogen generation.

The work presented in this chapter continues the investigation and comparison of the family of iron catalysts **2**, **4**, and **6** for photocatalytic hydrogen generation in systems containing the catalysts with chromophore and sacrificial donor. The systems were optimized for the best combination of chromophore and sacrificial donor with each catalyst, as well as for proton, catalyst, and chromophore concentrations. Experiments were conducted where hydrogen generation was measured over time and helped to elucidate quenching pathway of the chromophore. The goal of this research is to develop efficient and cost-effective alternatives to noble metal catalysts for photocatalytic proton reduction, and to ultimately incorporate such systems into devices for AP.

Experimental

Materials and methods

All experiments were performed under an air-free atmosphere of Ar unless otherwise indicated. Triethylamine (99.7%) and tetra-n-butyl-ammoniumhexafluorophosphate (98%), and fluorescein were purchased from Acros Organics. All other reagents were purchased from Fischer Scientific and were used without further purification.

Instrumentation

^1H and ^{13}C NMR spectra were recorded on an Agilent 400MR DD2 spectrometer operating in the pulse Fourier transform mode and chemical shifts are referenced to residual solvent. UV–Vis spectra were recorded using an Agilent Cary 60 UV–Vis Spectrophotometer using sealed quartz cuvettes degassed under Ar prior to scans. GC analysis was recorded on a Bruker Scion 436 gas chromatograph. Quenching studies were performed using a PerkinElmer LS 55 Luminescence Spectrometer. pH readings were recorded using a Vernier LabQuest2 pH sensor.

Photochemistry Experiments

Hydrogen Evolution Studies

Hydrogen evolution studies were conducted by preparing 16.0 mm x 125.0 mm glass test tubes with 20 μL of stock solution of catalyst in CH_3CN (0.4×10^{-3} M), 1.8 mL of stock solution of fluorescein in EtOH (4.0×10^{-3} M), 180 μL of EtOH, and 2.0 mL of 10% v/v TEA/ H_2O solution with a micro-stir bar, unless noted otherwise. Test tubes were sealed with airtight septa and secured with copper wire, and kept dark. The cells were degassed for 15 minutes under Ar. 1.0 mL of gas from the headspace of each test tube was then removed using a 10.0 mL Hamilton gastight syringe, and 1.0 mL of CH_4 gas was added to each cell as an internal standard. The test

tubes were inserted into a custom-built holder attached to a small motor that spins samples at 3 revolutions/min above a stir plate, and irradiated in a green LED apparatus ($\lambda = 520$ nm, $P = 1.8$ mW). LEDs of this wavelength were selected because of the broad range of chromophores that would absorb there. A fan cooled the assembly to maintain room temperature in the apparatus during the experiment. Hydrogen generation was measured using GC analysis at specified time points from the beginning of irradiation by removing a sample of 100 μ L of gas from the headspace of each test tube.

GC Calibration

Two 500 mL round bottom flasks were pulled vacuum and then filled with CH_4 and H_2 gas, one in each flask, and sealed with an airtight septa secured with copper wire. A sample was then prepared in a test tube containing a solution of 2.0 mL of CH_3CN and 2.0 mL of DI H_2O . The sample was sealed with a rubber septum, secured with copper wire, and degassed under Ar for approximately 15 minutes. A 10.0 mL Hamilton gastight syringe was then used to remove 1.0 mL of headspace gas from the test tube and 1.0 mL of CH_4 was added as an internal standard. Varied amounts of H_2 gas, ranging from 10 μ L to 500 μ L, were then added to the test tube. Gas samples of 100 μ L each were injected into a GC to determine the ratio of peak areas of H_2 to CH_4 . The peak area ratios were then plotted versus the volume of H_2 . The slope of the linear trend of the data was used to calculate the volume of H_2 generated from hydrogen evolution studies (Figure 4.2).³

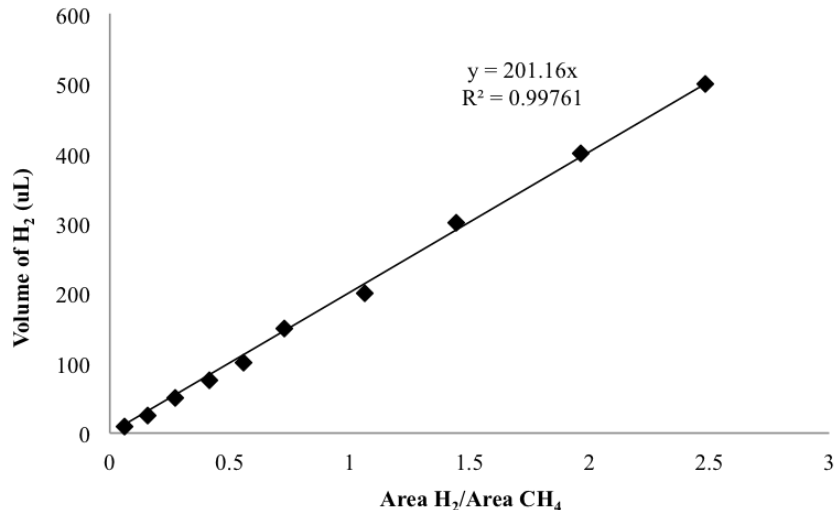


Figure 4.2. Calibration curve of H₂ to CH₄ peak areas used for determination of hydrogen generation. The ratio of peak areas was plotted against the volume of H₂ injected into the GC.³

Comparison of Chromophores and Sacrificial Donors

Hydrogen generation studies were also conducted using several commonly employed chromophore and sacrificial donor pairings in addition to fluorescein and triethylamine. Chromophore stock solution of tris(2,2'-bipyridyl)ruthenium(II) chloride in CH₃CN (1.56 x 10⁻³ M) was prepared and a corresponding sacrificial donor solution of ascorbic acid was prepared by dissolving 0.881 g of ascorbic acid in 25 mL DI H₂O. The ascorbic acid solution was then adjusted to pH = 4 by adding NaOH dropwise. Samples of hydrogen evolution studies were then prepared using 1.28 mL of Ru(bpy)₃²⁺, 50 μL of catalyst, and 670 μL of CH₃CN. 2.0 mL of ascorbic acid solution was then added to each sample, and the samples were degassed for 15 min. They were then prepared according to the same procedure described for the hydrogen generation studies. Similarly, chromophore stock solution of eosin Y in EtOH (4.0 x 10⁻³ M) was prepared along with a corresponding sacrificial donor of 10% v/v TEA/H₂O or 10% v/v triethanolamine

(TEOA)/H₂O solution. The TEOA solution was adjusted to pH = 7 by adding conc. HCl dropwise. Samples were prepared using 1.8 mL of Eosin Y stock solution, 20 μL of stock solution of catalyst in CH₃CN (0.4 x 10⁻³ M), 180 μL of EtOH, and 2.0 mL of 10% v/v TEA/H₂O or TEOA/H₂O solution. Samples were again degassed for 15 min and then prepared according to the procedure outlined in the hydrogen generation studies.

Hydrogen Evolution Using Local Pond Water

Water samples were collected from four locations around two bodies of water on the College of William and Mary campus. Samples were collected in 60 mL jars and kept sealed until use. Prior to using the water in experiments, samples were allowed to warm to room temperature. Water samples were filtered once by gravity filtration prior to use to remove any dirt or particles. Test tube samples were then prepared identically to that described above for hydrogen generation studies.

Photochemical Quenching

Catalyst Quenching (Oxidative)

Stock solutions of fluorescein in EtOH (4.0 x 10⁻³ M) and catalyst (**2**, **4**, **6**) in CH₃CN (8.0 x 10⁻⁴ M) were prepared. 7.5 μL of fluorescein stock solution was diluted with 3.0 mL of a solution of 1:1 EtOH:H₂O at pH = 12.5 in an air-free cuvette. The fluorescein solution was wrapped in aluminum foil to keep dark throughout the experiment. Both the fluorescein and catalyst solutions were degassed under Ar for 15 minutes, after which a positive pressure of Ar was maintained in the samples using an Ar balloon throughout the experiment. The catalyst solution was added to the cuvette in 10 μL increments, and the fluorescence intensity was monitored by exciting the sample at 430 nm. A total of 80 μL of catalyst solution was added in each

experiment unless noted otherwise. Stern-Volmer plots were used to calculate the quenching coefficient of each catalyst.

Sacrificial Donor Quenching (Reductive)

The triethylamine (TEA) quenching experiment was conducted using a similar procedure as outlined above. The stock solution of fluorescein was prepared using the same method, wrapped in aluminum foil and degassed for 15 minutes under Ar. Pure TEA was also degassed with Ar for 15 minutes. To observe fluorescence quenching by sacrificial donor, the TEA was added to the air-free cuvette in 30 μL increments and fluorescence intensity was recorded by exciting the sample at 430 nm. A total of 300 μL of TEA was added. A Stern-Volmer plot was used to calculate the quenching coefficient of TEA.

Quantum Yield Studies

A sample containing catalyst, fluorescein, and TEA at optimal conditions was prepared as outlined for the hydrogen generation studies. Quantum Yield measurements (QY) were performed by taking the difference between the power of light (P) emitted from the LEDs and the power of light passing through the sample. Measurements were taken immediately upon preparing the sample and after 24 hours, using a Coherent Fieldmate Laser Power Meter. 100 μL of headspace gas from the sample was removed and analyzed by GC. The quantum yield (ϕ_{H_2}) was determined by the following calculation, where λ is 520 nm, P is power (in W), h is Planck's constant, c is the speed of light, n is the number of photons, t is time (in seconds), k is the average rate of hydrogen production, and q_p is photon flux:⁴

$$P = \frac{c \times h \times n}{\lambda \times t} \quad (4.1)$$

$$k = \frac{n}{t(s)} \quad (4.2)$$

$$q_p = \frac{P \times \lambda}{c \times h} \quad (4.3)$$

$$\phi_{H_2} = \frac{2k}{q_p} \quad (4.4)$$

The QY reported was averaged from multiple measurements to account for differences in instrument readings and sample preparation. Sample calculations are included in the text.

Results and Discussion

Photochemical System for Hydrogen Generation

The systems for photochemical hydrogen generation included a chromophore, catalyst, and sacrificial donor in solution. Several commonly used chromophore and sacrificial donor pairings that operate well with catalysts of similar reduction potentials to **2**, **4**, and **6** were tested in our systems. Each of the catalysts were studied with fluorescein (Fl), eosin Y (EY), and tris(2,2'-bipyridyl)ruthenium(II) chloride ($\text{Ru}(\text{bpy})_3^{2+}$) (Figure 4.3). Fl is of interest because it is a highly reducing and inexpensive organic dye. EY is a halogenated derivative of Fl, and the bromide substituents enable the chromophore to undergo intersystem crossing to produce a longer lived excited triplet state.^{2,3} $\text{Ru}(\text{bpy})_3^{2+}$ is generally considered the most stable of the three chromophores as it is less susceptible to photobleaching than the organic dyes. Additionally, $\text{Ru}(\text{bpy})_3^{2+}$ has long lived fluorescence lifetimes but is limited by its higher cost.³

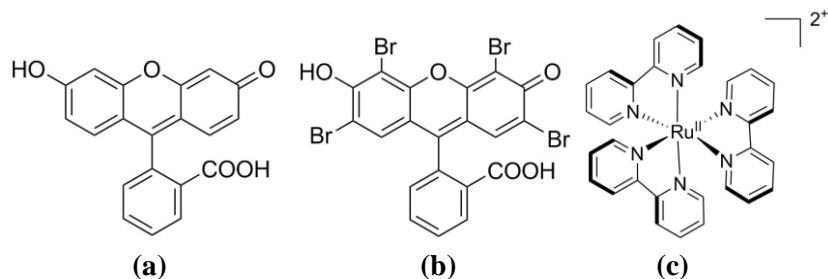


Figure 4.3. Commonly used chromophores (a) Fluorescein; (b) Eosin Y; (c) $\text{Ru}(\text{bpy})_3^{2+}$.

Of these chromophores, Fl yielded the highest activity with catalysts **2**, **4**, and **6** (see corresponding data in Appendix C). The greater activity of the systems with Fl compared to EY and $\text{Ru}(\text{bpy})_3^{2+}$ may be attributed to it being much more thermodynamically favorable for Fl to reduce the catalysts. The donating chromophores differ in reduction potential energies, with Fl corresponding to a reduction potential of -1.70 V vs. Fc^+/Fc , while EY^- has a lower reduction potential of -1.46 V vs. Fc^+/Fc . $\text{Ru}(\text{bpy})_3^{3+}$ is the least reducing of the three chromophores, with

a reduction potential of -1.21 V vs. Fc^+/Fc .^{2b, c} Compared with the redox potential of the protonated catalysts at -0.28 V vs. Fc^+/Fc , the larger thermodynamic difference makes photoreduction of the catalyst by Fl^- the most favorable (Figure 4.4). It is important to note that while Figure 4.4 is useful in understanding the favorability of Fl^- compared to the other chromophores, it is limited by its assumption that the photochemical systems undergo the same mechanism as determined by electrochemical studies. Because the photochemistry experiments were conducted at a much more basic pH than the electrochemistry experiments, the catalyst is likely reduced prior to protonation and may undergo a different mechanism than those proposed earlier. The estimate of the reduction potential for the protonated form of the catalyst at -0.28 V vs. Fc^+/Fc may therefore also be inaccurate at photochemical conditions.

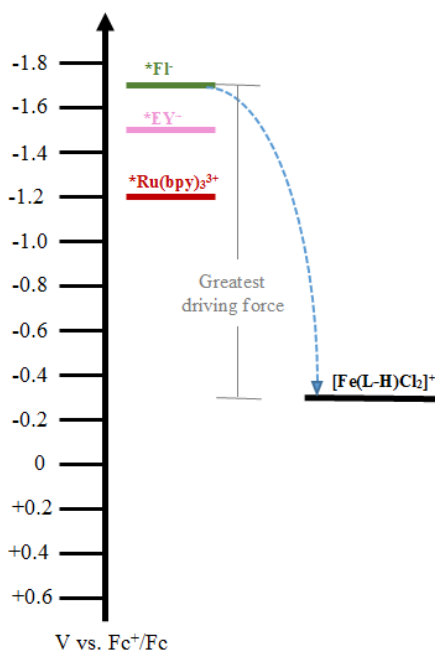


Figure 4.4. Schematic showing the larger thermodynamic driving force for reduction of the protonated catalyst by $^*\text{Fl}^-$ as compared to $^*\text{EY}^-$ and $^*\text{Ru}(\text{bpy})_3^{3+}$.

In addition to working the best with our catalysts, Fl is of interest in photochemical systems because it is a strong chromophore with an accessible π^* excited state and is relatively

inexpensive.² TEA was selected as the sacrificial donor in our systems as it is commonly paired in systems that utilize Fl as the chromophore.² Additionally, TEA is economical and its decomposition in solution is not known to produce reactive byproducts.²

Optimizing System Conditions for Hydrogen Generation

It was necessary to first establish optimal conditions for hydrogen generation for **2**, **4**, and **6**. The systems were each adjusted to determine the optimal catalyst, chromophore, and proton concentrations (pH). Experiments were first conducted varying the concentration of catalyst **2** while holding [Fl] constant, and then varying the concentration of Fl while holding [**2**] constant. Photocatalytic activity is compared in terms of the turnover number (TON), which is a measure of the moles of hydrogen produced per mole of catalyst used. Comparison of activity in terms of TON rather than volume of H₂ generated is necessary as it normalizes the volume of hydrogen generated among experiments varying [catalyst].³ Catalyst concentration studies showed optimal conditions at 2 μM of **2** with 1.8 mM Fl and 5% v/v TEA/H₂O (Table 4.1, Figure 4.5).

Table 4.1. Photocatalytic H₂ generation systems with 1.8 x 10⁻³ M Fl, 5% v/v TEA/H₂O and varying concentration of **2** in 1:1 H₂O:EtOH after 12 hours of irradiation.

[Fluorescein] (M)	[Catalyst] (M)	H ₂ (μL)	TON
1.8 x 10 ⁻³	0.50 x 10 ⁻⁶	21.8	490
1.8 x 10 ⁻³	1.00 x 10 ⁻⁶	61.5	690
1.8 x 10 ⁻³	2.00 x 10 ⁻⁶	151	840
1.8 x 10 ⁻³	3.00 x 10 ⁻⁶	185	690
1.8 x 10 ⁻³	4.00 x 10 ⁻⁶	215	620

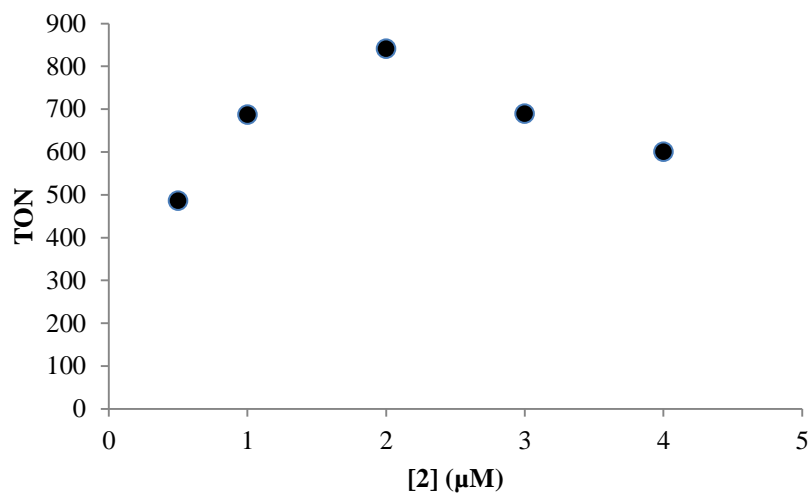


Figure 4.5. TON vs. [2] with 1.8 mM of Fl and 5% TEA in 1:1 H₂O:EtOH solution after 12 hours of irradiation.

Experiments varying the amount of chromophore in the systems generally showed increasing TON at higher concentrations of Fl, with optimal conditions at 1.9 mM Fl with catalyst **2** (Table 4.2, Figure 4.6).

Table 4.2. Photocatalytic H₂ generation systems with 2.0 x 10⁻⁶ M **2**, 5% v/v TEA/H₂O and varying concentration of Fl in 1:1 H₂O:EtOH after 12 hours of irradiation.

[Fluorescein] (M)	[Catalyst] (M)	H ₂ (μL)	TON
1.6 x 10 ⁻³	2.00 x 10 ⁻⁶	121	680
1.7 x 10 ⁻³	2.00 x 10 ⁻⁶	140	780
1.8 x 10 ⁻³	2.00 x 10 ⁻⁶	151	840
1.9 x 10 ⁻³	2.00 x 10 ⁻⁶	203	1132
2.0 x 10 ⁻³	2.00 x 10 ⁻⁶	162	900
2.1 x 10 ⁻³	2.00 x 10 ⁻⁶	135	753

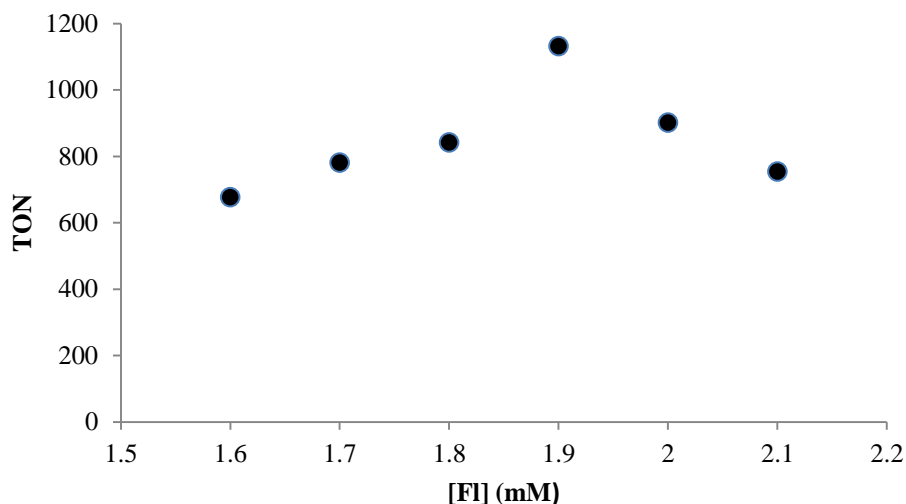


Figure 4.6. TON vs. [Fl] with 2 μM of **2** and 5% TEA in 1:1 H_2O :EtOH solution after 12 hours of irradiation.

The results of the optimization experiments clearly illustrate that catalyst **2** operates at optimal conditions of 2 μM catalyst and 1.9 mM Fl with 5% v/v TEA/ H_2O (Figures 4.5 and 4.6, respectively). Optimization studies with the nitro-functionalized catalyst (**4**) and the sulfinato catalyst (**6**) showed highest performance at similar conditions. Both **4** and **6** yield highest TON at conditions of 2 μM catalyst and 1.8 mM Fl (Appendix C). The experiments generated similar results to those reported in the literature for other three component systems with transition metal catalysts.^{2,5-7} Studies by McNamara *et al.*, for example, report photocatalytic systems with cobalt-dithiolene complexes yielding highest activity at very low concentrations of catalyst (<0.1 mM).^{2,7} As illustrated in Table 4.2, increasing [2] increases the overall amount of hydrogen generated; however, at higher concentrations of catalyst the rate of hydrogen evolution does not continue to increase.^{2,7} Higher concentrations of chromophore, on the other hand, generally leads to less rapid bleaching of samples.⁷

Studies varying pH demonstrated that the system yields the highest TON at pH 12.5 with **2** (Figure 4.7), as well as for systems with **4** and **6** (Appendix C). Many previously reported photocatalytic systems for proton reduction also operate with the highest rate at very basic pH in the range of 12-13.^{5,6} Lazarides *et al.*, reasoned that hydrogen generation is optimized at higher pH as protonation of TEA in solution results in a less effective electron donor at more acidic conditions.⁶ At pH above 12.5, the subsequent decrease in activity of the system is likely attributed to the lower $[H^+]$ in solution.^{2,7}

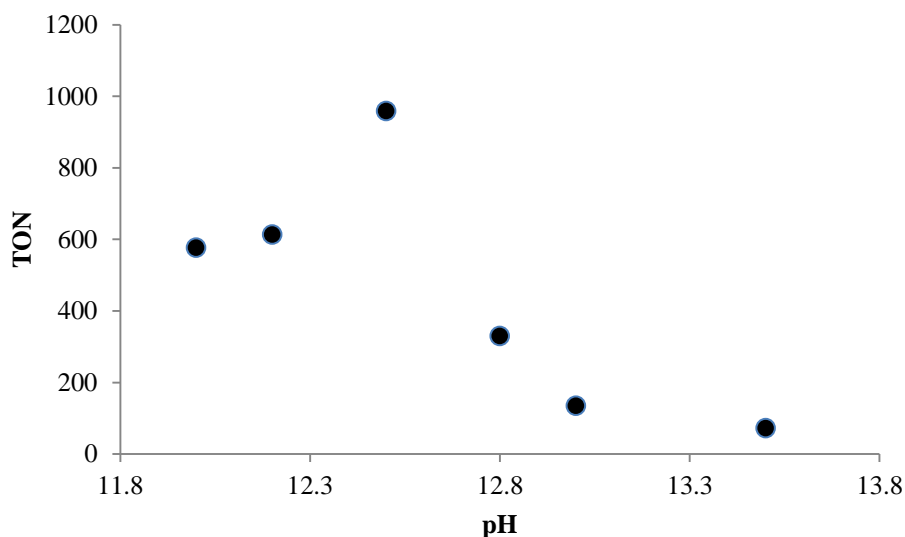


Figure 4.7. TON vs. pH with 2 μ M of **2**, 1.9 mM FI and 5% TEA in 1:1 H₂O:EtOH solution after 12 hours of irradiation.

Once optimal conditions were established, hydrogen generation experiments were conducted with each catalyst. Hydrogen generation was measured over a 24 hour period, with samples of the headspace gases taken after 1, 3, 6, 12, and 24 hours to observe the rate of evolution. Sample data is presented in Figure 4.8 for complex **2** at its optimal conditions, showing the generation of hydrogen over the 24 hour period. At optimal conditions, the activity of each catalyst may be compared. The parent catalyst **2** shows the highest activity of the three

catalysts, achieving over 2100 TON in 24 hours, while catalyst **4** yields over 1030 TON and catalyst **6** operates at the lowest level of activity, producing 740 TON in the same time period (Figure 4.9). The catalysts generally follow the trend proposed from electrochemistry studies with catalyst **2** performing at a faster rate than **4**. The lower activity of **6**, however, was unexpected based on the higher i_c/i_p and TOF determined with CV data. In addition to its lower activity, the data from **6** shows a slowing in activity after the 3 hour data point. As opposed to **2** and **4**, complex **6** begins at a similar rate of evolution to the other catalysts and then plateaus in activity. This indicates that **6** may be decomposing more rapidly in these systems than **2** or **4**.

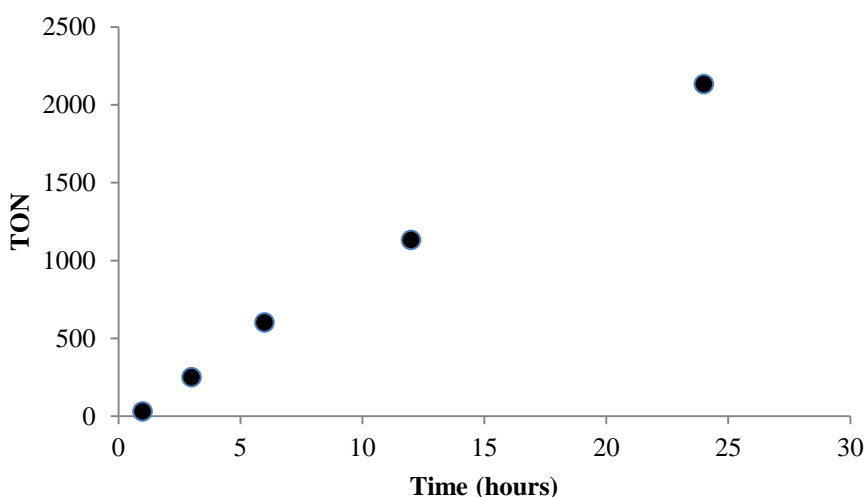


Figure 4.8. Hydrogen evolution over 24 hour period in photochemical system with **2** at optimal conditions (1.9 mM FI, 2 μ M catalyst with 5% v/v TEA/H₂O at pH 12.5).

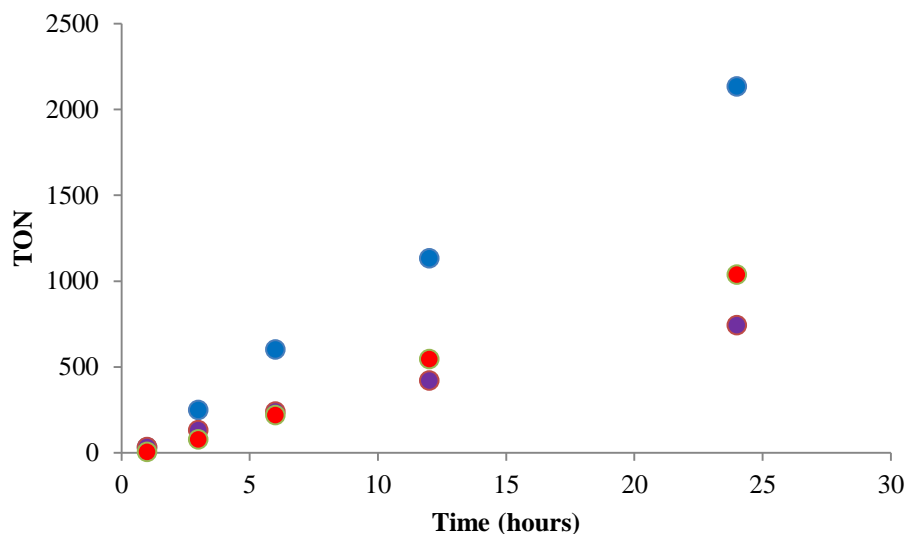


Figure 4.9. Hydrogen evolution over 24 hour period in photochemical systems comparing **2** (blue), **4** (red), and **6** (purple) at their optimal conditions.

Hydrogen Evolution Using Local Pond Water

The ultimate goal of developing systems for AP would enable people living in less industrialized regions to collect water from nearby bodies of water and use these devices to generate hydrogen fuel. It was therefore important to study whether these systems are able to reduce protons from water collected outdoors. To do so, water collected from Lake Matoaka in Williamsburg, Virginia was used as the water source in several trials.

Experiments using this water source successfully generated over 180 μL of hydrogen over a period of 24 hours, corresponding to over 1000 TONs (Figure 4.10). These studies operated at approximately half the rate of hydrogen generation as typical photochemical experiments conducted using DI water. The lower activity of the studies performed using the water from Lake Matoaka may be attributed to the presence of unknown pollutants, bacteria, or chelating humic acids. Additionally, the pH of the samples using the outdoor water rests at a slightly more acidic pH of 12.2 compared to the optimal pH of 12.5 for these systems. As it was

earlier determined that the activity of each of the catalysts decrease at pH below 12.5, this may be a contributing factor to the lower activity.

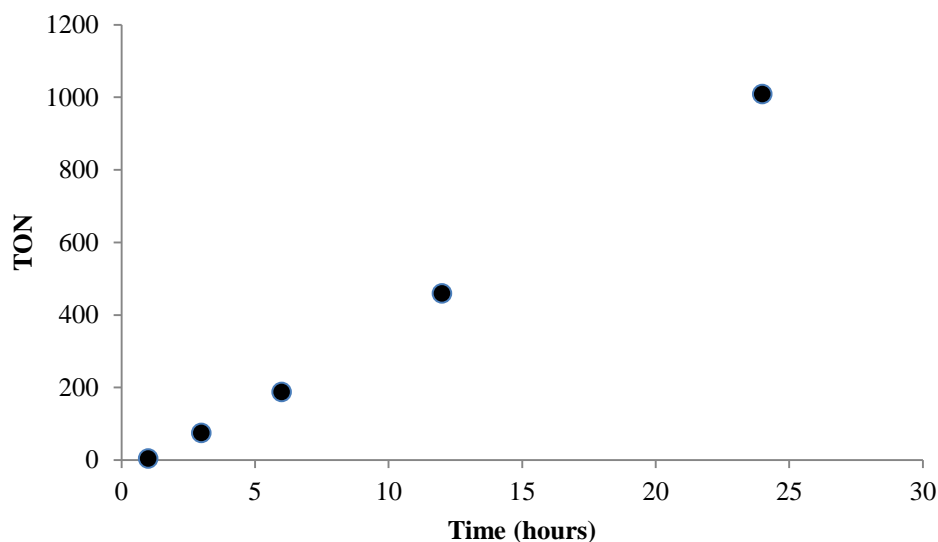


Figure 4.10. Hydrogen evolution over 24 hour period in photochemical systems comparing with 2 μM of **2**, 1.9 mM FI, and 5% v/v TEA/ H_2O solution using water from Lake Matoaka.

While lower in activity, experiments conducted with the water from the lake still performed better than many other reported systems for photocatalytic hydrogen generation.^{2,6} The results indicate that overall AP devices using systems modelled after those reported here may be viable options for hydrogen evolution purposes. Importantly, the cost-effective nature of the organic chromophore, inexpensive sacrificial donor, and iron catalysts used in these experiments assure that such devices for AP may be effective for widespread use.

Gaining Mechanistic Insight: Quenching Studies

It was of interest to further study the photocatalytic mechanism of our system in order to investigate the disparities in activity between each of the catalysts. Fluorescence quenching experiments allow for more in depth studies of the photocatalytic mechanism, especially in

regards to the chromophore. In our photochemical systems, Fl may undergo two distinct pathways to transfer electrons to the catalyst: reductive or oxidative quenching pathways (Figure 4.11).^{2g} The dominating pathway is determined by experimental conditions. Fl is more likely to undergo a reductive quenching pathway at high concentrations of TEA. In a reductive quenching pathway, Fl is first excited upon irradiation of light to $^1\text{Fl}^*$ and then reduced to $^*\text{Fl}^-$ by an electron transfer from TEA. This $^*\text{Fl}^-$ species may then donate an electron to the catalyst, allowing for proton reduction by the catalyst and regenerating Fl in its ground state. $^*\text{Fl}^-$ is unstable and decomposes easily in solution, and as such leads to shorter lifetimes for hydrogen generation. Conversely, $^1\text{Fl}^*$ may undergo an oxidative quenching pathway at low concentrations of TEA. In an oxidative quenching pathway, $^1\text{Fl}^*$ first transfers an electron to the catalyst, generating the more stable $^*\text{Fl}^+$ cation. This $^*\text{Fl}^+$ species is then reduced by TEA to reform Fl. The reductive quenching pathway is dominant when TEA quenches fluorescence at a faster rate than the catalyst, and the oxidative pathway is dominant when the catalyst operates with a faster quenching rate.

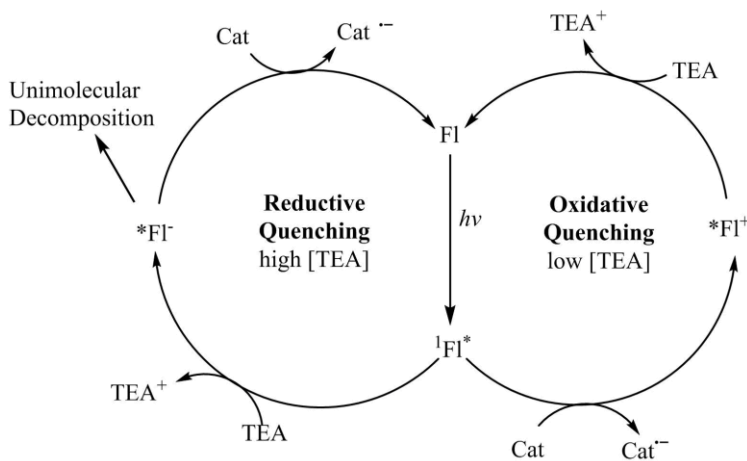


Figure 4.11. Possible quenching mechanisms that Fl may undergo in our systems include reductive quenching (left) and oxidative quenching (right).^{2g}

Fluorescence quenching experiments of Fl* were conducted in 1:1 H₂O:EtOH at pH 12.5 to be comparable to experimental conditions. Fl* quenching by TEA shows dynamic quenching. The corresponding Stern-Volmer plot allowed for determination of a quenching constant by TEA of $2.29 \times 10^8 \text{ M}^{-1}\text{s}^{-1}$ (Figure 4.12). Taking into account the experimental [TEA] of 0.36 M, the quenching rate in our studies for TEA is therefore $8.24 \times 10^7 \text{ s}^{-1}$.

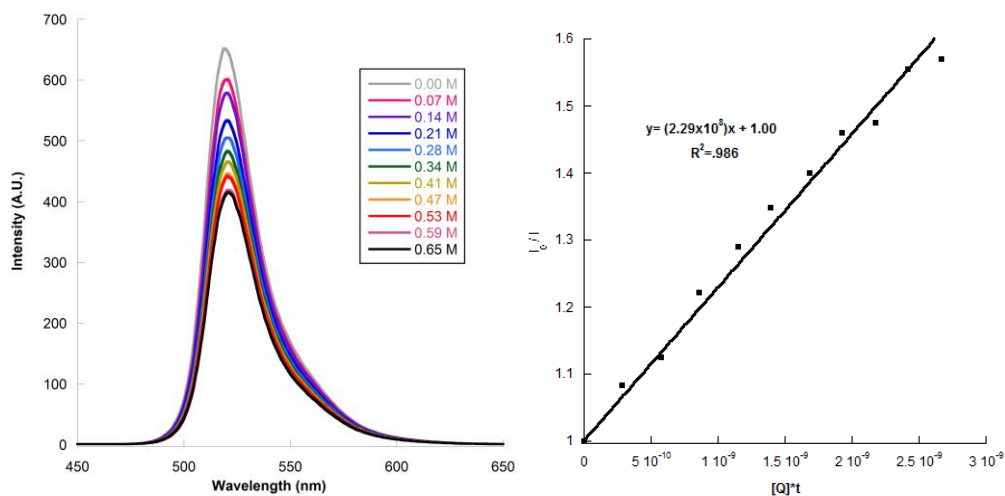


Figure 4.12. Emission spectra of Fl* quenching by TEA in 1:1 EtOH:H₂O pH 12.5 (left) and corresponding Stern-Volmer plot (right).

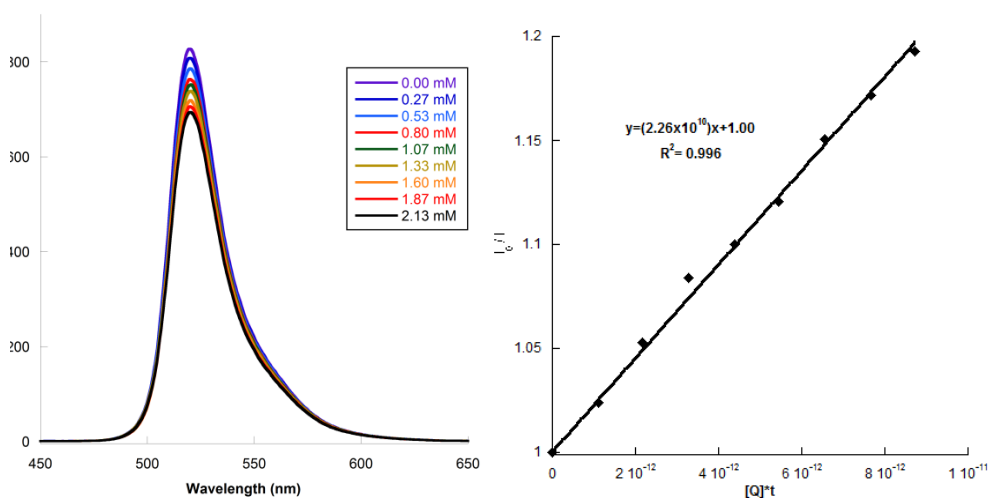


Figure 4.13. Emission spectra of Fl* quenching by **2** in 1:1 EtOH:H₂O pH 12.5 (left) and corresponding Stern-Volmer plot (right).

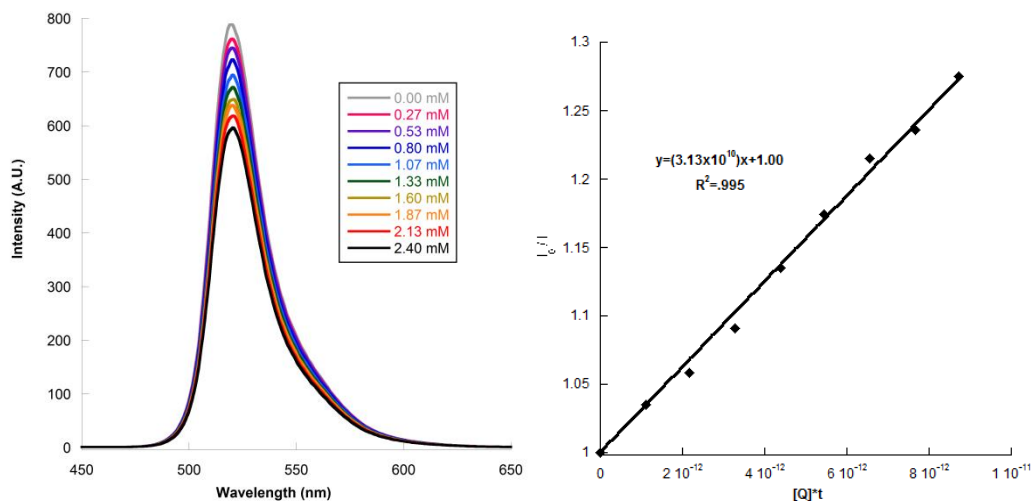


Figure 4.14. Emission spectra of FI* quenching by **4** in 1:1 EtOH:H₂O pH 12.5 (left) and corresponding Stern-Volmer plot (right).

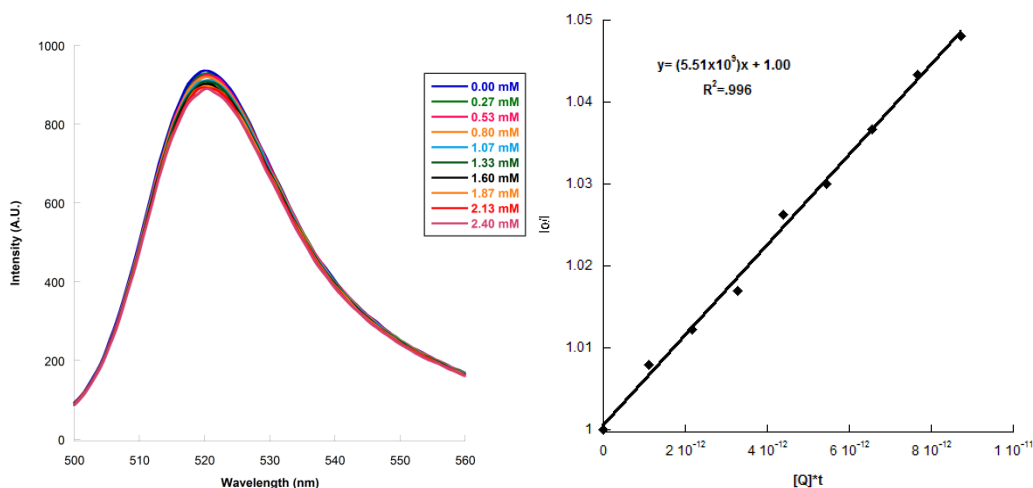


Figure 4.15. Emission spectra of FI* quenching by **6** in 1:1 EtOH:H₂O pH 12.5 (left) and corresponding Stern-Volmer plot (right).

Quenching studies with each of the catalysts were conducted in the same manner. Complex **2** displayed a quenching constant of $2.26 \times 10^{10} \text{ M}^{-1}\text{s}^{-1}$ (Figure 4.13). As hydrogen generation experiments were typically carried out at a catalyst concentration of $2 \mu\text{M}$, the quenching rate for **2** was calculated to be $4.41 \times 10^4 \text{ s}^{-1}$. Similarly, complex **4** shows a quenching constant of $3.20 \times 10^{10} \text{ M}^{-1}\text{s}^{-1}$ and corresponding quenching rate of $6.40 \times 10^4 \text{ s}^{-1}$ under

experimental conditions (Figure 4.14). The sulfinato complex **6** has a quenching constant of $5.51 \times 10^9 \text{ M}^{-1}\text{s}^{-1}$ and quenching rate of $1.20 \times 10^4 \text{ s}^{-1}$ (Figure 4.15). Because the quenching rates of all of the complexes are several magnitudes slower than the quenching rate of TEA, the systems operate under a predominantly reductive quenching pathway.

Also of note is the much slower quenching rate of **6** compared with **2** and **4**, which provides insight into the trend of photocatalytic activity shown in hydrogen evolution studies (Table 4.3). The much slower quenching rate by **6** suggests that the sulfinato catalyst is essentially less effective at accepting an electron from, or quenching, Fl^* as readily as the other catalysts of this family. This provides additional justification for the lower activity of the **6** compared with **2** and **4** as it is not as readily reduced and thus generates hydrogen at a slower rate. Additionally, the slower quenching rate further facilitates a reductive quenching pathway and may result in faster decomposition of the unstable Fl^\cdot .

Table 4.3. Comparison of quenching constants and rates of TEA and catalysts **2**, **4**, and **6**.

Quencher	Quenching Constant ($\text{M}^{-1}\text{s}^{-1}$)	Quenching Rate (s^{-1})
TEA	2.29×10^8	8.24×10^7
2	2.26×10^{10}	4.41×10^4
4	3.13×10^{10}	6.40×10^4
6	5.59×10^9	1.20×10^4

It is also important to note that while the quenching rates of the catalysts are much lower than that of TEA, the quenching constants are on the order of 100 times greater for **2**, **4**, and **6** than the sacrificial donor. This indicates that the experimental parameters of the systems may be adjusted to favor the oxidative pathway, by increasing the [catalyst] relative to [TEA].

Assessing Quantum Yield

Quantum yield studies were conducted to better understand the efficiency of the systems. Performing studies at each of the catalyst's optimal conditions, average quantum yields of 3.1%,

3.4%, and 1.9% were determined for complexes **2**, **4**, and **6**, respectively. These results indicate that 2 to 3 out of every 100 photons absorbed by the samples are converted to hydrogen.¹² While the quantum yields of these systems are modest, these results are similar to yields reported in the literature for analogous systems that generally range from 3-5% for iron, nickel and cobalt catalysts with the same chromophore and sacrificial donor pairings.^{2, 6, 12}

Conclusions

In conclusion, we have developed one of the first and most active examples of photocatalytic systems with mononuclear iron catalysts for proton reduction. Experiments were conducted using three component photochemical systems composed of a photosensitizer, proton reduction catalyst, and sacrificial donor. The parent complex (**2**) is the most active of the three under optimized conditions, yielding over 2100 TON during a 24 hour period. The nitro-functionalized catalyst (**4**) showed lower activity than **2** (>1000 TON), and the sulfinato catalyst (**6**) performed the weakest in these studies. Fluorescence quenching experiments provided insight into the mechanism of the photosystems and indicated that our systems operate under a reductive quenching pathway that may be experimentally modified to achieve an oxidative pathway for improved stability. These studies also justified the lower activity of **6** compared to **2** and **4** due to its much slower quenching rate.

References

- 1) (a) Woolerton, T.W.; Sheard, S.; Chaudhary, Y.S.; Armstrong, F.A. *Energy Environ. Sci.* **2012**, *5*, 7470. (b) Barber, J. *Chem. Soc. Rev.* **2009**, *38*, 185-196.
- 2) (a) Esswein, A.J.; Nocera, D.G. *Chem. Rev.* **2007**, *107*, 4022-4047. (b) Eckenhoff, W.T.; Eisenberg, R. *Dalton Trans.* **2012**, *41*, 13004-13021. (c) Eckenhoff, W.T.; McNamara, W.R.; Du, P.; Eisenberg, R. *Biochimica et Biophysica Acta* **2013**, *1827*, 958-973. (d) Prier, C.K.; Rankic, D.A.; MacMillan, D.W.C. *Chem. Rev.* **2013**, *113*, 5322-5363. (e) Dempsey, J.L.; Brunschwig, W.S.; Winkler, J.R.; Gray, H.B. *Acc. Chem. Res.* **2009**, *42* (12), 1995-2004. (f) Streich, D.; Astuti, Y.; Orlandi, M.; Schwartz, L.; Lomoth, R.; Hammarstrom, L.; Ott, S. *Chem. Eur. J.* **2010**, *16*, 60-63. (g) Han, Z.; McNamara, W.R.; Eum, M.; Holland, P.L.; Eisenberg, R. *Angew. Chem. Int. Ed.* **2012**, *51*, 1667-1670.
- 3) (a) Wise, C.F.; Liu, D.; Mayer, K.J.; Crossland, P.M.; Hartley, C.L.; McNamara, W.R. *Dalton Trans.* **2015**, *44*, 14265-14271. (b) Roy, S.; Bacchi, M.; Berggren, G.; Artero, V. *ChemSusChem* **2015**, *8*(21), 3632-3638. (c) Na, Y.; Wang, M.; Pan, J.; Zhang, P.; Akermark, B.; Sun, L. *Inorg. Chem.* **2008**, *47*, 2805-2810.
- 4) Han, Z.; Qiu, F.; Eisenberg, R.; Holland, P.L.; Krauss, T.D. *Science* **2012**, *338*, 1321-1324.
- 5) (a) Probst, B.; Guttentag, M.; Rodenberg, A.; Hamm, P.; Alberto, R. *Inorg. Chem.* **2011**, *50*, 3404-3412. (b) Na, Y.; Wang, M.; Pan, J.; Zhang, P.; Akermark, B.; Sun, L. *Inorg. Chem.* **2008**, *47*, 2805-2810.
- 6) Lazarides, T.; McCormick, T.; Du, P.; Luo, G.; Lindley, B.; Eisenberg, R. *J. Am. Chem. Soc.* **2009**, *131*, 9192-9194.
- 7) (a) McNamara, W.R.; Han, Z.; Alperin, P.J.; Brennessel, W.W.; Holland, P.L.; Eisenberg, R. *J. Am. Chem. Soc.* **2011**, *133*, 15368-15371.
- 8) Imbert, C.; Hratchian, H.P.; Lanznaster, M.; Heeg, M.J.; Hryhorczuk, L.M.; McGarvey, B.R.; Schlegel, H.B.; Verani, C.N. *Inorg. Chem.* **2005**, *44*, 7414-7422.
- 9) Lanznaster, M.; Neves, A.; Bortoluzzi, A.J.; Assumpcao, A.M.C.; Vencato, I.; Machado, S.P.; Drechsel, S.M. *Inorg. Chem.* **2006**, *45*, 1005-1011.
- 10) Miessler, G. L., & Tarr, D. A. (2011). *Inorganic chemistry*. Upper Saddle River, NJ: Pearson Prentice Hall.
- 11) Heinrich, L.; Li, Y.; Vaissermann, J.; Chottard, G.; Chottard, J. *Angew. Chem. Int. Ed.* **1999**, *38*(23), 3526-3528.
- 12) Wang, W.; Chen, J.; Li, C.; Tian, W. *Nat. Commun.* **2014**, *5*, 4647.

Appendix C

Table C1. Comparison of Chromophores and Sacrificial Donors

Catalyst	TON after 12 hours of Irradiation with Chromophore/Sacrificial Donor			
	FI/TEA	EY/TEOA	EY/TEA	Ru(bpy) ₃ ²⁺ /AA
2	1132	2	385	0
4	545	0	164	0
6	421	0	319	0

Optimization Studies for **4**

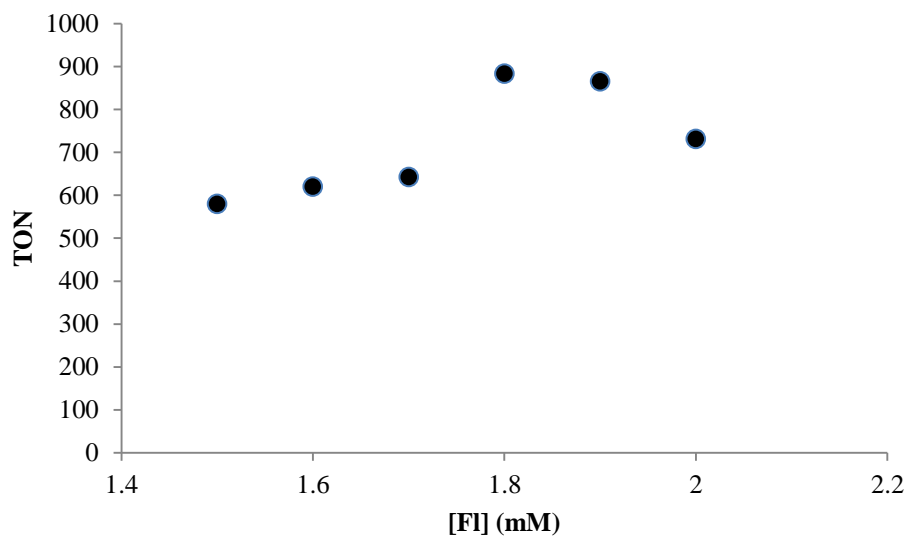


Figure C1. TON vs. [FI] with 2 μ M of **4** and 5% TEA in 1:1 H₂O:EtOH solution after 12 hours of irradiation.

**Note:* TONs in this study appear artificially high because this optimization study was performed using higher intensity LEDs than for regular studies.

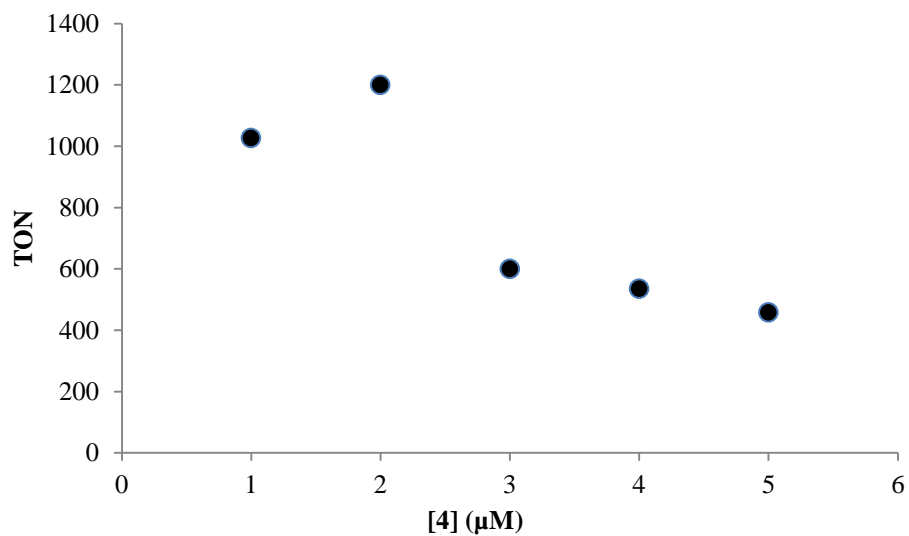


Figure C2. TON vs. [4] with 1.8 mM of Fl and 5% TEA in 1:1 H₂O:EtOH solution after 12 hours of irradiation.

**Note:* TONs in this study appear artificially high because this optimization study was performed using higher intensity LEDs than for regular studies.

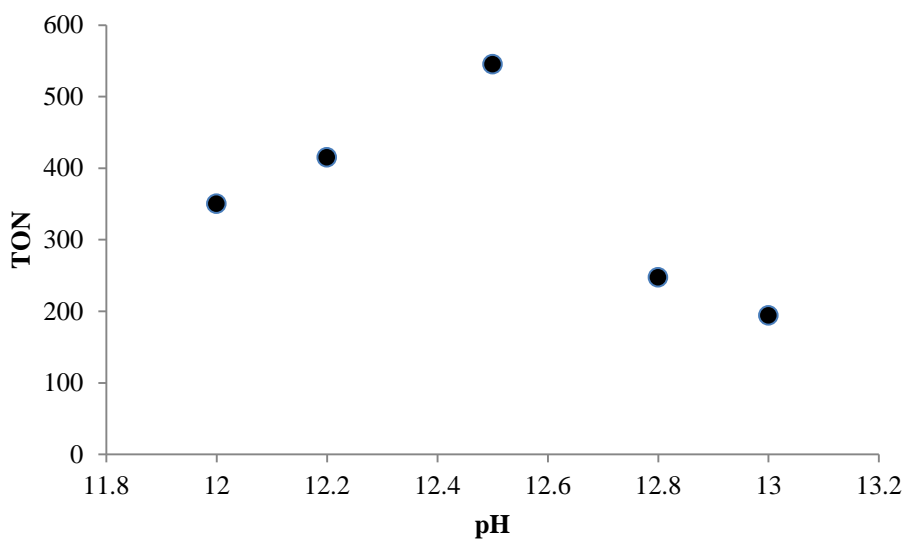


Figure C3. TON vs. pH with 2 μM of 4, 1.9 mM Fl and 5% TEA in 1:1 H₂O:EtOH solution after 12 hours of irradiation.

Optimization Studies for 6

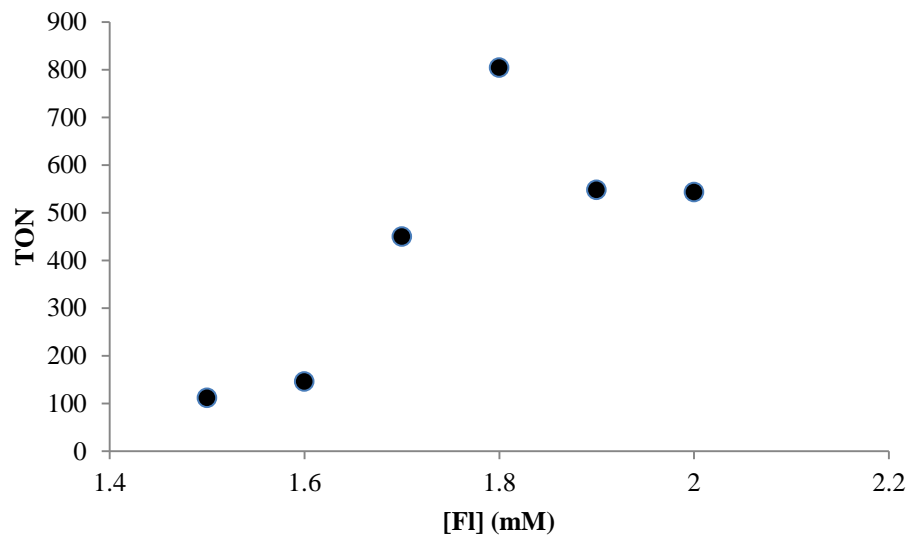


Figure C4. TON vs. [FI] with 2 μM of **6** and 5% TEA in 1:1 H_2O :EtOH solution after 12 hours of irradiation.

**Note:* TONs in this study appear artificially high because this optimization study was performed using higher intensity LEDs than for regular studies.

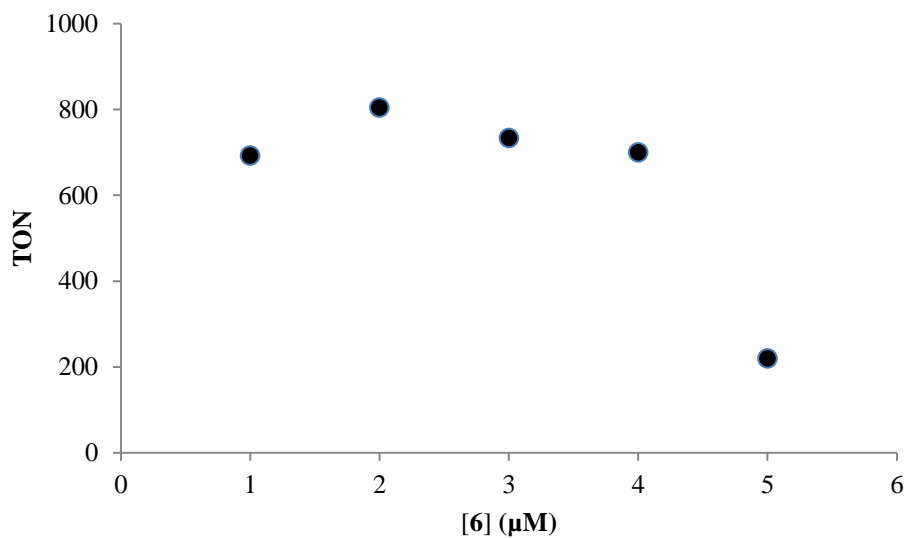


Figure C5. TON vs. [6] with 1.8 mM of Fl and 5% TEA in 1:1 H₂O:EtOH solution after 12 hours of irradiation.

**Note:* TONs in this study appear artificially high because this optimization study was performed using higher intensity LEDs than for regular studies.

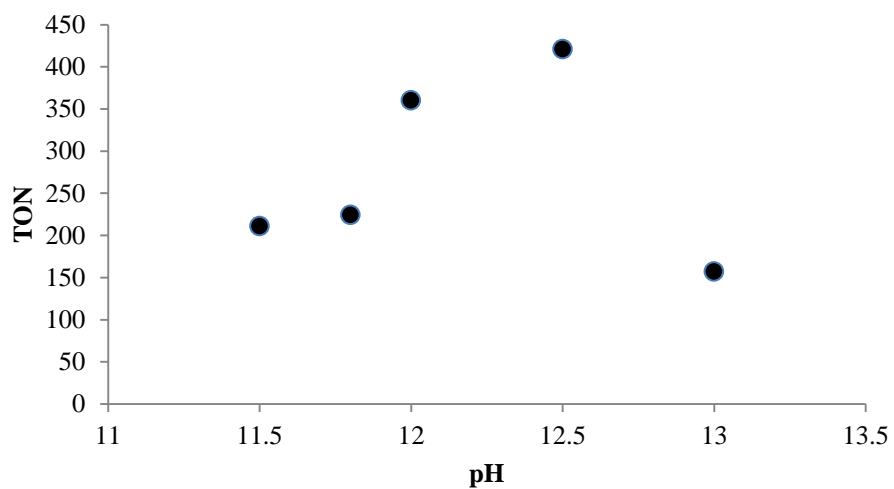


Figure C6. TON vs. pH with 2 μM of 6, 1.8 mM Fl and 5% TEA in 1:1 H₂O:EtOH after 12 hours of irradiation.

Calculation of quantum yield:

A sample calculation for determining the quantum yield for **4** is shown below:

$$H_2 \text{ produced: } 6.32 \times 10^{-6} \text{ mol}$$

$$k = \frac{(6.32 \times 10^{-6} \text{ mol})}{86400 \text{ s}} = 7.31 \times 10^{-11} \frac{\text{mol}}{\text{s}}$$

$$P = (1.86 \times 10^{-3} \text{ W}) - (910 \times 10^{-6} \text{ W}) = 9.50 \times 10^{-4} \text{ W}$$

$$q_P = \frac{(P \times \lambda)}{(c \times h)} = \frac{(9.50 \times 10^{-4} \text{ W})(520 \times 10^{-9} \text{ m})}{(3.00 \times 10^8 \text{ m/s})(6.626 \times 10^{-34} \text{ J/s})} = 2.49 \times 10^{15} \text{ s}^{-1}$$

$$\frac{q_P}{\text{mol}} = \frac{(2.49 \times 10^{15} \text{ s}^{-1})}{(6.02 \times 10^{23} \text{ photons/mol})} = 4.14 \times 10^{-9} \frac{\text{mol}}{\text{s}}$$

$$\phi_{H_2} = \frac{2k}{q_P} = \frac{2(7.31 \times 10^{-11} \text{ mol/s})}{(4.14 \times 10^{-9} \text{ mol/s})} \times 100 = 3.5\%$$